ČESKÉ VYSOKÉ UČENÍ TECHNICKÉ
v PRAZE

Fakulta jaderná a fyzikálně inženýrská

Disertační práce

Měření ρ^0 fotoprodukce při vysokých energiích s detektorem ALICE

Praha 2022 **Ing. David Horák**

CZECH TECHNICAL UNIVERSITY
IN PRAGUE

Faculty of Nuclear Sciences and Physical
Engineering

Dissertation

Measurement of ρ^0 photoproduction at high energies with the ALICE detector

Prague 2022 **Ing. David Horák**

Bibliografický záznam

Autor	Ing. David Horák
	České vysoké učení technické v Praze
	Fakulta jaderná a fyzikálně inženýrská
	Katedra fyziky
Název práce	Měření fotoprodukce ρ^0 při vysokých energiích
	s detektorem ALICE
Studijní program	Aplikace přírodních věd
Studijní obor	Jaderné inženýrství
Školitel	prof. Jesús Guillermo Contreras Nuño, Ph.D.
	České vysoké učení technické v Praze
	Fakulta jaderná a fyzikálně inženýrská
	Katedra fyziky
Školitel-specialista	Mgr. Michal Broz, PhD.
	České vysoké učení technické v Praze
	Fakulta jaderná a fyzikálně inženýrská
	Katedra fyziky
Akademický rok	2021/2022
Počet stran	176
Klíčová slova	ALICE, koherentní, ρ^0, vektorový mezon, fotoprodukce, ultra-periferní srážky

Bibliographic Entry

Author	Ing. David Horák Czech Technical University in Prague Faculty of Nuclear Sciences and Physical Engineering Department of Physics
Title of Dissertation	Measurement of ρ^0 photoproduction at high energies with the ALICE detector
Degree Programme	Application of Natural Sciences
Field of Study	Nuclear Engineering
Supervisor	prof. Jesús Guillermo Contreras Nuño, Ph.D. Czech Technical University in Prague Faculty of Nuclear Sciences and Physical Engineering Department of Physics
Supervisor-specialist	Mgr. Michal Broz, PhD. Czech Technical University in Prague Faculty of Nuclear Sciences and Physical Engineering Department of Physics
Academic Year	2021/2022
Number of Pages	176
Key Words	ALICE, coherent, ρ^0, vector meson, photoproduction, ultra-peripheral collisions

Acknowledgement

I would like to thank to my supervisor Jesús Guillermo Contreras Nuño for his kind support, guidance and time he devoted to me during my whole PhD. I would like to also thank to my supervisor-specialist Michal Broz for his technical support when things didn't work out.

Big thanks also belong to all people in the ALICE UPC group for their valuable comments and support of this research.

I am also grateful to my Alma Mater, Czech Technical University in Prague, Faculty of Nuclear Sciences and Physical Engineering, for the material support and all the education they have provided me.

Last but not least, I would like to thank all people around me, my family and my friends. Without them, dreams would never come true.

Declaration

I hereby declare that this thesis is the result of my own work and all the sources I used are in the list of references.

I have no objection to usage of this work in compliance with the act §60 Law No. 121/2000 Coll. (Copyright Act), and with the rights connected with the copyright act including the changes in the act.

In Prague, 2022 Ing. David Horák

Abstrakt

Tato práce shrnuje výsledky výzkumu v oblasti koherentní fotoprodukce ρ^0 mesonu v ultraperiferních srážkách na detektoru ALICE. Účinný průřez koherentní produkce ρ^0 byl změřen ve srážkách Pb–Pb při těžišťové energii 5.02 TeV a ve srážkách Xe–Xe při těžišťové energii 5.44 TeV. Data byla naměřena na detektoru ALICE na urychlovači LHC v letech 2015, resp. 2017. Mojí prací byla kompletní analýza těchto dat včetně korekcí na detektorové efekty. Naměřené účinné průřezy jsou porovnány s teoretickými předpověďmi založenými na různých modelech. Ukázalo se, že současné modely zahrnující efekty mírného stínění a saturace k popisu dynamických QCD efektů poměrně dobře popisují naměřená data.

Abstract

This thesis will summarise of results on coherent ρ^0 photoproduction in ultraperipheral collisions with the ALICE detector. The cross section of coherent ρ^0 photoproduction was measured in Pb–Pb collisions at a centre-of-mass energy 5.02 TeV and in Xe–Xe collisions at a centre-of-mass energy 5.44 TeV. The data were recorded by the ALICE experiment at the LHC in 2015, 2017 respectively. My work was a complete analysis of these data including corrections on detector effects. The measured cross sections are compared with theoretical predictions based on various models. The results show that current models implementing moderate shadowing or saturation effects to account for dynamic QCD effects describe the data satisfactorily.

Contents

Preface

The world's largest and highest-energy particle accelerator nowadays, the Large Hadron Collider (LHC), has shown a remarkable performance and physical results over the last decade. However, it is not only the most powerful collider of protons and heavy ions, but also the most powerful source of photons. The photon-photon, photon-proton and photon-ion processes can be studied in ultra-peripheral collisions (UPCs). The ALICE experiment is the most suitable detector at the LHC to study soft processes in UPCs, including the coherent ρ^0 photoproduction.

The photoproduction of vector mesons is a clean probe of the hadronic structure and provides a direct determination of the gluon distribution of the target. The coherent ρ^0 photoproduction is an excellent process to test the black disc regime of quantum chromodynamics (QCD). This process was extensively studied at midrapidity in Au—Au UPCs at the Relativistic Heavy Ion Collider (RHIC), but at a substantially lower energy than what can be reached at the LHC.

The purpose of this work is to give a complete overview of the analysis procedure I performed during my PhD studies at ALICE, which resulted in two published papers on coherent ρ^0 photoproduction. It can also be read by future students focusing on UPCs to gain an overview in this topic.

Chapter 1 provides the reader an overview of the experimental facility at CERN that produced the analysed data. The Large Hadron Collider is introduced together with its design, main operational characteristics and physics programme in the near future. Then, the ALICE detector is described. The main focus is on the design and operation of the most important detectors for the UPC analyses together with their planned upgrade. The end of the chapter describes the data processing handled by the data acquisition (DAQ) system and reconstruction software on the computing grid.

Chapter 2 is devoted to an introduction to the physics of UPCs. The production mechanisms of vector mesons in proton-ion and ion-ion collisions are described, followed by production mechanisms of background particles in such collisions. The following section summarises theoretical and phe-

nomenological models and calculations that are nowadays commonly used in UPC physics.

Chapter 3 presents the ρ^0 vector meson, its properties and models describing its invariant mass spectrum. Then, kinematic variables are defined and general measurement procedures are explained. At the end of the chapter, previous measurement on coherent ρ^0 photoproduction at HERA, RHIC, and at the LHC are summarised.

The main experimental results are shown in Chapter 4. The published analyses on coherent ρ^0 photoproduction in Pb–Pb and Xe–Xe ultra-peripheral collisions performed at ALICE are described in detail. Data and Monte Carlo selections are described based on observed data quality in specific variables, followed by the estimation of correction factors and the signal extraction procedure that lead to the differential cross section for both measurements. Several other results obtained during the procedure are discussed. The end of the chapter is devoted to a discussion and a proposal for future ρ^0 measurements at ALICE that can be performed using not only current data but also, in the near future, data to be recorded during Run 3 and 4 at the LHC.

Chapter 1

Experimental facility

The experimental facility, the Large Hadron Collider (LHC), used in this work is situated on the French-Swiss border near Geneva and its operator is the European Organization for Nuclear Research (CERN) that was established in 1954. The main interest of CERN lies in basic research. The successful research in past decades resulted in several Nobel Prize awards. To became a frontier in physics, CERN is heavily involved in technology development, worldwide cooperation among scientists, and education.

1.1 LHC at CERN

The Large Hadron Collider [1] is nowadays the largest and most powerful accelerator in the world. Its main goal as a "discovery" machine was to scan a higher invariant mass region than previous accelerators in order to search for the Higgs boson which was found in 2012 [2, 3] and for signs of new physics beyond the Standard model.

1.1.1 Accelerator design

The LHC is built in the 27 km long tunnel of its predecessor LEP [4]. The circle is divided into eight segments called octants (Fig. 1.1), in each of them an interaction point (IP) can be placed. Only four of them are used for large experiments: ATLAS (IP1), ALICE (IP2), CMS (IP5) and LHCb (IP8). The accelerating devices, radio frequency cavities (RF), are placed in Octant 4, the beam dump is in Octant 6.

The key element of the LHC is a 15 m long superconductive dipole magnet (Fig. 1.2). The collider consist of 1232 of these magnets that keep particle beams on a stable circular trajectory using a magnetic field of 8 T. There

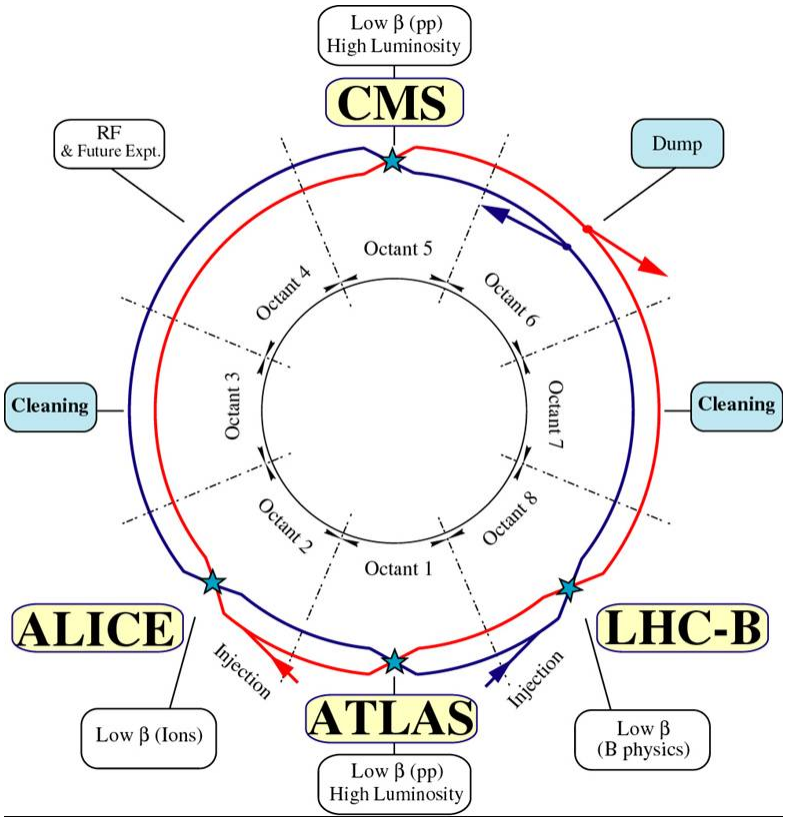

Fig. 1.1: Layout of the LHC and positions of main experiments. Taken from [5].

are also straight sections that contain quadrupole and higher-pole magnets providing focusation and correction of the beam orbit.

There are two beam pipes inside the dipole magnet enclosed by the superconductive coil that uses an electrical current of 12 000 A. The steel structure acts as a coil core, provides the integrity of the magnet and a cover to the cryogenic systems and to the electronics.

The LHC is designed to operate with two colliding beams. Beam 1 rotates clockwise and Beam 2 rotates anticlockwise when looking from above. They intersect each other and collide in four experiments, where they can be aligned and focused according to needs of the experiment.

1.1.2 Filling procedure

Both beams are injected into the LHC at 450 GeV after acceleration in the cascade of several older accelerators shown in Fig. 1.3. They are filled in so-called bunches with 25 ns spacing. Each bunch is placed in a bucket: a

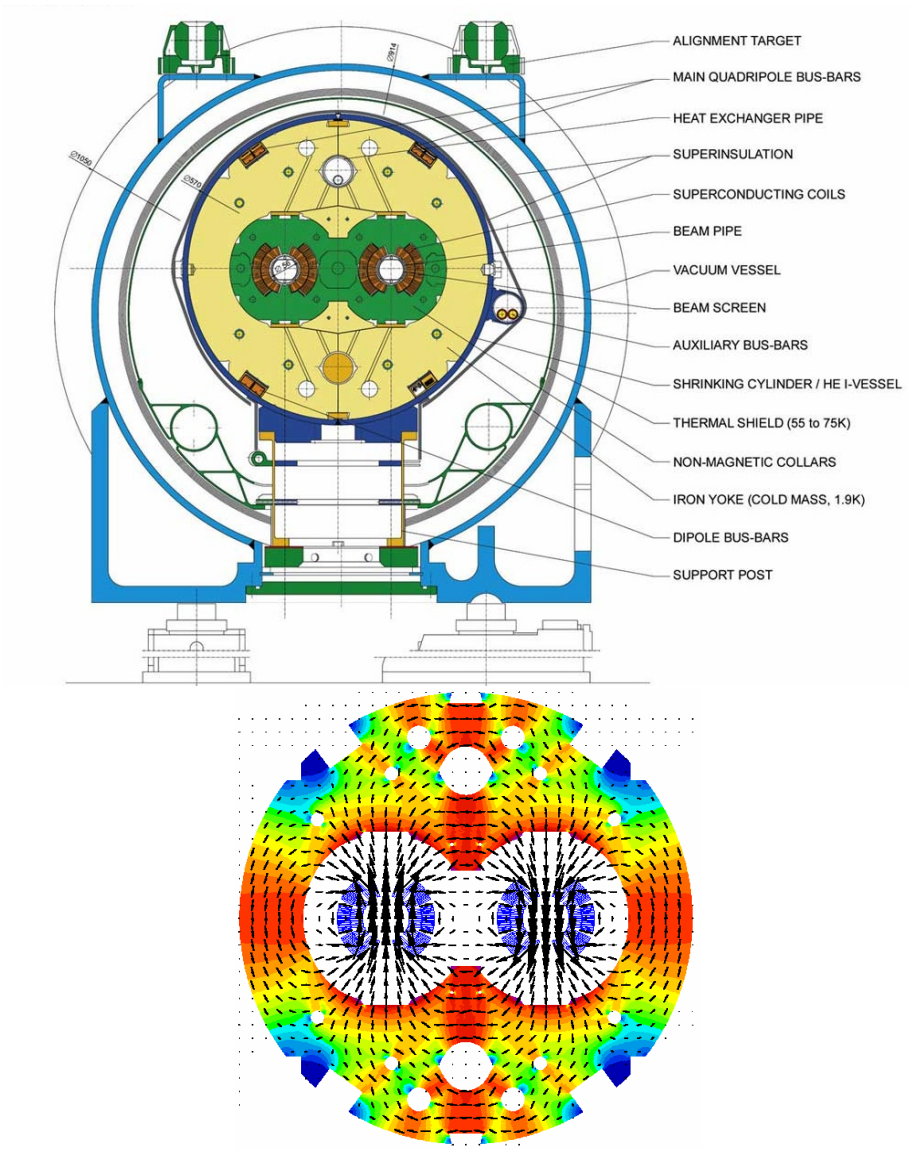

Fig. 1.2: Top: Cross section of the LHC dipole magnet. Bottom: Magnetic field inside the dipole magnet. Taken from [5].

virtual position along the LHC circumference that is given by the RF synchronisation. The LHC is designed to operate with up to 2808 bunches. During filling phase, first a "pilot" bunch is injected to test the LHC operation. Then bunches are filled according to a planned filling scheme. The injection phase is the most dangerous one from the point of view of the LHC and all experiments and its detectors are usually shut down. The position of experiments allows LHC operators to use a different number of collid-

ing bunches in each experiment, however ATLAS and CMS have to operate with the same number of colliding bunches. There is also an abort gap in the bunch spacing that is designed to turn on a kicker—a very fast magnet designed to dump the beam.

When the accelerator is filled, a ramp up phase follows. A gradually increasing current in the dipole magnets together with delivering RF power accelerates beams from 450 GeV up to the desired energy. This energy was gradually increased in past years and reached up to 6.5 TeV per beam in pp collisions in Run 2 (2015–2018). Ramp up is followed by squeezing of the beam to reach maximum density of the beam and by the adjust phase when beams are brought into collisions. The duration of these phases is around 1 hour and this timescale is used by collaborations to bring detectors to operation from safe mode and for their calibration.

After that, stable beams are declared and the data taking period can start. In this phase, the luminosity of the beam is slowly decreasing as collisions

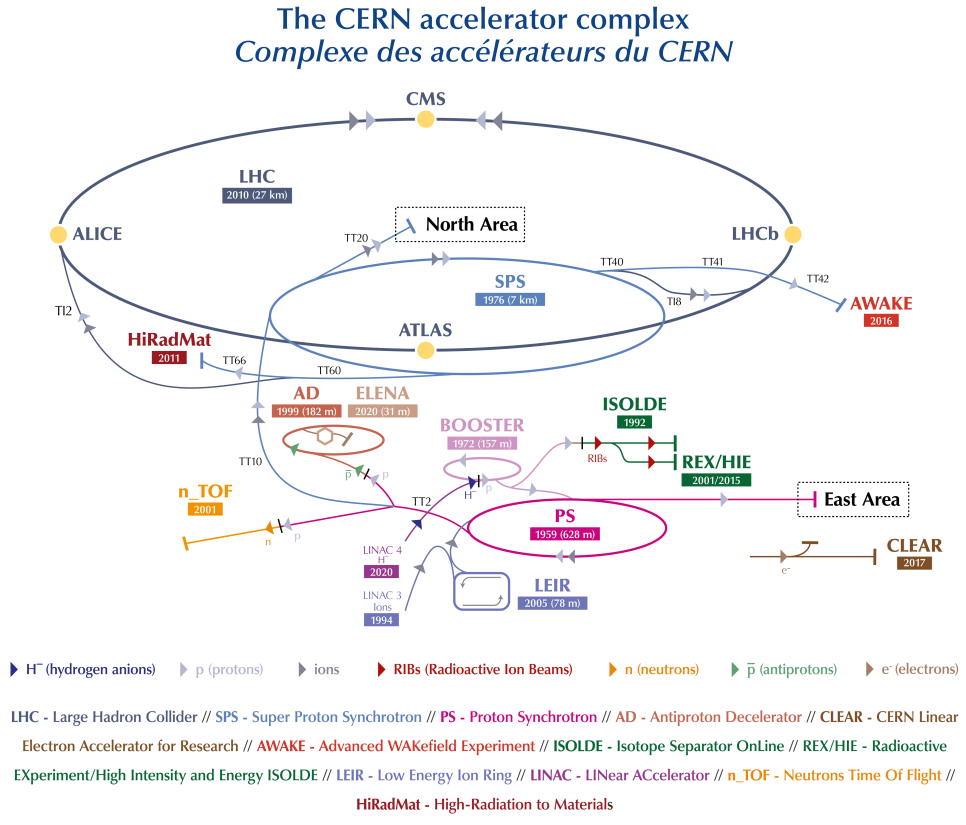

Fig. 1.3: CERN accelerator complex (2019). Taken from [6].

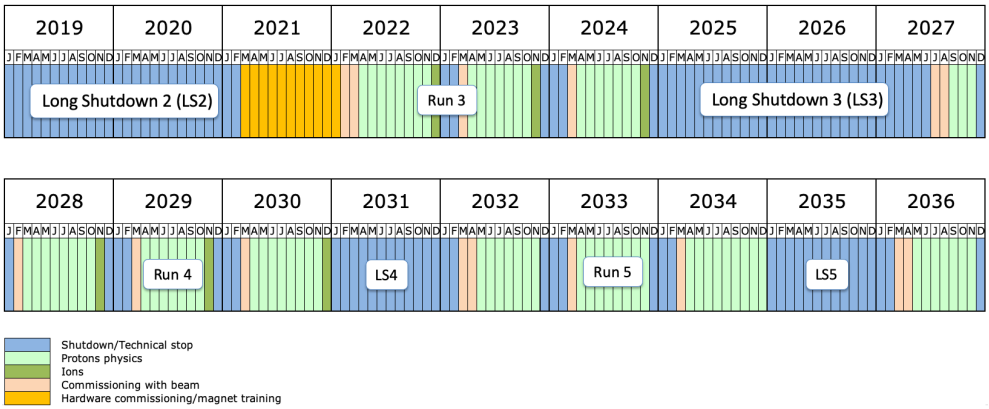

Fig. 1.4: The latest LHC schedule is planned up to 2036. Taken from [7].

occur and some of the beam particles are lost by beam–gas interactions. This phase usually ends after several hours, when the collision rate loss is higher than the time needed for refilling the LHC. In that case a beam dump is performed, followed by a slow ramp down of dipole magnets.

1.1.3 Physics programme

The LHC started its operation on September 10, 2008, running the first beam. Few days later, September 19, 2008, during a powering test of a main dipole magnet, a fault occurred in the electrical connection between the dipole and a quadrupole magnet causing a helium leak resulting in an explosion and damaging of several main dipole magnets [8]. This accident delayed the LHC operation for more than one year.

The LHC operation is divided into data taking periods called Runs, which usually last several years. They are separated by Long Shutdowns (LS) dedicated to the maintenance and upgrade of the LHC as well as each experiment. Each year starts with commissioning of the facility. Then, most of the year is dedicated to proton–proton collisions which are the main point of interest for ATLAS, CMS and LHCb. After this period, usually approximately one month is dedicated to ion physics in lead–lead (Pb–Pb) and proton–lead (p–Pb) collisions. In 2018, a short time was also dedicated to special xenon–xenon (Xe–Xe) collisions. The ion programme is scheduled (see Fig. 1.4) up to the year 2030 and will end when upgrade to high–luminosity LHC (HL–LHC) will come.

1.2 The ALICE Detector

ALICE (A Large Ion Collider Experiment) as a general-purpose heavy-ion detector at CERN LHC was firstly proposed in 1990 and approved in 1997. In this chapter we will briefly describe its main sub-detectors and their upgrades during the years, especially those that are crucial from the point view of UPCs.

The detector design is described in detail in [9], its performance in [10] and there are also two Physics Performance Reports [11, 12] describing the physics topics of interest, ALICE subsystems, detector performance, event reconstruction procedures, and event generators. The main objective of ALICE detector is to measure various processes related to the quark-gluon plasma (QGP) in order to get insight into the phase diagram of QGP and the QCD phase transition. Extrapolation from RHIC results showed that the charge particle multiplicity in Pb–Pb midrapidity could reach up to $\mathrm{d}N/\mathrm{d}\eta = 4000$, therefore the tracking capabilities had to be robust with precise three-dimensional tracking, momentum measurement (spanning several orders of magnitude from tens of MeV to hundreds of GeV), and particle identification.

The interaction rate designed for ion beams at the LHC is low (10 kHz for Pb–Pb collisions) and also the radiation doses are moderate ($< 3000\,\mathrm{Gy}$), allowing for slow and high-granularity tracking detectors. The expected Pb–Pb luminosity per year was $0.5\,\mathrm{nb}^{-1}$.

1.2.1 Overall layout

We will describe the detector layout and technical specifications as it was designed for Run 1. Detector upgrades that were done for Run 2 and also upgrades for Run 3 are mentioned in a separate paragraph at the end of each detector section.

The ALICE detector is located in a cavern 56 m underground at the Interaction Point 2. The detector layout can be seen in Fig. 1.5. It can be divided into a central barrel, that is embedded in a large solenoid magnet (originally used in the cavern by the L3 experiment at LEP) providing a moderate magnetic field up to 0.5 T in the midrapidity region, and a muon spectrometer at forward rapidity on the side towards the CMS experiment (so-called C-side). The opposite side (A-side) of the detector is occupied by a massive concrete block that protects the detector against any beam failure during the injection phase as the injection point for Beam 1 is placed near ALICE.

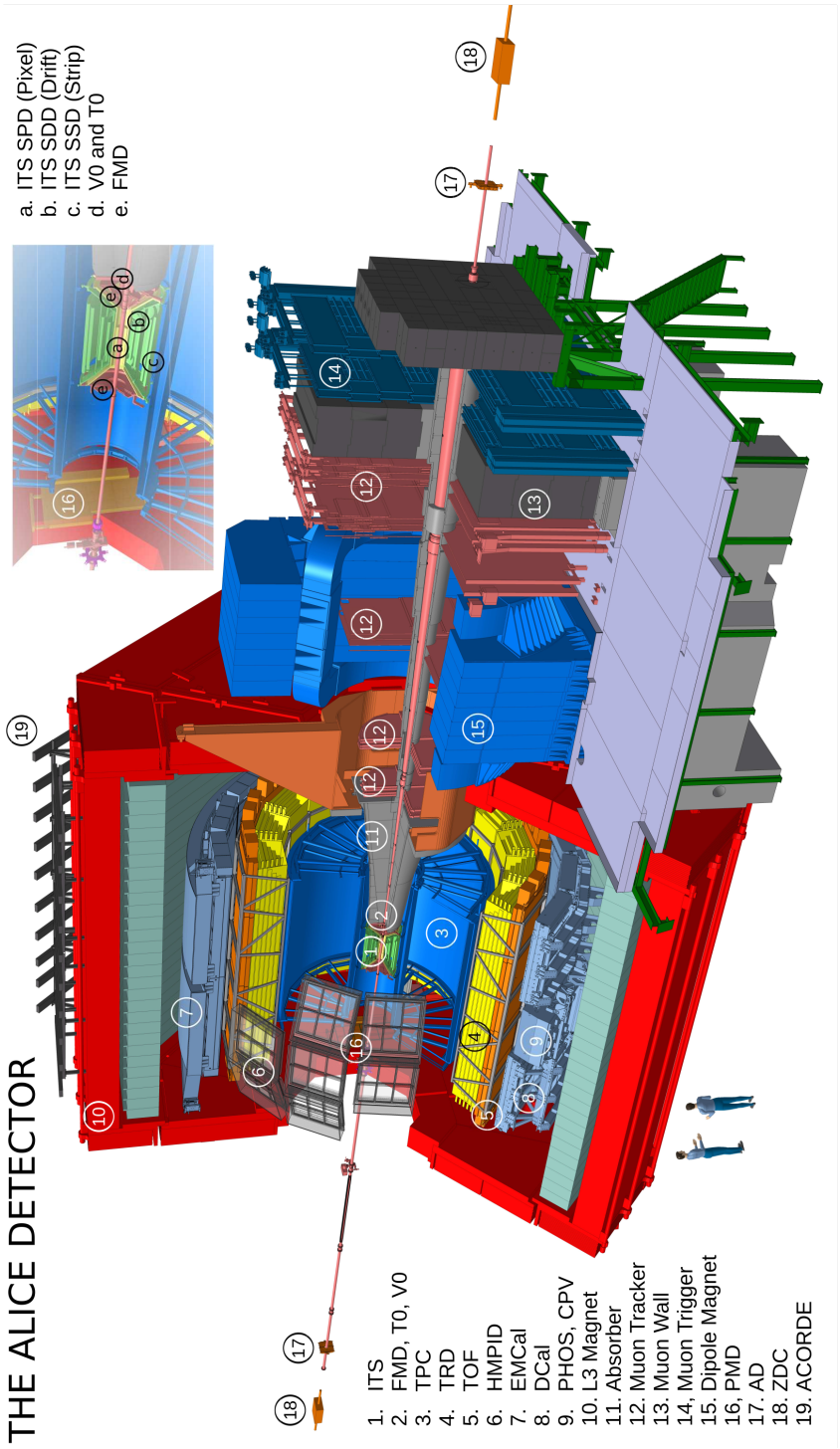

Fig. 1.5: ALICE layout as designed for Run 2. Taken from [13].

1.2.2 Inner Tracking System

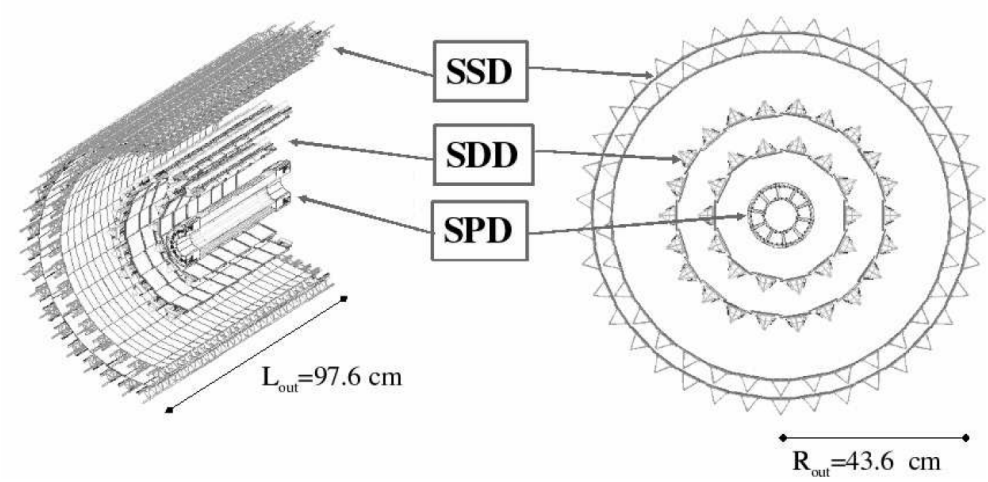

Fig. 1.6: Layout of the ITS. Taken from [9].

The Inner Tracking System (ITS) is the barrel detector closest to the beam pipe. The main tasks of the ITS are to localise the primary vertex (the resolution is better than 100 μm), to reconstruct secondary vertices from hyperon decays and B and D mesons, to track and identify particles with momentum less than 200 MeV/c, and to improve momentum and angle resolution of particles reconstructed in the Time-Projection Chamber.

The ITS consists of six coaxial layers of silicon detectors as it is shown in Fig. 1.6. The layers radii vary from 4 to 43 cm and the detector covers the pseudorapidity interval $|\eta| < 0.9$. The two innermost layers forming the Silicon Pixel Detector (SPD) have an enlarged pseudorapidity coverage up to $|\eta| < 1.4$. The two middle layers consist of Silicon Drift Detectors (SDD) followed by two outer layers of Silicon Strip Detector (SSD). The momentum and impact-parameter resolution of low-momentum particles is dominated by the multiple scattering effect in the material of the detector, therefore the material budget needs to be minimal. In this design used in Run 1 and 2, an effective detector thickness of 7.18 % of X_0 was achieved.

SPD

We will describe the Silicon Pixel Detector in more detail as it plays an important role in this work. It has two important roles: to find primary and secondary vertices and to provide a trigger input. The former is done using

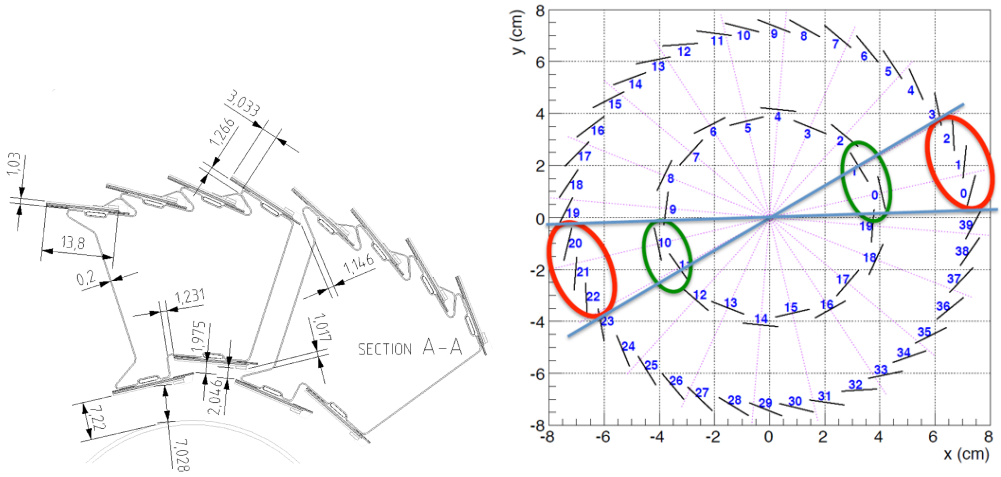

Fig. 1.7: (Left) Carbon-fibre support of SPD staves. Taken from [9]. (Right) SPD stave numbering.

tracklets—track fragments that are created from two reconstructed hits in the SPD, one in the inner and the second in the outer layer.

The SPD is based on hybrid silicon pixels (a sensor is bumb-bonded to the read-out chip) organised into a two-dimensional matrix. The read-out of each pixel is binary: a threshold voltage is compared to the amplified and shaped signal and if the latter is above threshold, a logical one is in the output. The detector sensor is made as a 256×160 array of pixel cells, where the dimensions of each pixel are $50(r\phi) \times 425(z)\,\mu$m. The basic detector module is a half-stave consisting of two ladders, one Multi-Chip Module (MCM), and multi-layer interconnect. In total, the SPD consists of 60 staves (Fig. 1.7), 240 ladders, and 1200 chips.

Each detector chip provides a Fast-OR signal when one or more of the pixels are hit. These signals are sent every 100 ns (10 MHz) through optical links and after pre-processing, it can contribute to the Level 0 (L0) trigger decision in the ALICE Central Trigger Processor (CTP). The pre-processing is done on FPGA motherboards, where various algorithms, based on global multiplicity or on predefined topologies, can be implemented as boolean logic functions. This type of information is particularly useful at low multiplicities and therefore it is widely used in case of an ultra-peripheral collision.

SDD

The two intermediate layers of ITS consist of Silicon Drift Detectors (SDD). Apart from providing the position information, they offer an analog read-

out. Therefore, they can provide specific ionisation energy loss, $\mathrm{d}E/\mathrm{d}x$, information that can be used for particle identification.

SSD

The Silicon Strip Detectors (SSD) are the two outermost layers of the ITS. The two-dimensional position information is used for matching reconstructed tracks from the Time-Projection Chamber to the ones from ITS and also it provides a $\mathrm{d}E/\mathrm{d}x$ measurement.

Upgrade

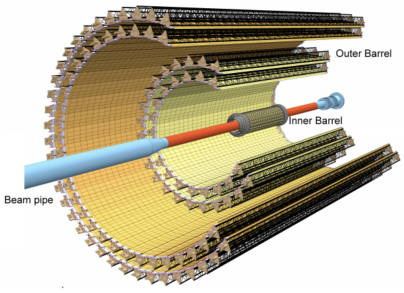

BARREL	LAYERS	RADIUS (cm)	LENGHT (cm)	NUM. STAVES	NUM. CHIPS
Inner	Layer 0	22.4	271	12	108
Inner	Layer 1	30.1	271	16	144
Inner	Layer 2	37.8	271	20	180
Outer	Layer 3	194.4	843	24	2688
Outer	Layer 4	243.9	843	30	3360
Outer	Layer 5	342.3	1475	42	8232
Outer	Layer 6	391.8	1475	48	9408

Fig. 1.8: (Left) Schematic layout of the upgraded ITS for Run 3. (Right) Characteristics of the upgraded ITS. Taken from [14].

The ITS was substituted during the LS2 with a completely new silicon-based detector using a MAPS (Monolithic Active Pixel Sensor) technology that will be used in Run 3 [14]. The main benefit of this technology is a large reduction of the material budget to 1.3 % of X_0 compared to 7.18 % with previous ITS. The new ITS is designed on an ALPIDE chip that has a $30 \times 30\,\mu\mathrm{m}^2$ pixel size. These chips are connected into seven cylindrical layers (the three innermost referred as Inner Barrel, the four outermost referred as Outer Barrel). The distance to the beam pipe is also reduced. These design characteristics will improve tracking efficiency at low momenta and impact-parameter resolution. Together with the enhanced read-out capabilities, the new ITS is necessary to measure a large sample of short lived systems, e.g. heavy-flavour hadrons, quarkonia, and low mass dileptons, that are keys to a precise exploration of QGP properties.

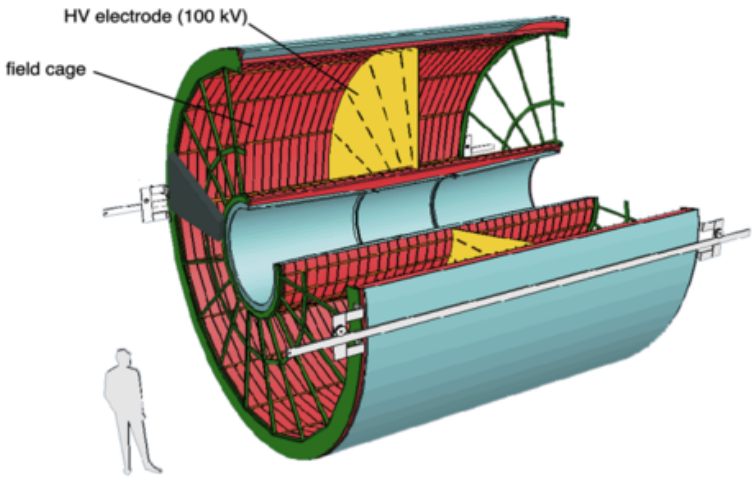

Fig. 1.9: A scheme of a TPC. Taken from [15].

1.2.3 Time-Projection Chamber

The Time-Projection Chamber (TPC) is the main tracking detector of ALICE in the midrapidity region. It was designed to handle very large charge particle densities up to $\mathrm{d}N/\mathrm{d}\eta = 8\,000$ which results up to 20 000 charged primary and secondary tracks in the TPC volume (never achieved before). At Pb–Pb peak luminosity an interaction rate of 8 kHz was tested.

In addition to tracking capabilities, the TPC provides the charged-track momentum measurement, particle identification, and vertex position estimation. The covered p_T range starts at about 0.1 GeV/c and goes up to 100 GeV/c with a precision of 0.7 % at 0.5 GeV/c.

The detector is made in a cylindrical field cage as shown in Fig. 1.9. The active volume has an inner radius of 85 cm, an outer radius of 250 cm, and an overall length of 500 cm along the beam direction (z-axis). It has a full azimuthal coverage, except dead zones affecting high-momentum particles as it is divided into 18 sectors. The pseudorapidity acceptance is $|\eta| < 0.9$ (matching to ITS and TOF) for tracks with full radial length and up to $|\eta| < 1.5$ for tracks with a reduced length.

The inner volume is filled with 90 m^3 of mixture of $Ne/CO_2/N_2$ that is optimised for low drift speed, low radiation length, space-charge effects, ageing, and stability properties. However, Run 2 shows substantial space-charge distortions due to high multiplicities causing difficulties in the TPC calibration.

The volume is divided in half by a central electrode. The high voltage

of 100 kV generates an uniform field along the z-axis. Charged particles travelling through the TPC ionise the gas mixture and generate clusters of electrons that drift to the end plates. There are multi-wire proportional chambers (MWPC) with cathode pad read-out mounted on the end plates giving a 2-dimensional track information. These read-out chambers are closed by a gating grid until a Level 1 (L1) trigger signal is obtained. The third space-position is obtained using the drift-time information with a maximum of 90 μs (which is also the TPC dead-time).

The TPC provides particle identification (PID) using specific energy loss $\mathrm{d}E/\mathrm{d}x$ measurements. The ionisation produced by each track is sampled by so-called cluster points and it is computed as a truncated mean. That results in an excellent resolution of $\sim 5\,\%$. As shown in Fig. 1.10, kaons and protons can be identified up to momentum $p \approx 1 - 2\,\mathrm{GeV}/c$. Electrons can be distinguished from pions over a wide momentum range except at very low values. There are two complementary PID strategies in ALICE. The first one is based on the assumption that the raw PID signal is not too far from the theoretical one (so-called n_σ cuts), the second one is based on a Bayesian approach.

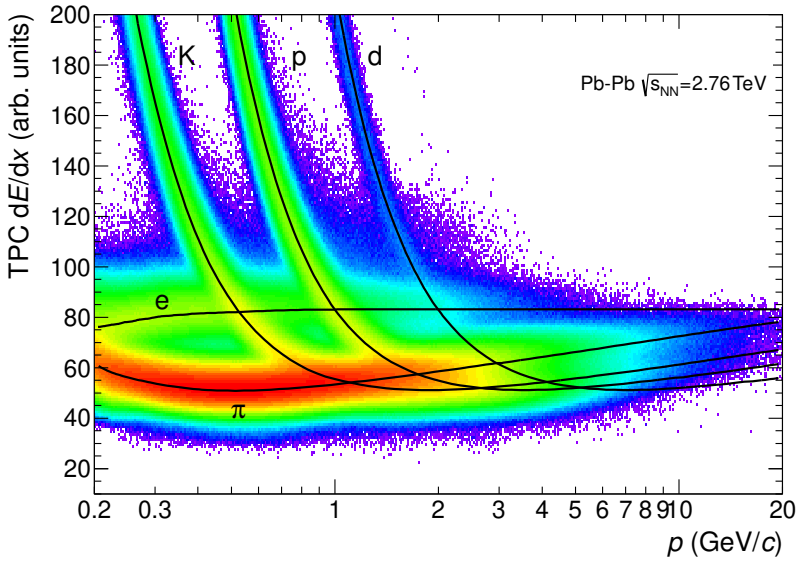

Fig. 1.10: Particle identification using $\mathrm{d}E/\mathrm{d}x$ signals from the TPC detector. Taken from [10].

The spatial points reconstructed in the TPC are matched to the track and fitted using a Kalman filter. Together with the information matched from the ITS, they create a track object that has momentum, charge, number of

TPC clusters, and $\mathrm{d}E/\mathrm{d}x$ data.

Upgrade

The TPC was upgraded during the Long Shutdown 2. During this upgrade, the Multi-Wire Proportional Chambers were replaced by continuously operated chambers based on Gas Electron Multiplier (GEM) technology. The idea of continuously read-out detectors working in trigger-less mode is to read out all minimum bias Pb–Pb data that will be delivered by the LHC at an interaction rate of 50 kHz. That will significantly improve the statistical uncertainty of rare probes that are key to study the QGP. It will also lead to enlarging of all data samples including that for UPCs and will allow for the study of rarer events. Together with the upgrade to GEM chambers, a new read-out front-end electronics was developed to be able to transfer the expected data rate of 3.28 TByte/s into the online data farm.

1.2.4 Time-Of-Flight Detector

The Time-Of-Flight (TOF) detector is responsible for particle identification and triggering. It covers a cylindrical area around the TPC with the same pseudorapidity coverage ($|\eta| < 0.9$). Its length is 741 cm, the internal radius is 370 cm, and the outer one 399 cm. Because of its huge dimensions it was designed as a gaseous detector based on Multi-gap Resistive-Plate Chambers (MRPCs) with 10 gaps of 250 μm. The key aspect of these chambers is that they create a high and uniform electric field. Any ionisation produced by the travelling charged particle will start an avalanche and due to its small size, basically no drift time is present in the signal. That results into an excellent time resolution of 40 ps and an efficiency close to 100 %.

The measured time-of-flight (Fig. 1.11) is used for particle identification in the intermediate momentum range, below 2.5 GeV/c for pions and kaons and up to 4 GeV/c for protons.

The second role of TOF is to provide a L0 trigger input. The MRPCs are arranged into pads of size $\approx 1000\,\mathrm{cm}^2$ and they are the basic logic unit of the trigger. The L0 trigger input can be constructed using a number of fired trigger pads or even a topology pattern, e.g. back-to-back (opposite side hits). This kind of triggers are extremely useful in UPCs.

1.2.5 V0 Detector

The V0 detector is a small-angle detector located along the beam pipe on each side of the interaction point. It consists of two arrays of scintillator counters,

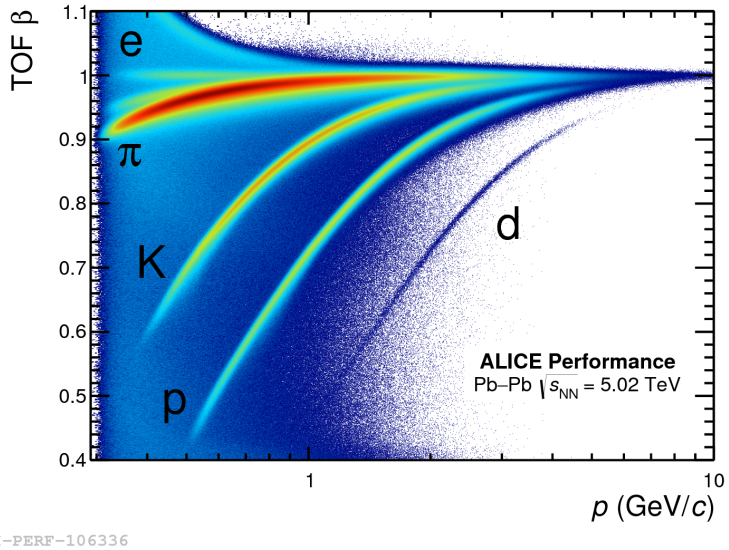

Fig. 1.11: Particle identification using the particle velocity in the TOF detector. Taken from [16].

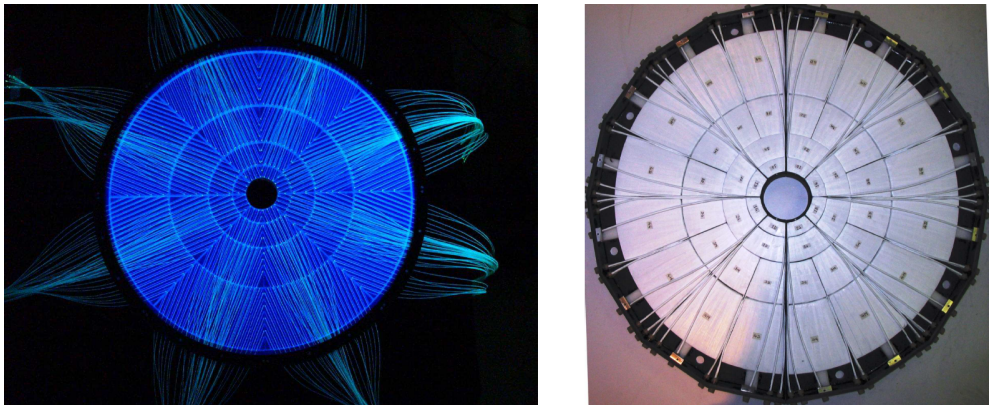

Fig. 1.12: Front view of V0A without the protecting cover (left) and V0C (right) detector. Taken from [9].

V0A and V0C, covering the pseudorapidity regions of $2.5 < \eta < 5.1$ and $-3.7 < \eta < -1.7$. It is made of BC404 scintillating material and read-out using wave-length shifting optical fibres to photo-multipliers. Each of the detectors is segmented into 32 individual counters (cells) arranged in four rings, as shown in Fig. 1.12, providing to the online trigger the number of fired cells and in offline processing also the time information.

The V0 detector has several important functions. Its main task is to

provide a minimum-bias trigger. Another task is to provide an online centrality trigger and using the time information, a rejection of beam-gas events. Also the number of fired cells can be used to distinguish hadronic and ultra-peripheral collisions in the offline analysis. Lastly, the V0 detector plays an important role in the luminosity measurement.

1.2.6 AD Detector

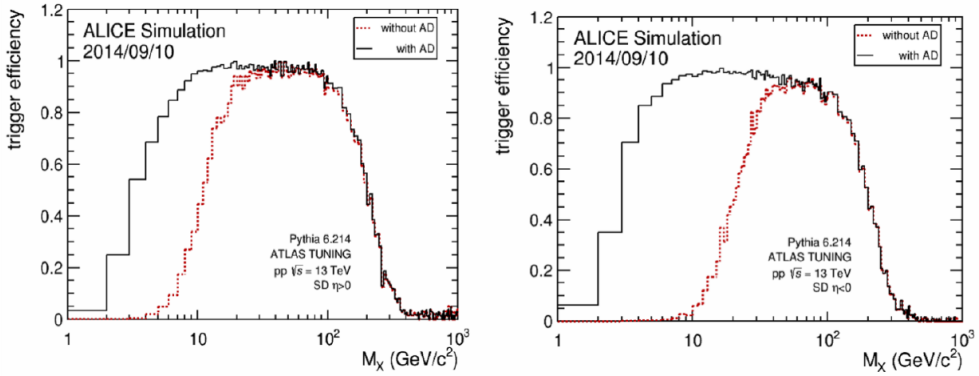

Fig. 1.13: Simulation of the trigger efficiency for single diffractive events (SD) using the AD detector. Taken from [17].

The Alice Diffractive (AD) detector [17] is a forward detector that was added during the LS1 and successfully operated in Run 2. The AD was added in order to increase the sensitivity to lower diffractive masses (Fig. 1.13) and to compensate the loss of Minimum Bias trigger efficiency. Its design and functions are similar to V0, but it covers a higher pseudorapidity range $4.8 < \eta < 6.3$ and $-7.0 < \eta < -4.9$.

The AD detector consists of two arrays of scintillator pads on each side of ALICE: ADA and ADC. Each has two layers of BC404 scintillator segmented into four pads of dimensions $181 \times 216 \times 25\,\mathrm{mm}^3$. A coincidence of both layers is required in order to reduce background and electronic noise. The light produced by charged particles is collected by wave-length shifting bars and transferred through optic fibres to PMTs.

The signal is sent to the preamplifier card, which delivers two signals: one amplified by a factor of 10 that is used for the timing measurement, the second, direct unmodified signal, is used for charge integration. The detector provides a L0 trigger signal.

Upgrade

The functionalities of the detectors V0, T0, and AD were upgraded and merged into a new Fast Interaction Trigger (FIT) detector during LS2. FIT [18] is designed to sustain an interaction rate up to 1 MHz in pp and 50 kHz in Pb–Pb collisions. It will also determine the interaction time with a resolution better than 50 ps. Moreover, it will be used to determine the event multiplicity, the centrality, and the reaction plane. The detector will consist of two Cherenkov arrays (FT0-A and FT0-C), a segmented scintillator detector (FV0), and two scintillator arrays of Forward Diffractive Detector (FDDA and FDDC). All detectors will use common electronics on custom-made boards.

1.2.7 Zero-Degree Calorimeters

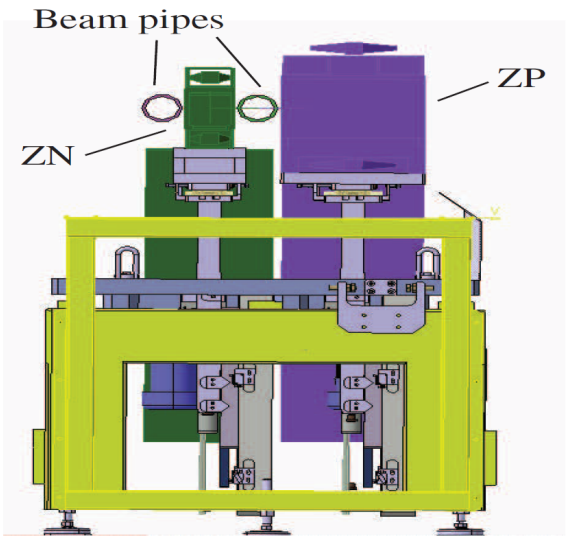

Fig. 1.14: Front view of the ZDC in the data-taking position. Taken from [9].

The purpose of the Zero-Degree Calorimeters (ZDCs) is to measure energy spectra of the spectators[1] in AA collisions. The ZDCs are located on both sides (ZDCA and ZDCC) of the interaction point at a distance of 112.5 m. Each ZDC consists of two detectors, one to detect neutrons (ZN) and the other to detect protons (ZP). On top of that, these hadronic calorimeters are complemented by two electromagnetic calorimeters located 7 m from the IP.

[1] non-interacting nucleons

The proton calorimeter (ZP), covering a pseudorapidity region $6.5 < |\eta| < 7.5$, is placed outside the LHC beam pipe as the proton spectators are deflected by the LHC magnets. The neutron calorimeter (ZN) acceptance is $|\eta| > 8.8$ and it is positioned between the beam pipes, because neutrons are not deflected. The whole ZDC can be moved down when is not used, as shown in Fig. 1.14, to protect it from beam radiation.

An incident particle produces a shower in a dense absorber material, in the case of ZN a tungsten alloy is used because of strong space restrictions between the beam pipes. The shower is detected using Cherenkov radiation in the active material—quartz fibres. The read-out is divided into five photomultiplier tubes.

The signal strength is proportional to the energy deposited in the calorimeter and the calibrated resolution is 20% [19]. Cherenkov calorimeters also provide very fast output signals, therefore the ZDC can be used as an L1 trigger input for different centralities of hadronic collisions. The excellent time resolution is provided by time-to-digital converters (TDCs) and can also be used to exclude events where one of the collided ions was displaced from the nominal bunch position to another RF bucket (so-called "Out-of-bunch pile-up" or "satellite bunches").

1.2.8 Muon Spectrometer

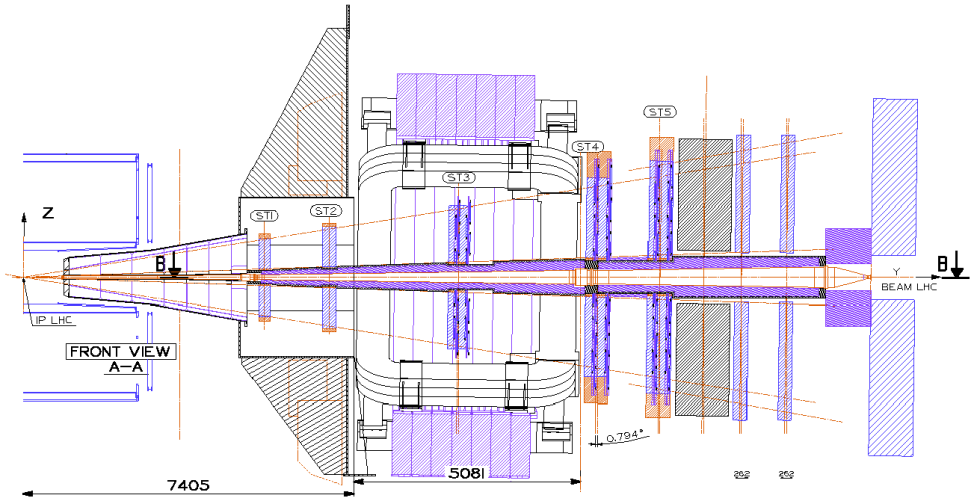

Fig. 1.15: Muon spectrometer layout in the side view. Taken from [9].

The muon spectrometer is responsible for muon measurement in the pseudorapidity region $-4.0 < \eta < -2.5$. This allows for heavy-quark vector

mesons resonances to be measured in the $\mu^+\mu^-$ decay channel. This is especially useful in UPCs, where heavy-quark vector mesons are great probes to study saturation in QCD.

The layout of the muon spectrometer is shown in Fig. 1.15 and it consists of several components located in the C-side of ALICE. Closest to the interaction point, there is a front passive absorber to absorb hadrons and photons. It is dominantly made out of concrete and carbon to limit energy loss and small-angle scattering that affects the detector resolution. The tracking device consists of 10 layers of high-granularity resistive-plate chambers coupled into 5 "Tracking chambers". In the middle of the spectrometer, a dipole magnet of $B_{\text{nom}} = 0.7\,\text{T}$ bends the travelling muons and enables a momentum measurement. At the end, a passive muon wall is followed by four planes of trigger chambers.

Upgrade

The muon tracking and vertexing capabilities will be improved by the installation of the new Muon Forward Tracking (MFT) detector [20]. The MFT detector is placed between the ITS and the front of the absorber covering the muon spectrometer acceptance. It is designed as a CMOS silicon pixel detector based on ALPIDE chips, the same that are used in the upgraded ITS.

In order to achieve a designed read-out rate of 100 kHz, a new architecture where the signals are continuously sampled will be used. The dead time free data read-out will support continuous, self-triggered read-out mode and triggered mode [21].

1.3 Data processing

1.3.1 Trigger and Data Acquisition Systems

The trigger system is responsible for selecting common and rare events at a rate that will be managed by the bandwidth of the Data Acquisition (DAQ) system. The trigger inputs from detectors are processed by the ALICE Central Trigger Processor (CTP) that can be configured according to LHC conditions, physics program, and actual detector condition and decides if an event is recorded or not.

The trigger itself is splitted into three levels according to the time needed for the decision. The fastest one is Level 0 (L0) that provides the decision back to the detectors within $1.2\,\mu$s, where most of the latency comes from

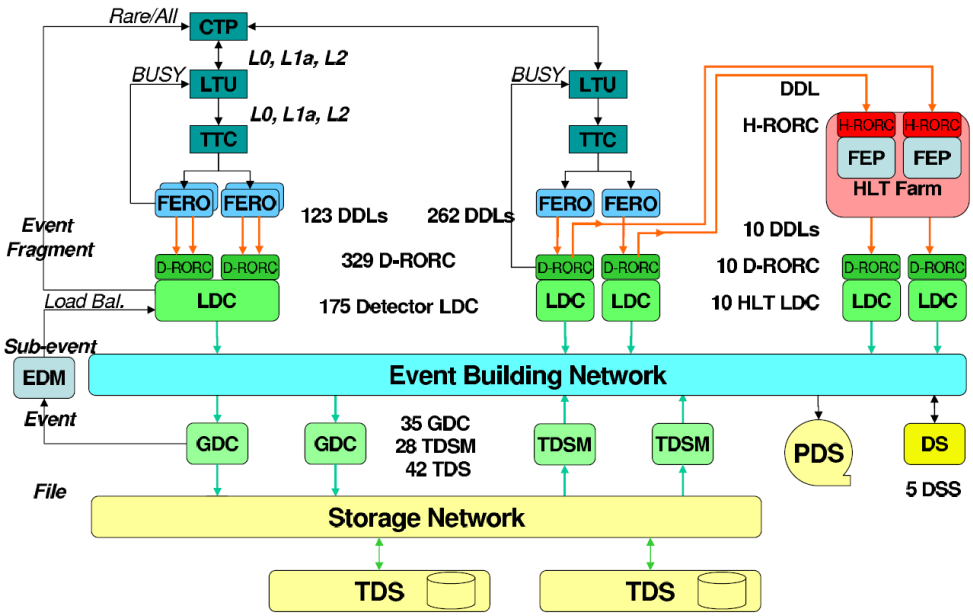

Fig. 1.16: Architecture of the ALICE Data Acquisition (DAQ) system. Taken from [9].

signal generation and cable delays. It is followed by the Level 1 (L1) at 6.5 μs that contains all trigger inputs that are not fast enough for L0. The final Level 2 (L2) at 88 μs waits until the past-future protection[2] is ensured.

After the trigger decision, the data are sent from Front-End Read-Out (FERO) detector electronics through the Detector Data Link (DDL) protocol to the Data Acquisition system. The scheme of the ALICE DAQ system can be seen in Fig. 1.16. The data from detectors are processed by the LDCs (Local Data Collectors) that are selected for each detector and create sub-events. Then data are collected by GDCs (Global Data Collectors), where the event data are completed by Event Builder and sent to Permanent Data Storage at the CERN computing centre. These data are called the RAW data.

Upgrade

The ALICE Central Trigger System will be upgraded for Run 3. It is designed on a completely new hardware and new Trigger and Timing System using FPGA boards [22]. The main challenge is the increase in interaction rate

[2]It ensures that only one central collision happens within the time window, as more of them would cause the event to be unreconstructable.

from 8 kHz to 50 kHz for Pb–Pb and from 100 kHz to 2 MHz for p–p and p–A. The main goal of the new ALICE trigger system is to select all these collisions. In addition, it will be operated in two modes, a continuous mode and a triggered mode. In both modes the main function is to provide a time flag rather than select events, since the event selection will be done by a very large processor farm in real time.

1.3.2 Data reconstruction

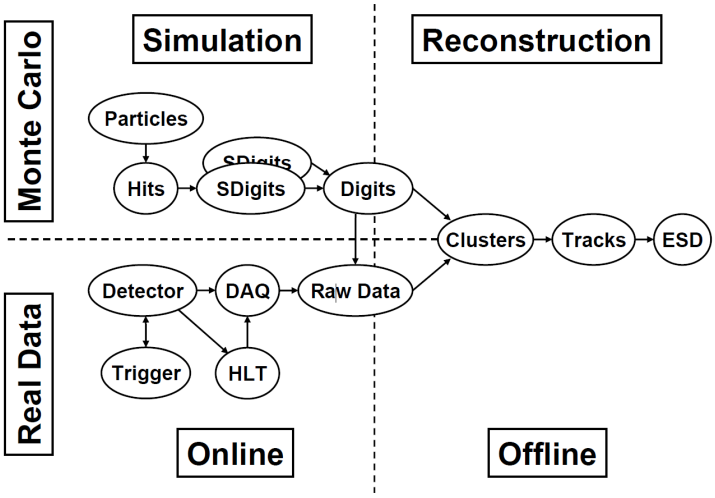

Fig. 1.17: Simulation and reconstruction scheme using the AliRoot framework. Taken from [9].

The recorded data (events) are organised into larger groups called "runs". When an Experiment Control System (ECS) operator starts the data taking, a new run is created. Every run has an unique integer number larger by one than the previous one. Not all runs are devoted to physics, there are also calibration runs for detectors and technical runs for testing and maintenance. Runs are usually stopped because of a technical failure of the detector, a trigger reconfiguration or the LHC beam dump.

Several runs that are taken under the similar LHC configuration (LHC energy, bunch distribution, beam particles) is called a "period". The period name consists of the last two digits of the year and a letter increasing in alphabetical order to distinguish different periods (e.g. LHC15o, LHC17n,...).

The calibration data taken during the run are stored as objects in the Offline Condition DataBase (OCDB). They contain data such as pedestal values, detector alignment, voltages, pixel maps, etc. These parameters are

important during data reconstruction and also in Monte Carlo simulations as they provide the detector response.

The event reconstruction proceeds starting on the RAW data and is performed using AliRoot. AliRoot [23] is a C++ Object-Oriented framework based on the ROOT [24] system complemented by the AliEn [25] system, which gives access to the computing grid.

The reconstruction activities performed by AliRoot can be seen in Fig. 1.17. The process of reconstruction starts with individual steps for each detector, e.g. cluster finding. Clusters are found by the grouping of several neighbouring detector hits by a dedicated algorithm. Then the primary vertex is reconstructed followed by the track reconstruction using a Kalman filter [26] and particle identification. Finally, the secondary vertices from uncharged particles, cascades, and kink decays are found. The output of the reconstruction is the Event Summary Data (ESD), which contains information about charged particle tracks, particle identification, and information about decays or cascade topology.

Afterwards, Analysis Object Data (AOD) are produced with a content condensed from the ESD and are filled with specific physical information like momentum, energy and other. The working group analyses are performed via so-called LEGO Trains that are sent to the GRID Tier-1 centres in order to be processed. They provide large computing capacities and can merge analyses of several users working on the same dataset (both ESD and AOD) to save CPU power. The end-user analysis starts from condensed AODs (or nanoAODs) produced in trains and it is designed for local system processing.

AliRoot is also used for detector simulation. Particles that are produced by a Monte Carlo generator are passed to the AliRoot framework. The particle response in detectors is simulated using the full geometry of the ALICE detector created in ROOT, and the interaction with the detector material is simulated using the GEANT 3 [27], GEANT 4 [28] or FLUKA [29, 30] packages. In the end, the output is stored in the same RAW format as real data. From this point onwards the MC and real data are processed in exactly the same way. On top of that, MC data contain also input particle information to study specific kinematic region or detector effect afterwards.

Upgrade

The AliRoot framework will be upgraded for Runs 3 and 4 to a new control system called O2 (Online–Offline) [31] that is designed for a maximal reduction of the data volume read out from the detector as early as possible during the data-flow. The data volume reduction will be achieved by reconstructing the data in several steps synchronously with data taking.

Chapter 2

Theory and models

2.1 Ultra-peripheral collisions

The protons or ions are accelerated in current colliders to relativistic velocities and due to the Lorentz contraction, their shape is pancake-like. Also, the electromagnetic field of the accelerated particle is Lorentz-contracted and can be viewed as a cloud of quasi-real photons [32]. The number of photons scales with Z^2. The photon emitted from one nucleus can interact with a photon emitted from the other nucleus (photon–photon interaction) or a photon is emitted from one of the nuclei and interacts with a target nucleus. The formalism of the interaction depends on the model. It can be viewed as an interaction through the Pomeron in the Regge theory, a fluctuation of the photon into a vector meson in the Vector Dominance Model, or a fluctuation into a quark–antiquark pair in the Color Dipole Model. We will discuss these options below.

When the impact-parameter[1] b of colliding protons (ions) is larger than the sum of their radii (see Fig. 2.1), it is called an ultra-peripheral collision (UPC). The UPCs typically occur at impact-parameters of several tens (hundreds) of femtometers, where the incoming ions do not overlap and are beyond the range of the strong force. It results into a suppression of hadronic interactions and photoproduction of vector mesons becomes the dominant process [34]. However, from the production mechanism can be expected that the vector meson photoproduction could also occur at peripheral collisions as the strong EM field is still present and the target nucleus is almost intact. This was recently confirmed by ALICE that observed an excess in the expected hadroproduction of J/ψ which was attributed to coherent J/ψ photoproduction in peripheral collisions [35].

[1] The perpendicular distance between the centres of colliding particles.

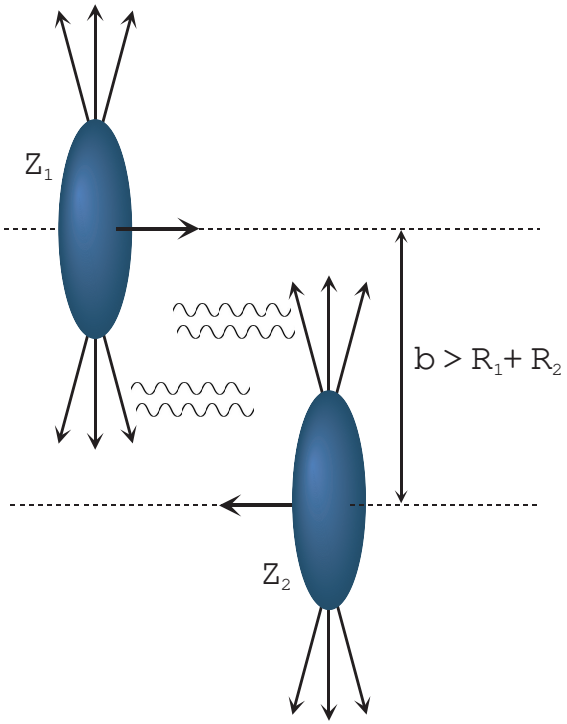

Fig. 2.1: A sketch of an ultra-peripheral collision. Taken from [33].

2.1.1 The flux of virtual photons

In 1924, Enrico Fermi calculated the excitation and ionisation of atoms by means of energetic alpha-particles. He realised that the calculations can be simplified if the electromagnetic field generated by the projectiles is replaced by an equivalent pulse of real photons incident on the atom [32]. This brilliant idea denoted as the equivalent photon approximation (EPA) was further developed by Weiszäcker [36] and independently by Williams [37]. Fermi's method became widely known as the Weiszäcker-Williams approximation (WWA) and can be written as:

$$\sigma_X = \int d\omega \frac{n\left(\omega\right)}{\omega} \sigma_X^{\gamma}\left(\omega\right) \ , \tag{2.1}$$

where $\sigma_X^{\gamma}\left(\omega\right)$ is the photonuclear cross section, $n\left(\omega\right)$ is the number of equivalent photons incident on the target, and the integration runs over all photon energies ω.

The flux of photons per unit area $N(\omega, b)$ can be calculated as a Fourier transform of the electromagnetic field of the moving charged particle. The

result is presented as [38]:

$$N(\omega, b) = \frac{Z^2\alpha\omega^2}{\pi^2\gamma^2\hbar^2\beta^2c^2}\Big(K_1^2(x) + \frac{1}{\gamma^2}K_0^2(x)\Big). \tag{2.2}$$

where $x = \omega b/\gamma\beta\hbar c$, Z is the ion charge, $\alpha = 1/137$, βc is the particle velocity and K_0 and K_1 are modified Bessel functions. The first term $(K_1(x)^2)$ is responsible for the flux of transversely polarised photons and dominates for ultra-relativistic particles. The second term is the flux for longitudinally polarised photons.

Integrating $n(\omega) = \int N(\omega, b)d^2b$ over the impact-parameter we can obtain the flux in Eq. 2.1 as:

$$n(\omega) = \frac{2Z^2\alpha}{\pi\beta^2}\Big[\xi K_0(\xi)K_1(\xi) - \frac{\xi^2}{2}(K_1^2(\xi) - K_0^2(\xi))\Big] \tag{2.3}$$

where $\xi = \omega b_{\min}/\gamma\beta\hbar c = 2\omega R_A/\gamma\beta\hbar c$. The integration is done for $b > b_{\min} = R_1 + R_2$ with $R_A = 1.2A^{1/3}$ fm, in other words, colliding particles do not overlap in the impact-parameter plane, called the hard sphere approximation. From Eq. 2.2 is now clear that the flux is proportional to the electric charge squared Z^2.

2.1.2 Exclusive vector meson photoproduction

Let's describe the exclusive vector meson production that is the main topic of this work. This UPC process produces only a vector meson in the final state:

$$A + A \to A + A + V. \tag{2.4}$$

A photon emerging from one of the nuclei interacts with the other target nucleus producing a vector meson. The photon transverse momentum in this process is small, it implies that the final state p_T will also be small. The final state can be identified through its decay products, which are commonly two pions or leptons. The multiplicity of these events is therefore much smaller than that of hadronic interactions and usually the events can be fully reconstructed. This provides a clean experimental signature to trigger on these events and to compute the full kinematics. An example of such event can be seen in Fig. 2.2.

2.1.3 Production off protons

The photoproduction of a vector meson off protons can be elastic or dissociative. In the former, the proton remains in its ground state, in latter, it gets excited and breaks.

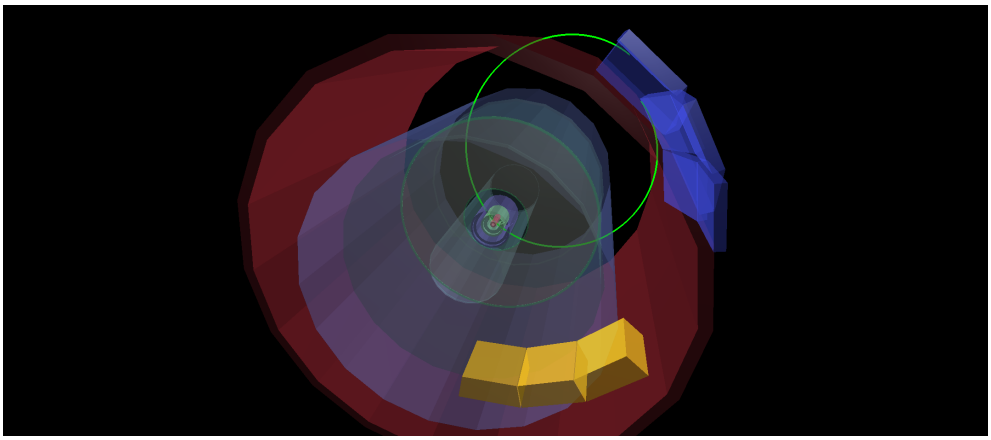

Fig. 2.2: An example of an UPC event in the central barrel of ALICE. This event is a candidate for $\rho^0 \to \pi^+\pi^-$.

The elastic photoproduction of the ρ^0 in p–Pb UPCs is shown in Fig. 2.3. A photon is produced by the Pb-ion. It may also be produced by a proton, however this channel is suppressed by a factor of 82^2 due to the flux proportionality to the electric charge squared as shown in Eq. 2.3. The photon then interacts with the gluon field of a proton and produces a vector meson (e.g. a ρ^0 meson). We will describe several concepts of this interaction in the next chapter. Now let us focus on the kinematics of this interaction.

The kinematics of this process can be described by the lead-proton centre-of-mass energy squared s, the photon-proton centre-of-mass energy $W_{\gamma p}$, the four-momentum transferred squared at the proton vertex t, and the four-momentum transferred at the Pb vertex Q^2. In the elastic case, the t and Q^2 are relatively small. The transverse momentum p_T of a vector meson can be related to t through the formula $p_T^2 \approx -t$ and is of the order of 300 MeV/c.

As the vector meson is the only produced particle in the final state, the photon-proton centre-of-mass energy $W_{\gamma p}^2$ can be related to the rapidity of the vector meson:

$$W_{\gamma p}^2 = 2E_p M_{VM} \exp(\pm y), \tag{2.5}$$

where E_p is the beam target energy in the laboratory frame, M_{VM} is the vector meson rest mass, and y its rapidity.

The cross section of the vector meson is given by the photon-proton cross section and the photon flux:

$$\frac{d\sigma_{pA}(y)}{dy} = N_{\gamma/A}(y, \{b\})\, \sigma_{\gamma p}(y), \tag{2.6}$$

where $\sigma_{\gamma p}(y)$ is the photoproduction cross section and $N_{\gamma/A}(y, \{b\})$ is the

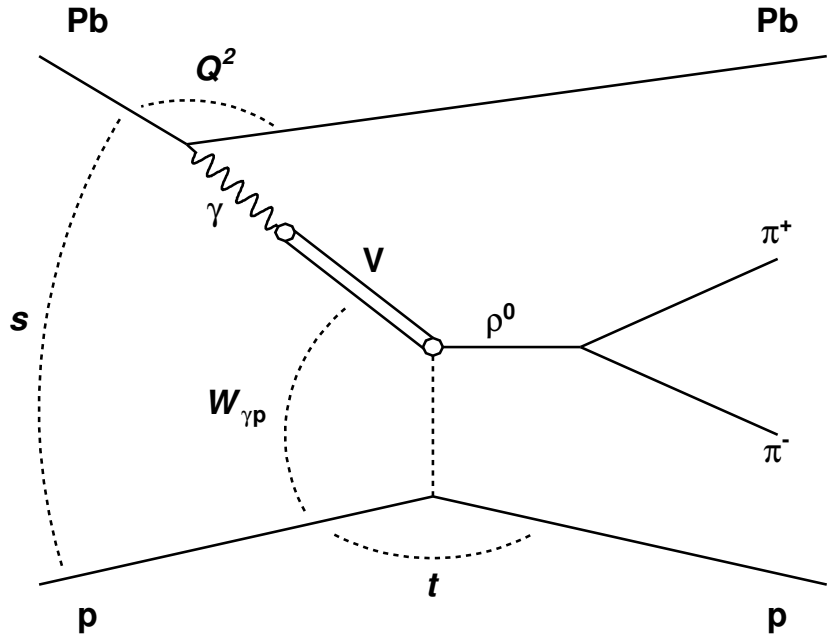

Fig. 2.3: Kinematics of elastic ρ^0 photoproduction in p–Pb ultra-peripheral collisions in the vector dominance model. The most probable ρ^0 decay channel to $\pi^+\pi^-$ is shown.

photon flux, where $\{b\}$ denotes the range of impact-parameter values sampled by the process.

The dissociative photoproduction occurs when the proton is excited by the interaction and dissociates. It means that new particles are created when the proton breaks up, forcing the transverse momenta of the vector meson to higher average values above 1 GeV/c.

2.1.4 Heavy-ion production

The kinematics of vector meson photoproduction in heavy-ion collisions is very similar to that off protons we described above. However, the interaction can be coherent, if the photon interacts with the whole nucleus, or incoherent where the photon interacts with one of the nucleons in the nucleus.

The main experimental difference between the coherent and incoherent interaction is the mean transverse momentum of the produced particle. From Heisenberg principle of uncertainty, it is inversely proportional to the target size $p_T \approx 1/2R$ resulting in much smaller p_T in the coherent interaction,

where the whole nucleus is a target ($\langle p_T \rangle \approx 60\,\mathrm{MeV}/c$), than in the incoherent one, where the inner nucleon (or a parton) is taken as a target particle ($\langle p_T \rangle \approx 300\,\mathrm{MeV}/c$). Moreover, the incoherent interaction makes the nuclei to break up producing particles in the forward rapidity. Usually the forward neutrons can be easily detected by the zero-degree calorimeters. Forward neutrons can also be produced during the coherent interaction by another producing mechanisms that we will describe in Sec 2.1.6.

In nucleus-nucleus collisions, both particles can be a source or a target as is sketched in Fig. 2.4. We can write the total cross section as a sum of both contributions:

$$\frac{d\sigma_{AA}(y)}{dy} = N_{\gamma/A}(y, \{b\})\,\sigma_{\gamma A}(y) + N_{\gamma/A}(-y, \{b\})\,\sigma_{\gamma A}(-y)\,. \tag{2.7}$$

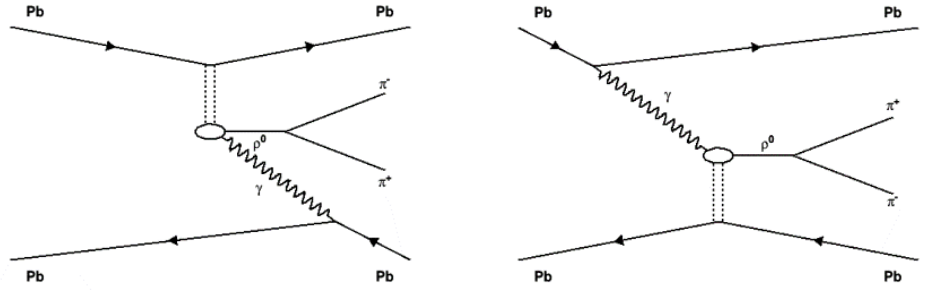

Fig. 2.4: Both contributions to the ρ^0 photoproduction in Pb–Pb UPCs.

2.1.5 Dilepton pairs

In the introduction we mentioned that the photon interacts not only with a target nucleus, but it may also interact with the photon from the other nucleus. Two-photon interactions are an exceptionally interesting topic as many final states can be produced; starting with meson pair production, fermion pairs, up to exotic mesons, Higgs production or super-symmetry particles beyond the Standard Model. An overview can be found for example in [38].

We will discuss only the dilepton production (Fig. 2.5) as it has large cross section and similar kinematics which cause an important background process for vector meson analyses.

The lepton (or quark) pair can be produced in two-photon collision if the invariant mass of the $\gamma\gamma$ system is above the threshold $\sqrt{s} > 2m_f$. The cross

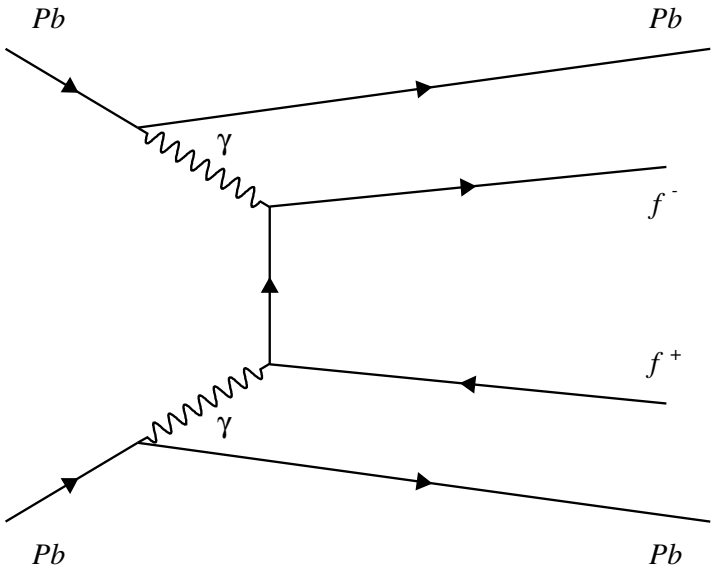

Fig. 2.5: Dilepton (fermion) pair production in Pb–Pb ultra-peripheral collisions.

section of dilepton production in the lowest order of QED is given by the following formula:

$$\sigma(\gamma\gamma \to f^+f^-) = \frac{4\pi\alpha^2 Q_f^4 N_c}{s}\beta\left[\frac{3-\beta^4}{2\beta}\ln\frac{1+\beta}{1-\beta} - 2 + \beta^2\right], \tag{2.8}$$

where $\beta = \sqrt{1-4m_f^2/s}$ is the velocity of the fermion in the $\gamma\gamma$ rest frame. The production of $\tau^+\tau^-$ is not observed because of its large mass and quick decay. However, both e^+e^- and $\mu^+\mu^-$ pairs will be present in data.

2.1.6 Electromagnetic dissociation

As heavy nuclei have a large electric charge, the probability of additional, independent, purely electromagnetic interactions is large. This can be explained as an exchange of additional photons during the ultra-peripheral collision. An example of one of the contributions is shown in Fig. 2.6. This processes are usually called electromagnetic or Coulomb dissociation (EMD) [39]. We can also distinguish a single dissociation, where one of the nuclei is excited and breaks up, or mutual EMD, where both of them get excited and break up. It was proposed that these photons are emitted independently on vector meson production and a factorisation can be used [40].

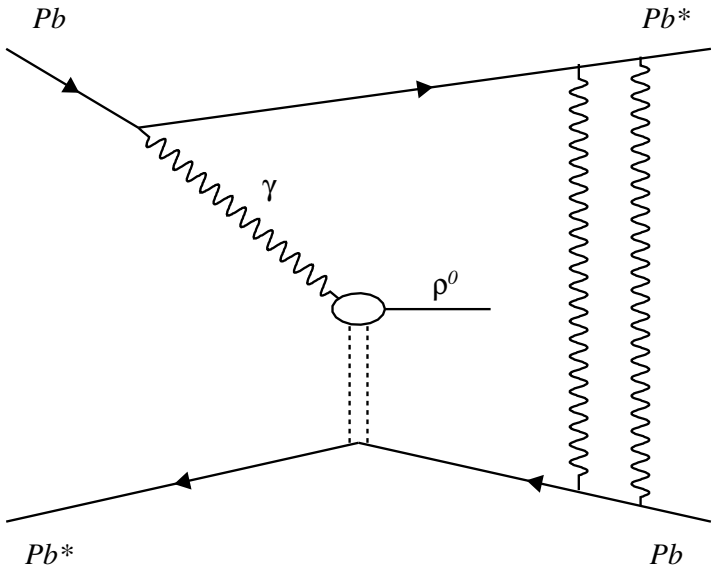

Fig. 2.6: Dominant diagram for vector meson production with nuclear excitation.

The excitation of a nucleus leads to several possible decays depending on the energy of the photon as shown in Fig. 2.7. In particular, a Giant Dipole Resonance (GDR) [42] can be excited in the nucleus at soft energies. In GDR the protons and neutrons oscillate against each other, which results in the radiation of one or more neutrons. These neutrons will travel in the direction of the beam and can be detected using zero-degree calorimeters. Above the GDR region the situation becomes more complicated leading to multiple neutron emission, delta resonances, and multiple charged-particle production at high rapidities.

The EMD is an important process since it sets the beam lifetime limit at LHC energies and it is used to measure the luminosity. In recent years, the EMD was studied at ALICE using lead nuclei [19] and the experimental results were correctly reproduced by theoretical predictions of the RELDIS model [43].

2.2 Photoproduction models

Now we will mention several models based on both theory and phenomenology that are commonly used in UPCs. All models are based on Eq. 2.6 which has two factors: the photon flux and the photonuclear cross section. There

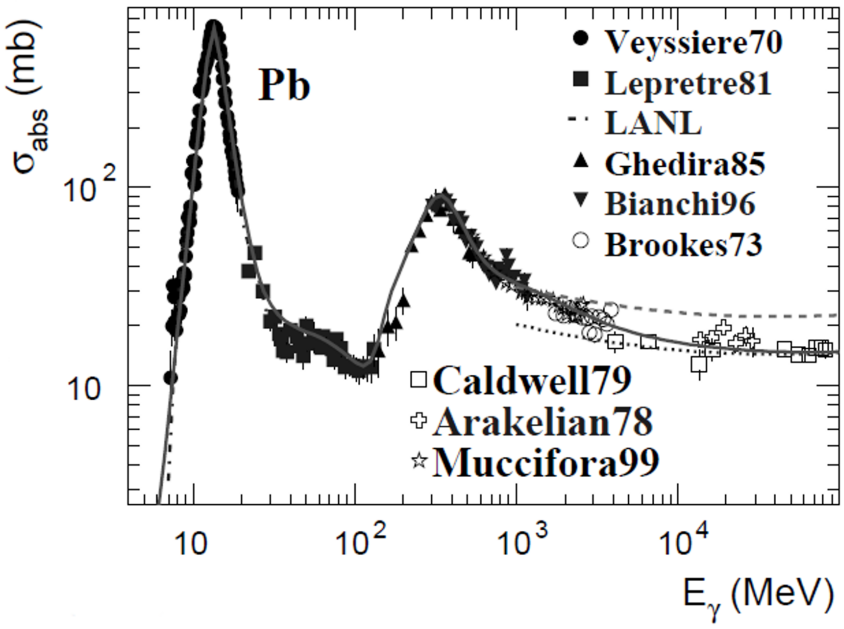

Fig. 2.7: EMD cross section as a function of photon energy. The first peak corresponds to the GDR, second to the delta resonance. Taken from [41].

is different approach of models in both factors.

2.2.1 Vector Meson Dominance

Vector meson dominance (VMD) is a model developed by J.J. Sakurai [44] who applied Yang-Mills theory to strong interaction back in 1960s. According to the VMD model, a photon is a superposition of a pure electromagnetic photon and vector meson (the largest contribution is given by light vector mesons such as ρ, ω and ϕ). The model was lately extended and denoted as generalized vector meson dominance (GVMD) model [45].

The application of the GVMD to coherent vector meson photoproduction in UPCs is given by Klein and Nystrand in Ref. [46] and [39]. In these calculations a photon is approximated by a produced vector meson V (calculation of $\gamma + \mathrm{A/p} \rightarrow V + \mathrm{A/p}$ is approximated by $V + \mathrm{A/p} \rightarrow V + \mathrm{A/p}$). The optical theorem is used to relate this process to the total cross section as:

$$\left.\frac{d\sigma(\gamma A \rightarrow VA)}{dt}\right|_{t=0} = \frac{\alpha\sigma_{tot}^2(VA)}{4f_v^2} \tag{2.9}$$

where f_v is the vector meson-photon coupling.

The total cross section is computed using the classical Glauber model as follows:

$$\sigma_{tot}(VA) = \int d^2\vec{r}\Big(1 - e^{-\sigma_{tot}(Vp)T_{AA}(\vec{r})}\Big), \tag{2.10}$$

where $T_{AA}(\vec{r})$ is the nuclear thickness function. The optical theorem is again used at the nucleon level to obtain the vector meson-nucleon cross section:

$$\sigma^2_{tot}(Vp) = 16\pi \frac{d\sigma(Vp \to Vp)}{dt}\Big|_{t=0}. \tag{2.11}$$

Using VMD we can obtain:

$$\frac{d\sigma(\gamma p \to Vp)}{dt}\Big|_{t=0} = \frac{4\pi\alpha}{f_v^2} \;\; \frac{d\sigma(Vp \to Vp)}{dt}\Big|_{t=0}, \tag{2.12}$$

where the nucleon cross section is parametrised by the following formula

$$\frac{d\sigma(\gamma p \to Vp)}{dt}\Big|_{t=0} = b_V(XW^{\epsilon} + YW^{-\eta}). \tag{2.13}$$

and fitted to experimental data from HERA to obtain individual parameters.

2.2.2 Colour dipole model

In the colour dipole model [47, 48, 49], the interaction is explained by the fluctuation of a photon into a quark-antiquark pair which forms a colour dipole that exchange a colourless object with the hadron target via the strong interaction and then turns into a vector meson. This is shown schematically in Fig. 2.8.

The transverse size of the pair is denoted by $\vec{r}$ and the quark carries a fraction z of the photon's momentum. There is an assumption that in the target rest frame, the dipole lifetime is much longer than the lifetime of its interaction with the target hadron. First, the incoming virtual photon fluctuates into a quark–antiquark pair long before the interaction. Then the $q\bar{q}$ pair scatters elastically on the target, and finally the $q\bar{q}$ pair recombines to form a virtual photon (or vector meson in the case of photoproduction). The main ingredients for the calculation of the cross sections are the vector meson wave function and the dipole-hadron scattering amplitude, which is dependent on the modelling of the QCD dynamics at high energies. In the perturbative region, that is, for small dipole sizes $\vec{r}$, the dipole cross section corresponds to the exchange of a gluon ladder.

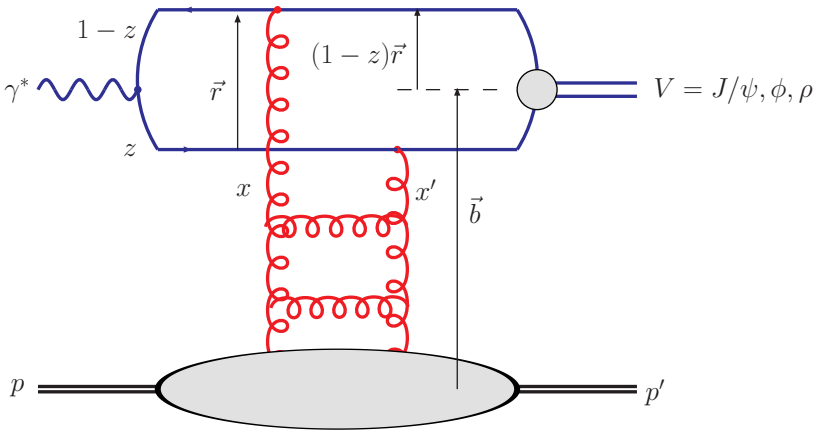

Fig. 2.8: The vector meson photoproduction in the dipole representation. Taken from [49].

2.3 Cross section predictions

2.3.1 STARlight

STARlight [50] is an event generator that provides an input for Monte Carlo (MC) simulations of UPC processes. It is optimised to describe processes at RHIC and LHC energies with final states that are visible in central detectors.

The STARlight program uses a two-step process: first it calculates the cross section as a function of W, y and p_T, second; it generates Monte Carlo events which can be used to determine the cross section in specific kinematic regions of the detector or to establish the detector response and efficiencies.

STARlight can simulate the collision of various nuclei. Heavy nuclei can be modelled both as hard spheres or using the Woods-Saxon mass distribution, where the radius is set to $R_A = 1.2\,\mathrm{fm} \cdot A^{1/3}$ and the skin depth to 0.53 fm. For several of the most common ones (gold, lead, copper) measured parameters of nucleus radius are used. The light nuclei ($Z \leq 6$) are modelled using a Gaussian mass distribution. The flux calculations are based on the equivalent photon approximation.

The cross section calculation are computed in several ways. For lepton pairs in two-photon interactions, a Breit-Wheeler formula is used. Vector meson photoproduction on proton targets is parameterised using HERA data and coherent production on nuclear targets is determined using a classical Glauber calculation as described above. There are also multiple options for generating p_T spectra, e.g. it can be assumed that photoproduction on the two nuclei is independent or an interference term can be included.

STARlight can also be interfaced with the DPMJET III event generator.

Vector mesons are usually decayed within STARlight taking the spin state into account. More complex cases (multiple final states) are decayed using PYTHIA.

2.3.2 GKZ

The GKZ (Guzey, Kryshen and Zhalov) model is introduced in [51]. It is based on a modified vector meson dominance model combined with the Gribov–Glauber model of nuclear shadowing. The vector meson dominance model was upgraded to include the contribution of high-mass fluctuations of the photon according to QCD constraints. The Gribov–Glauber approach was necessary to take into account both elastic and inelastic diffraction in the intermediate states contributing to the shadowing correction.

The GKZ model proved to describe the data on elastic ρ^0 photoproduction on nuclei in heavy ion UPCs in the $7\,\text{GeV} < W_{\gamma A} < 46\,\text{GeV}$ energy range at RHIC and the LHC (Run 1). The model then predicts the coherent ρ^0 photoproduction cross section in Pb–Pb [52] and Xe–Xe [53] UPCs at energy that is covered by the LHC in Run 2..

2.3.3 CCKT

This model by Čepila, Contreras, Křelina and Tapia (CCKT) [54] is based on the colour dipole model with the structure of the nucleon in the transverse plane described by so-called hot spots. Hot spots are regions of high gluonic density and their number grows with decreasing Bjorken-x. The number of hot spots also depends on the energy of the photon–target interaction in the version extended to be applied to nuclei [55]. The nuclear effects in the model are implemented along the ideas of the Glauber model proposed in [56].

The CCKT reproduced the $F_2(x, Q_2)$ data from HERA at the relevant scale as well as the exclusive and dissociative J/ψ photoproduction data from H1 and ALICE. The model predicts a maximum in the observed cross section for dissociative production that is a clear signature for gluon saturation at the LHC and future collider energies. Predictions of the model are made for exclusive and dissociative production of ρ^0, J/ψ, and Υ(1S) off protons as well as for coherent and incoherent photoproduction of ρ^0 off Xe, Au, and Pb nuclei targets. They also proved that the coherent photonuclear production of ρ^0 is sensitive to fluctuations in the subnucleon degrees of freedom at RHIC and LHC energies.

2.3.4 GMMNS

The GMMNS (originally GM) model by Goncalves, Machado, Morerira, Navarra and dos Santos [57, 58] describes exclusive vector meson photoproduction in pp, pPb and PbPb collisions at Run 1 (GM) and Run 2 (GMMNS) LHC energies using the colour-dipole formalism providing gluon saturation effects. An updated version of different models (IIM [59], bCGC, impact-parameter Colour Glass Condensate, and IP-SAT) of the dipole scattering amplitude, which take into account the nonlinear effects of the QCD dynamics, is used in GMMNS. Moreover, the model uses two different vector meson wave functions (boosted Gaussian and Gaus-LC).

2.3.5 $\mathbf{n^{O}_{O}n}$

The $\mathbf{n^{O}_{O}n}$ [60] is a generator of forward neutrons for ultra-peripheral collisions. As we discussed above (Sec.2.1.6), forward neutrons produced at beam rapidities are a common effect in UPCs, especially in coherent photoproduction of vector mesons due to the large effect of GDR.

The $\mathbf{n^{O}_{O}n}$ generator is a ROOT based program that can be interfaced with existing event generators or with theoretical calculations. Photon energies from the accompanying process are loaded from the interfaced calculation. The nuclear break-up probabilities are computed using existing data and the comparison to RELDIS shows an excellent agreement of both models. The produced neutrons are generated, boosted to the laboratory frame and stored as a TParticle ROOT object, so the output can be easily integrated with simulation programs of experiments at RHIC and LHC.

Chapter 3

Previous measurements of ρ photoproduction

In this chapter, we will describe the ρ^0 meson and its properties. Then the Söding and Ross-Stodolsky models describing the ρ^0 invariant mass spectrum are introduced. Last part of this chapter summarises previous measurements on ρ^0 photoproduction at HERA, RHIC, and LHC accelerators.

3.1 The ρ vector meson

The ρ resonance was discovered at Brookhaven National Laboratory in 1961 [61]. The $\rho(770)^0$ belongs to the family of light unflavored vector mesons ($J^{PC} = 1^{--}$) with quark content $\frac{1}{\sqrt{2}}\left(u\bar{u} - d\bar{d}\right)$.

The determination of its mass $m_{\rho^0} = (775.26 \pm 0.25)\,\mathrm{MeV}/c^2$ is very difficult as it has a wide full width $\Gamma_{\rho^0} = (149.1 \pm 0.8)\,\mathrm{MeV}/c^2$. However, a downward shift of its mass in photoproduction is observed, as we will discuss below, resulting in $m_{\rho^0} = (769.0 \pm 1.0)\,\mathrm{MeV}/c^2$ and $\Gamma_{\rho^0} = (151.7 \pm 2.6)\,\mathrm{MeV}/c^2$. The mean lifetime is $4.5 \times 10^{-24}\,\mathrm{s}$ and it decays dominantly into a $\pi^+\pi^-$ pair. The leptonic and four-pion decays are suppressed and occur with a branching ratio of about 10^{-5} [62].

3.1.1 Söding model

The first experiments on ρ^0 photoproduction showed a downward shift of its invariant mass and a skewing of its peak. A mechanism was suggested by Söding in 1965 [63].

Since pion pairs can be produced without first producing a ρ^0, there will be a background of non-resonant p-wave pion pairs (Fig. 3.1 left). This

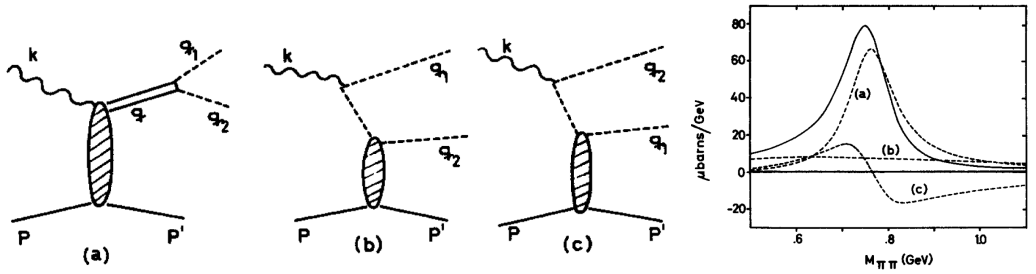

Fig. 3.1: Left: Diagrams used by Söding: (a) production of ρ^0 , (b) and (c) non-resonant production of pions. Right: The effect on the invariant mass spectrum (a) Breit-Wigner resonant part, (b) non-resonant contribution and (c) an interference term. Taken from [63].

background will interfere with the pions produced by ρ^0 decay, resulting in a mass shift. Therefore, the invariant mass distribution of $\rho \to \pi^+\pi^-$ can be described by the Söding formula that consists of two terms: the ρ^0 Breit-Wigner (BW_ρ) function and the non-resonant amplitude B that describes the non-resonant pion background (Fig. 3.1 right):

$$\frac{d\sigma}{dm_{\pi\pi}} = |A \cdot BW_\rho + B|^2, \tag{3.1}$$

where A is the normalisation factor of the ρ Breit-Wigner (BW_ρ) function and the relativistic Breit-Wigner function of the ρ^0 is:

$$BW_\rho = \frac{\sqrt{m_{\pi\pi} \cdot m_{\rho^0} \cdot \Gamma(m_{\pi\pi})}}{m^2_{\pi\pi} - m^2_{\rho^0} + i m_{\rho^0} \cdot \Gamma(m_{\pi\pi})}, \tag{3.2}$$

where the mass-dependent width $\Gamma(m_{\pi\pi})$ is given by

$$\Gamma(m_{\pi\pi}) = \Gamma(m_{\rho^0}) \cdot \frac{m_{\pi\pi}}{m_{\rho^0}} \cdot \left(\frac{m^2_{\pi\pi} - 4m^2_\pi}{m^2_{\rho^0} - m^2_\pi} \right)^{3/2}. \tag{3.3}$$

Very close to ρ^0 mass the ω meson can be produced with its mass $m_\omega = (782.66 \pm 0.13)\,\mathrm{MeV}/c^2$ and its width $\Gamma_\omega = (8.68 \pm 0.13)\,\mathrm{MeV}/c^2$ [62]. Therefore, an updated formula [64] with an extra term to take into account the contribution of the ω is also used:

$$\frac{d\sigma}{dm_{\pi\pi}} = |A \cdot BW_\rho + B + C \cdot \exp(i\Phi) \cdot BW_\omega|^2, \tag{3.4}$$

where C is the normalisation factor of the ω Breit-Wigner (BW_ω) and Φ is the mixing phase. Similarly for the ω BW:

$$BW_\omega = \frac{\sqrt{m_{\pi\pi} \cdot m_\omega \cdot \Gamma_\omega(m_{\pi\pi})}}{m^2_{\pi\pi} - m^2_\omega + i m_\omega \cdot \Gamma_\omega(m_{\pi\pi})}, \tag{3.5}$$

where the mass-dependent width $\Gamma_\omega(m_{\pi\pi})$ is given by

$$\Gamma_\omega(m_{\pi\pi}) = Br(\omega \to \pi\pi)\Gamma(m_\omega) \cdot \frac{m_{\pi\pi}}{m_\omega} \cdot \left(\frac{m_{\pi\pi}^2 - 4m_\pi^2}{m_\omega^2 - m_\pi^2}\right)^{3/2}, \tag{3.6}$$

with a branching ratio of ω to pions $Br(\omega \to \pi\pi) = 0.0153$ [62].

3.1.2 Ross and Stodolsky model

Another model was proposed by Ross and Stodolsky (RS) in 1965 [65]. Their work extended the research of Good and Walker on diffraction dissociation [66] in high-energy photoproduction.

The RS model introduced a phenomenological γ-ρ coupling, which simply changes a photon to a ρ with a certain coefficient while not changing the wave function. The calculations show that the invariant mass spectrum shape will look like:

$$\frac{\mathrm{d}^2\sigma}{\mathrm{d}m_{\pi\pi}\mathrm{d}\Omega} = g_{\gamma\rho}^2 \left(\frac{m_\rho^4}{m_{\pi\pi}^4}\right) \frac{\mathrm{d}\sigma}{\mathrm{d}\Omega} \times \frac{1}{\pi} \frac{\Gamma/2}{(m_{\pi\pi} - m_\rho)^2 + \Gamma^2/4}. \tag{3.7}$$

This equation predicts that the ρ mass will be shifted downward by a factor $m_\rho^4/m_{\pi\pi}^4$. This will produce a downward shift of about 10 MeV in the photoproduced ρ compared with the ρ produced in πN collisions. The shape of the ρ peak is also noticeably skewed.

The formula (3.7) is used by ALICE [67] and STAR [64] in the following form:

$$\frac{d\sigma}{dm_{\pi\pi}} = f \cdot |BW|^2 \cdot \left(\frac{m_{\rho^0}}{m_{\pi\pi}}\right)^k, \tag{3.8}$$

where the parameters f and k are determined by the fit and another definition of the mass dependent width can also be used:

$$\Gamma(m_{\pi\pi}) = \Gamma(m_{\rho^0}) \cdot \left(\frac{m_{\pi\pi}^2 - 4m_\pi^2}{m_{\rho^0}^2 - m_\pi^2}\right)^{3/2}. \tag{3.9}$$

3.2 Previous measurements

3.2.1 Measurements at HERA

After the era of fixed target experiments [68, 69, 70, 71, 72, 73], the photoproduction of ρ^0 off protons was studied at the electron-proton collider HERA by the H1 and ZEUS collaborations.

The latest measurement was performed by the H1 collaboration in 2020 [74]. A sample of about 900000 events was used to measure single- and double-differential cross sections for the reaction $\gamma p \to \pi^+\pi^- Y$. The measurements are presented in various bins of the photon-proton collision energy $W_{\gamma p}$. The phase space restrictions are $0.5 < m_{\pi\pi} < 2.2$ GeV, $|t| < 1.5\,\mathrm{GeV}^2$, and $20 < W_{\gamma p} < 80$ GeV. Cross section measurements of elastic ρ^0 photoproduction are presented in Fig. 3.2 together with previous measurements.

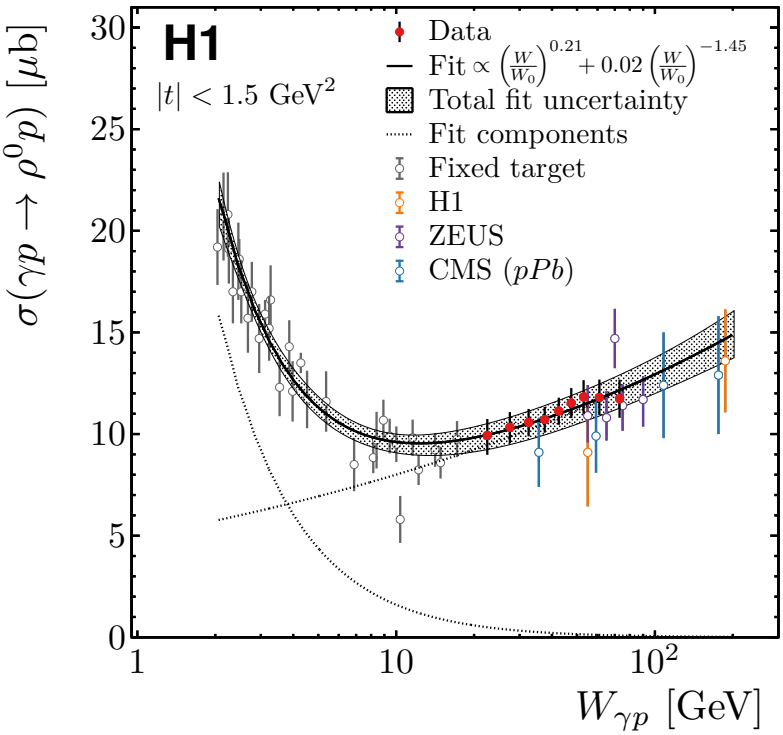

Fig. 3.2: Elastic ρ^0 meson photoproduction cross section as a function of $W_{\gamma p}$. The present data are compared to measurements by fixed-target [68, 69, 70, 71, 72, 73], HERA [75, 76, 77], and LHC [78] experiments as indicated in the legend. Only total uncertainties are shown. The solid line shows the fit of a sum of two power-law functions to the fixed-target and HERA data. The respective contributions are shown as dotted lines. The fit uncertainty is indicated by a band. Taken from [74].

Parametrising the $m_{\pi\pi}$ dependence (Fig. 3.3) with resonant and non-resonant contributions (Söding model in Sec. 3.1.1) added at the amplitude level leads to a measurement of the ρ^0 meson mass and width at $m_\rho = 770.8\ ^{+2.6}_{-2.7}$ (tot.) MeV/c^2 and $\Gamma_\rho = 151.3\ ^{+2.7}_{-3.6}$ (tot.) MeV/c^2, respectively. For the first time at HERA, the sensitivity of the data was sufficient to

constrain the ω meson contribution to $\pi\pi$ photoproduction and measure the ω meson mass at $m_\omega = (777.9 \pm 2.2\ (\text{stat.})\ ^{+4.3}_{-2.2}\ (\text{syst.}))\ \text{MeV}/c^2$.

Older H1 results [75] measured the cross section at two different average photon-proton centre-of-mass energies of 55 and 187 GeV.

Elastic and proton dissociative ρ^0 photoproduction was also measured by the ZEUS collaboration in 1995 [76] and 1997 [77]. Both Söding and Ross-Stodolsky models were used for signal extraction. The differential cross section was obtain at photon-proton centre-of-mass energies in the range $50 < W_{\gamma p} < 100$ GeV and for $|t| < 0.5\ \text{GeV}^2$ as shown in Fig. 3.2.

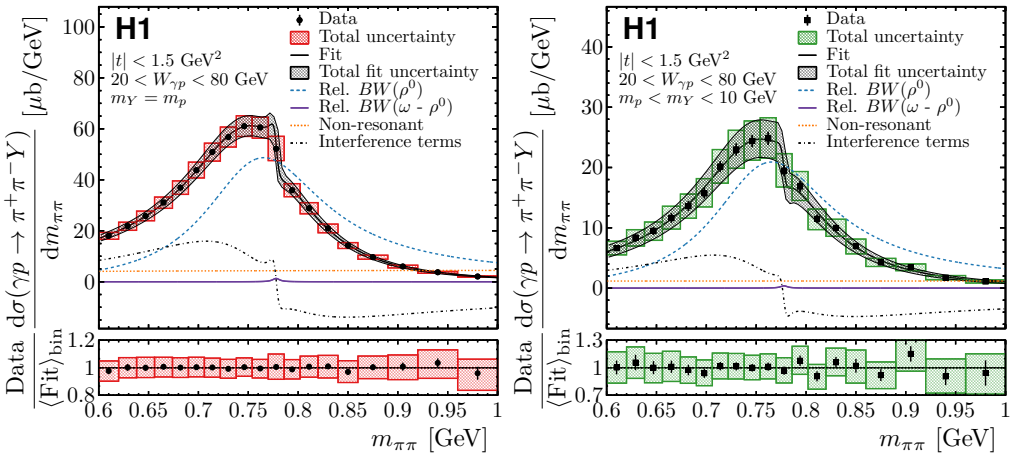

Fig. 3.3: Elastic (left) and proton-dissociative (right) differential $\pi\pi$ photoproduction cross sections as functions of $m_{\pi\pi}$ measured by H1 in 2020. Taken from [74].

3.2.2 Measurements at RHIC

The STAR Collaboration measured the coherent photonuclear production of a ρ^0 vector meson at midrapidity in Au–Au UPCs at the Relativistic Heavy Ion Collider (RHIC) at three different centre-of-mass energies per nucleon pair $\sqrt{s_{\text{NN}}} = 62.4$ GeV [79], $\sqrt{s_{\text{NN}}} = 130$ GeV [80], and $\sqrt{s_{\text{NN}}} = 200$ GeV [81, 64]. The measured cross sections are summarised in Table A.1.

Let's describe STAR results at a centre-of-mass energy of 200 GeV/nucleon-pair [64] in more detail.

That analysis used data collected in 2010 with an integrated luminosity of $(1100 \pm 100)\,\mu b^{-1}$. About 384,000 events with $\pi^+\pi^-$ candidates were used for physics evaluation.

The STARlight Monte Carlo [50] was used for acceptance and efficiency, however, a mix of ρ^0 and non-resonant $\pi^+\pi^-$ events was used, after passing

a GEANT 3 [82] simulation of the detector. Events were embedded in 'zero-bias' STAR events providing a good agreement with the detector noise and backgrounds.

The STAR analysis considered two types of nuclear breakup: single neutron (1n) and more than one neutron (Xn). The cross section for coherent ρ^0 photoproduction accompanied by different numbers of neutrons was determined.

The invariant mass spectrum of pion pairs with $p_T < 100\,\mathrm{MeV}/c$ corrected by the acceptance and efficiency is shown in Fig. 3.4. The spectrum was fitted using an improved Söding model, where an additional relativistic Breit-Wigner component was added to account for ω photoproduction. As can be seen from the Fig. 3.4, the ω cross section is low, however, it can be seen through the ρ^0-ω interference term causing a 'kink' in the spectrum. This is the first observation of the ω photoproduction in ultra-peripheral collisions and the first measurement of the ρ^0-ω interference [83] at RHIC energies. The masses and widths of the ρ^0 and ω were compatible with PDG values.

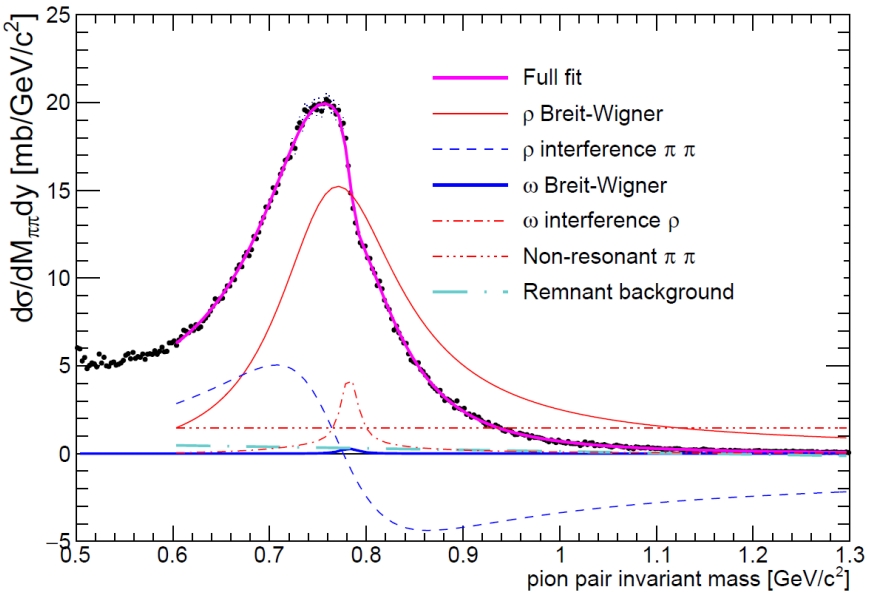

Fig. 3.4: Fitted invariant mass spectrum from the STAR experiment. Taken from [64].

The STAR Collaboration measured the rapidity dependence of the ρ^0 cross section $\mathrm{d}\sigma/\mathrm{d}y$ as shown in Fig. 3.5. There is a large improvement in statistical errors compared to the previous measurement in 2008 [81]. The dependence is compatible with the STARlight prediction within the systematic errors.

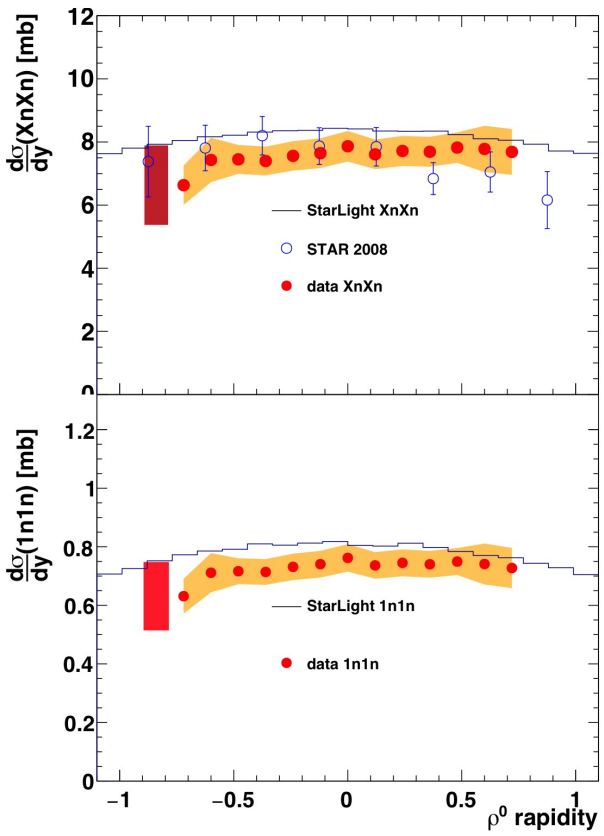

Fig. 3.5: $\mathrm{d}\sigma/\mathrm{d}t$ dependence for different neutron scenarios compared with the STARlight model. Taken from [64].

The large size of the STAR data sample allows for the measurement of the differential cross section $\mathrm{d}\sigma/\mathrm{d}t$ showing a clear diffraction pattern. The Fourier transform of this distribution describes the average distribution of QCD matter in the transverse plane of the target nucleus.

The STAR collaboration explored higher mass final states, and observed a $\pi^+\pi^-$ state with a mass of (1653 ± 10) MeV/c^2 and a width of (164 ± 15) MeV/c^2 (statistical errors only) as can be seen in Fig. 3.6. The state is at least roughly compatible with the $\rho_3(1690)$ [84].

The STAR collaboration has also measured the interference between ρ^0 production from two sources (the two nuclei) by observing the $\pi^+\pi^-$ decay products. The interference was observed at $(87 \pm 5(\text{stat.}) \pm 8\ (\text{syst.}))\%$ of the expected level. This shows that the final state wave function retains

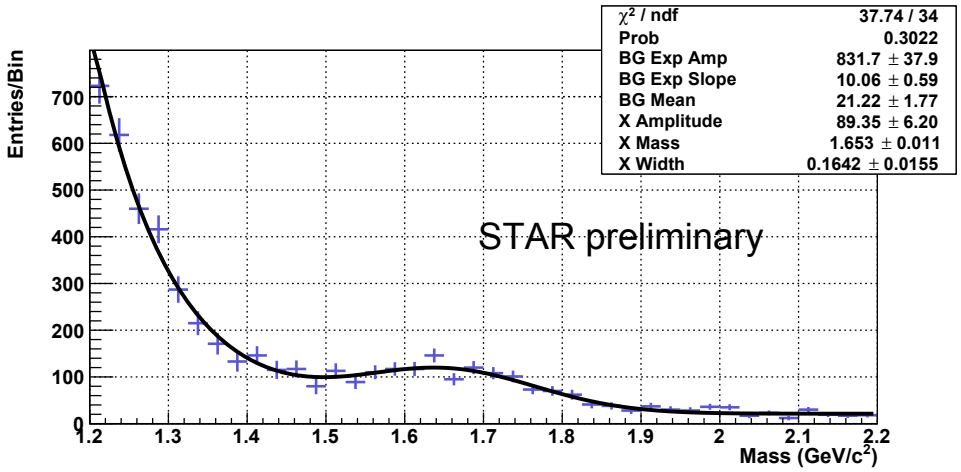

Fig. 3.6: STAR preliminary dipion mass spectrum for pairs with $M_{\pi\pi} > 1.2$ GeV, along with a fit to an exponential tail of the ρ^0, a constant background, and a Gaussian peak. Errors are statistical only. Taken from [84].

amplitudes for all possible decays, long after the decay occurs. The maximum decoherence (loss of interference) is less than 23% at the 90% confidence level [85].

3.2.3 Measurements at the LHC

The coherent photoproduction of a ρ^0 meson was measured at the LHC by the ALICE Collaboration. It was studied in ultra-peripheral Pb–Pb collisions at $\sqrt{s_{NN}}$ =2.76 TeV [67].

The analysis used data collected during the 2010 Pb–Pb run. Two different triggers were used: at the beginning of the run the trigger was based on the Time-Of-Flight (TOF) detector, at the end, when luminosity was high, an additional requirement for at least two hits in the outer layer of the SPD and a veto in the V0 arrays were used.

The ρ^0 was measured using its decay into a $\pi + \pi^-$ pair. The pions were detected in the central barrel (midrapidity) using the ITS and TPC for tracking and particle identification, TOF and V0 for triggering, and ZDC for detection of forward neutrons.

The measured pion-pair p_T is shown in Fig. 3.7. A clear coherent peak can be seen and it is compared to a STARlight simulation. The data are shifted to lower p_T as compared to predictions, which was also observed by STAR. The reason is that the STARlight program does not include all known effects. Data also show a dip around $p_T = 0.12$ GeV/c, which is not present in

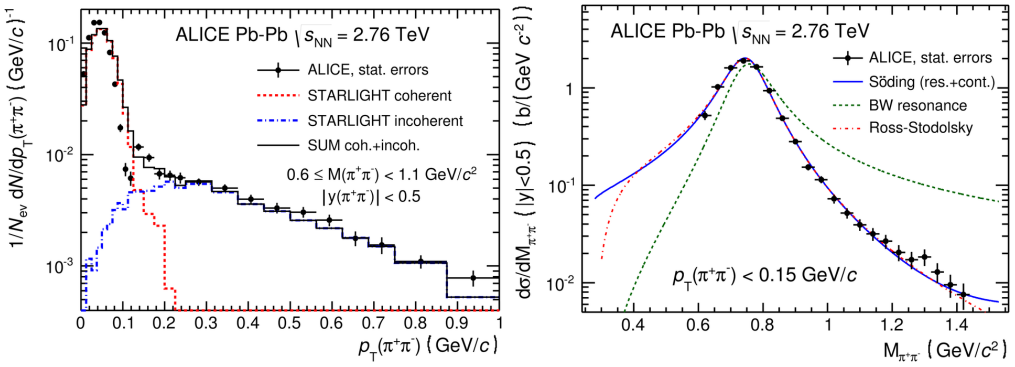

Fig. 3.7: Left: Measured pair-p_T distribution compared to the STARlight model. Right: Invariant mass distribution corrected for the acceptance and efficiency fitted with the Söding and Ross-Stodolsky functions. Taken from [67].

the STARlight model (new predictions for the p_T spectrum are in [86]). The high-p_T tail coming from the incoherent production of ρ^0 is well described by STARlight.

The invariant mass distribution (Fig. 3.7 right) corrected for the acceptance and efficiency was fitted using a Söding parametrisation [63], and a Ross-Stodolsky function [65] was used as a cross-check. The mass and width of ρ^0 were in a good agreement with PDG values, the ratio of the non-resonant and resonant amplitudes was significantly lower compared to the STAR measurement. It may indicate that the non-resonant production is absorbed in Pb nuclei at higher energies.

The coherent ρ^0 cross section can be seen in Fig. 3.8 where it is compared to the STARlight model, calculations by Goncalves and Machado (GM) [57], and the Glauber-Donnachie-Landshoff (GDL) model [87]. The measured cross section is in agreement with the first and second of the previously mentioned models, but GDL is a factor 2 higher.

The STAR Collaboration measured the total coherent cross section at different energies. To compare these results, the measured cross section was integrated over the full phase space using models and it can be seen as a function of the centre-of-mass energy $\sqrt{s_{NN}}$ in Fig. 3.8. The total cross section increases by a factor of 5 between RHIC and LHC energies. GDL overpredicts the cross section by a factor of two, independent of energy, indicating that the process is not fully understood.

The fraction of events in classes separated according to forward neutron activity was reported. The results were found to be compatible with both STARlight and GDL models within 3σ.

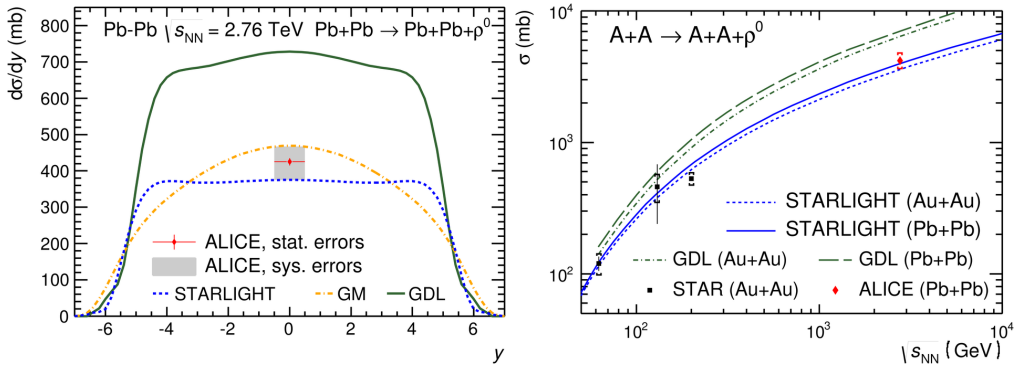

Fig. 3.8: Left: Differential cross section $d\sigma/dy$ for coherent ρ^0 measured by ALICE and compared to models. Right: The total cross section for coherent ρ^0 in Pb–Pb and Au–Au systems compared to STARlight and GDL predictions. Taken from [67].

For completeness, let me mention that the exclusive ρ^0 photoproduction was measured for the first time in ultra-peripheral pPb collisions at $\sqrt{s_{\mathrm{NN}}} = 5.02$ TeV with the CMS detector [78]. The cross section $\sigma(\gamma\ \mathrm{p} \to \rho^0\ \mathrm{p})$ was found to be $(11.0 \pm 1.4(\mathrm{stat.}) \pm 1.0(\mathrm{syst.}))\,\mu\mathrm{b}$ at $\langle W_{\gamma p} \rangle = 92.6$ GeV for photon-proton centre-of-mass energies $W_{\gamma p}$ between 29 and 213 GeV. The differential cross section $\mathrm{d}\sigma/\mathrm{d}|t|$ was measured in the interval $0.025 < |t| < 1$ GeV^2 as a function of $W_{\gamma p}$. The $W_{\gamma p}$ dependence of the exponential slope of the differential cross section $\mathrm{d}\sigma/\mathrm{d}|t|$ was also measured.

Chapter 4

Results on coherent ρ^0 photoproduction at the LHC Run 2 energies

4.1 Motivation for new ρ^0 measurements

Nowadays, the LHC is the most powerful source of photon collisions [34]. The ultra-peripheral processes, in particular photoproduction of vector mesons, offer a unique opportunity to study fundamental interactions in QED and QCD.

The main motivation to measure the coherent ρ^0 photoproduction is that it is a clean probe of the hadronic structure and allows for a direct determination of the gluon distribution inside nucleons and nuclei [88]. The gluon distribution cannot be directly estimated using deep-inelastic scattering, because gluons do not have an electrical or weak charge. Interesting is the measurement of nuclear shadowing [89] using heavy-ion beams where the LHC offers the highest γ-Pb energy $W_{\gamma\mathrm{Pb}}$ ever, corresponding to small x through the relation $x = (M_{\mathrm{VM}}/W_{\gamma\mathrm{Pb}})^2$.

The coherent ρ^0 photoproduction process in heavy-ion UPCs is an excellent tool to test the black disc regime, where the target nucleus appears as a black disc and the total ρ^0+A cross section reaches its limit. RHIC and first LHC results have deviated from some Glauber+VDM calculations, which is thus a call for new data.

In addition, the measurement of the coherent photoproduction of ρ^0 mesons for different classes on forward neutron activity offers the possibility to extract the energy dependence of the cross section as proposed in [39] and computed for current ALICE parameters by Guzey, Kryshen and Zhalov [52].

The basic idea is that the presence of forward neutrons modifies the impact-parameter range sampled by the process, so using Eq. (2.7) for each class and knowing the photon-flux, one can solve it for the two photonuclear cross sections. The measurement at $y = 0$ will allow us to test the method accuracy using the symmetry of Eq. (2.7) and then using the forward neutron classes.

Furthermore, the coherent production of a ρ^0 vector meson off a nucleus allows for the study of shadowing. This phenomenon is expected to depend on the atomic number A of the nucleus so measurements for different values of A offer another tool to test our understanding of shadowing at high energies and at semi-hard scales. Nowadays, the LHC offers Pb–Pb and Xe–Xe collisions that can be used to study this dependence.

Moreover, the measurement of coherent photoproduction in UPCs at the LHC can be used to gain information on the nuclear matter distribution as was shown by STAR [64]. This can be particularly interesting for Xe–Xe collisions, because the nuclear matter distribution, the effective nuclear radius, and the structure factors of Xe isotopes are of key importance for experiments searching for dark matter with Xenon-based detectors [53].

4.2 Coherent ρ^0 measurement in Pb–Pb UPCs

This section presents my work on ALICE results that lead to publication of the paper "Coherent photoproduction of ρ^0 vector mesons in ultra-peripheral Pb–Pb collisions at $\sqrt{s_{\rm NN}}$ = 5.02 TeV" [90]. The preliminary results were shown at the Quark Matter 2017 conference in the form of a poster that can be seen in Appendix B.6. The final results were also presented in the form of a poster (Appendix B.7) at the LHCP 2020 conference and which won one of the 'Poster Awards'.

4.2.1 Data and Monte Carlo

The analysed data were recorded by ALICE towards the end of 2015, when the LHC provided Pb–Pb collisions at $\sqrt{s_{\rm NN}} = 5.02$ TeV. The corresponding period is LHC15o containing several filling schemes:

- 2 colliding bunches, runs 244824-244827
- 6 colliding bunches, runs 244917-244918
- 18 colliding bunches, runs 244975-245068
- 236 colliding bunches, runs 245145-245256

- 362 colliding bunches, runs 245345-246994

that are usually split into low interaction rate (IR) and high IR.

We followed the Data Preparation Group (DPG) recommendation and we used pass5 processing for low IR data and pass1 for high IR data, however during the analysis, we cross-checked the results with dedicated UPC-processing pass2_CCUP of high IR data.

In total, 83 runs were selected, recommended by the DPG containing the CCUP9 trigger and full TPC coverage.

For low IR data a 'pass5' reconstruction was used: 244975, 244980, 244982, 244983, 245064, 245066, 245068.

For high IR data 'pass1' reconstruction was used: 245683, 245692, 245702, 245705, 245829, 245831, 245833, 245923, 245949, 245952, 245954, 245963, 246001, 246003, 246012, 246036, 246037, 246042, 246048, 246049, 246052, 246053, 246087, 246089, 246113, 246115, 246148, 246151, 246152, 246153, 246178, 246180, 246181, 246182, 246185, 246217, 246222, 246225, 246271, 246272, 246275, 246276, 246424, 246431, 246434, 246487, 246488, 246493, 246495, 246750, 246751, 246757, 246758, 246759, 246760, 246763, 246765, 246766, 246804, 246805, 246807, 246808, 246809, 246810, 246844, 246845, 246846, 246847, 246851, 246945, 246948, 246982, 246984, 246989, 246991, 246994.

All data were processed on ESD level because of one specific selection criterion that was introduced in this analysis (to be explained later) and because the processed AOD files do not contain the necessary information. Both data and MC samples are preselected on the ALICE GRID using the AliAnalysisTaskUpcRho0.cxx code running in the LEGO train[1]. Namely, trains 168, 160, 161, and 162 were used for final results. This class is responsible for selecting triggered events with two good-quality tracks and calculating the ρ^0 kinematic variables. Its output is only several hundreds of Megabytes in the TTree format allowing for the further processing locally and a fast changing of other selection criteria such as kinematics or binning.

4.2.2 UPC trigger

The main trigger used for this analysis is CCUP9, however several other triggers were used for corrections and systematic studies as will be explained later. The full list of triggers and trigger elements can be found in Appendix B.1. Now let us describe the CCUP9 that consists of four veto decisions from V0 and AD scintillator detectors, ensuring that there are no charged particles in the forward and backward pseudorapidities, and the

[1]The code is accessible to ALICE users in the git directory of the PAG-UPC.

0STP trigger element that ensures activity in the central barrel as only two pions are expected in the central barrel during the coherent ρ^0 photoproduction. The 0STP element is a crucial one as without that, most of the accepted events would be empty.

The online trigger decision provided by the V0 is a binary (fired / not fired) trigger input on each side (0VBA and 0VBC). Each requires that there is at least one V0 cell fired in the beam–beam (BB) time window. The offline trigger decision is much more complex – the signal is processed, corrected, and its signal threshold can be adjusted. Its final output is an integer number:

- ▷ 0 (kEmpty) → the detector is empty.
- ▷ 1 (kBB) → the detector has a signal in the beam–beam time window.
- ▷ 2 (kBG) → the detector has a signal in the beam–gas time window.
- ▷ 3 (kFake) → the signal in the detector arrived at a time outside both the beam–beam and the beam–gas windows.

The situation is quite similar for the AD detector. The online and offline outputs are the same, however during the processing of the offline decision, a correction on trigger time slewing is made. That is because the charge collected by the AD detector is estimated using a threshold discriminator and therefore, the trigger time is shifted and depends on the charge in the detector as shown in Fig. 4.1.

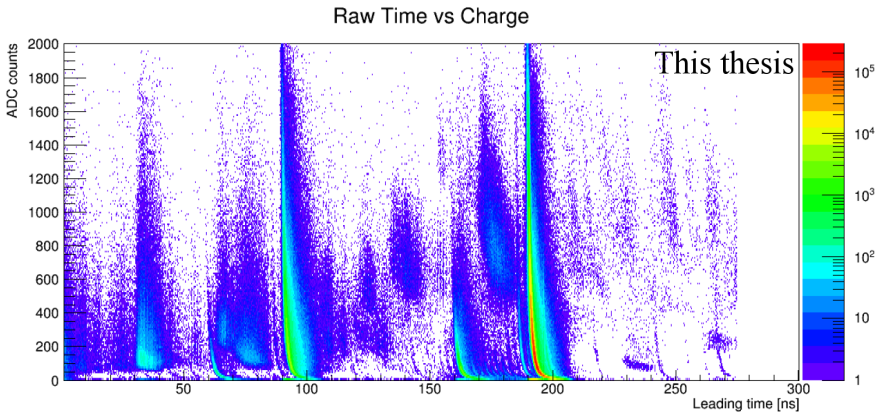

Fig. 4.1: Example of time-slewing in the AD detector due to use of threshold discriminator.

There are several possible configurations of the trigger in the inner pixel detector SPD. We will describe it in more detail as one of the main analysis corrections is done for this trigger.

The 0STP component of the trigger requires presence of (at least) two hits in the inner layer of SPD and another two in the outer one, which have a back-to-back topology in the transverse plane. In other words, there are 240 modules that provide a fast-OR signal and at least four of the 240 ladders have to form a back-to-back topology (Fig. 1.7). The result of that is that only events with a low pair-p_T up to 200–300 MeV/c can be accepted with full efficiency and therefore, the trigger has a great acceptance for coherent production of vector mesons in UPCs and removes events with no activity in barrel detectors or at higher p_T.

There are several pitfalls of the 0STP trigger. Firstly, the efficiency of each fast-OR module has to be estimated and well reproduced in the Monte Carlo. Secondly and more importantly, the trigger logic works only in the transverse plane. So, for example, if one of the fired modules is on one side of the SPD along z-axis and the other in the second layer on the other side along z-axis, the trigger can be fired even though they are not from a single track. This can lead to a very uncomfortable situation: the coherent ρ^0 photoproduction is often accompanied by photoproduction of very soft electron-positron pairs that will reach just the SPD and they can produce a fast-OR signal in several modules. In such case, the 0STP trigger logic could be fulfilled although pions from coherent ρ^0 production did not fired the trigger (e.g. if they passed a dead module). This effect is expected to be up to 10% at $\sqrt{s_{\mathrm{NN}}} = 5.02$ TeV as the production cross section is high and therefore, we will describe its correction in Sec. 4.2.4 as this was one of the important findings of this work and results in an improvement with respect to the other UPC analyses.

4.2.3 Event selection

The tracks used for the analysis (good-quality tracks), were required to:

- have distance-of-closest approach (DCA) to the event primary vertex below $0.0182 + 0.035/{p_T}^{1.01}$ and 2 cm in the transverse plane and in the longitudinal direction, respectively;
- be a TPC-global track refitted in both TPC and ITS;
- have more than 50 TPC clusters;
- have 2 SPD clusters matched to the track. This criterion is motivated by the trigger condition, as discussed below, and it allows to discard most of out-of-BC time ghost tracks as well.

The selected events were required to fulfill:

- triggered by the CCUP9 trigger
- exactly two reconstructed good-quality tracks.
- opposite charge of two tracks (like-sign events were used for the estimation of combinatorial background)
- offline V0 veto (V0A and V0C decision empty)
- offline AD veto (ADA and ADC decision empty)
- n_σ(pion) from TPC PID of both particles limited by $n_{\sigma_1}^2 + n_{\sigma_2}^2 < 5^2$. The criterion effectively removes electron-positron pairs and other contamination from kaons and protons.
- fast-OR fired SPD chips matched to the reconstructed tracks as explained below.

Kinematic selection of the ρ^0 candidate:

- To have an absolute value of the pair rapidity below 0.8 to cut-away the edges of the detector where efficiency can be difficult to estimate. Where it is not mentioned explicitly, a pion mass is assumed.
- Invariant mass (under the pion hypothesis) higher than 550 MeV/c^2. The cut on n_σ(pion) does not remove low mass di-electrons due to overlapping dE/dx curves of pions and electrons below this value.
- Invariant mass (under the pion hypothesis) below 1400 MeV/c^2.
- Pair-p_T below 200 MeV/c to have a coherent-enriched sample.

The final number of selected events is 56 699 and the number of events after each selection criterion is applied can be seen in Appendix B.2.

4.2.4 Data quality

In this section, we present information to study the characteristics of the selected data. The starting point is the data after the preselection. Distributions of variables either used in the selection process or of importance to the analysis are shown and their impact on the analysis procedure is discussed. When possible, they are compared with equivalent distributions from the MC samples.

Track variables We already said that only events with exactly two good-quality tracks are used in this analysis. The reason is that we want to compute kinematics of the initial states and reduce the combinatorial background. The trigger itself is also taking data with higher number of tracks and from the physics point of view, the coherent ρ^0 can be accompanied by other soft particles that can be reconstructed in the TPC, however, we will deal with that later on in the pile-up section.

The "good-quality track" selection follows the standard ALICE track selection on AOD level based on filter bits. The number of clusters in TPC has to be at least 50 in order to have a good reconstructed and fitted track.

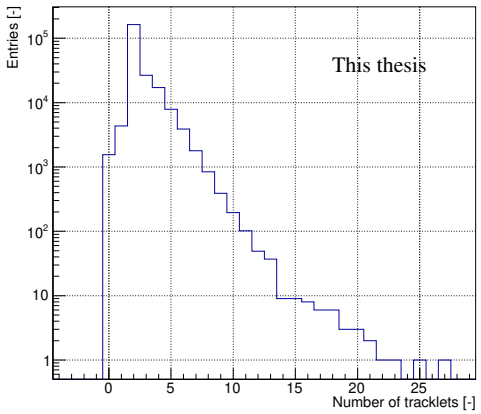

Fig. 4.2: Number of tracklets in Pb–Pb data with track selection only.

The number of tracklets (connected clusters in the SPD) can be seen in Fig. 4.2. The expected number of tracklets is two, as indicated by the Monte Carlo, however in some events, three clusters can be produced due to chip overlapping causing double hits in one layer of SPD. In the data the number of tracklets is higher and even events with up to twenty tracklets are seen. This is a strong indication that particles with very low p_T, mainly from the QED production of electron–positron pairs, are present in the data sample. In the previous ρ^0 analysis at ALICE, the cut on the number of tracklets was used and the cross section was then corrected on the probability (pile-up) that an additional tracklet will be present on top of the coherent ρ^0. However, we think that keeping events with additional tracklets is beneficial to obtain the best amount of data and we ensured that our trigger is not misfired by these soft tracks by adding the procedure described below.

Figure 4.3 shows the correlation between the pseudorapidity of both tracks (η) for data and STARlight MC. A similar pattern is found in both cases suggesting a well simulated behaviour.

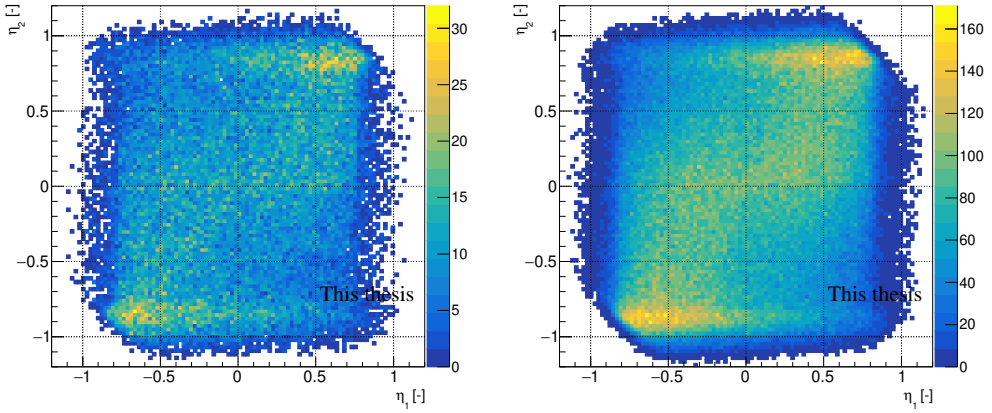

Fig. 4.3: Correlation between the pseudorapidity of both tracks η_1-η_2 after event selection. Left: data, right: STARlight MC.

Vertex Figure 4.4 shows the distribution of the z coordinate of the primary vertex compared to MC. As can be seen the vertex distribution is very well described in MC and stay in the safe ± 15 cm region. The difference found between the primary and the SPD vertices (a vertex that is reconstructed using only SPD clusters) in data and MC are shown in Fig. 4.5.

AD and V0 veto decisions The V0 and AD scintillator detectors are used as veto detectors in the trigger. Moreover, both detectors can also be used in the offline mode, when a more precise signal processing is done. Both online and offline decisions can be used to veto, but in each case the pile-up probability (that an additional particle will hit the detector) needs to be estimated for each individual detector array.

The offline decision of the AD is shown in Fig. 4.6. As can be seen, most of the events are considered to be empty and only a small number of events (2%) is denoted as fake signals. These are neither in beam-beam (BB) nor in beam-gas (BG) time and they may come from cosmic rays or from neighbouring bunches.

The offline decision of the V0 array is in Fig. 4.7. As can be seen, the number of BB and BG hits in the offline V0 is quite common compared to the AD.

Particle identification The aim of the particle identification (PID) is to have well identified pion candidates in most of the events and to reduce other type of particles (background) to a minimum. The PID is estimated using the information from the TPC, specifically the TPC signal in arbitrary

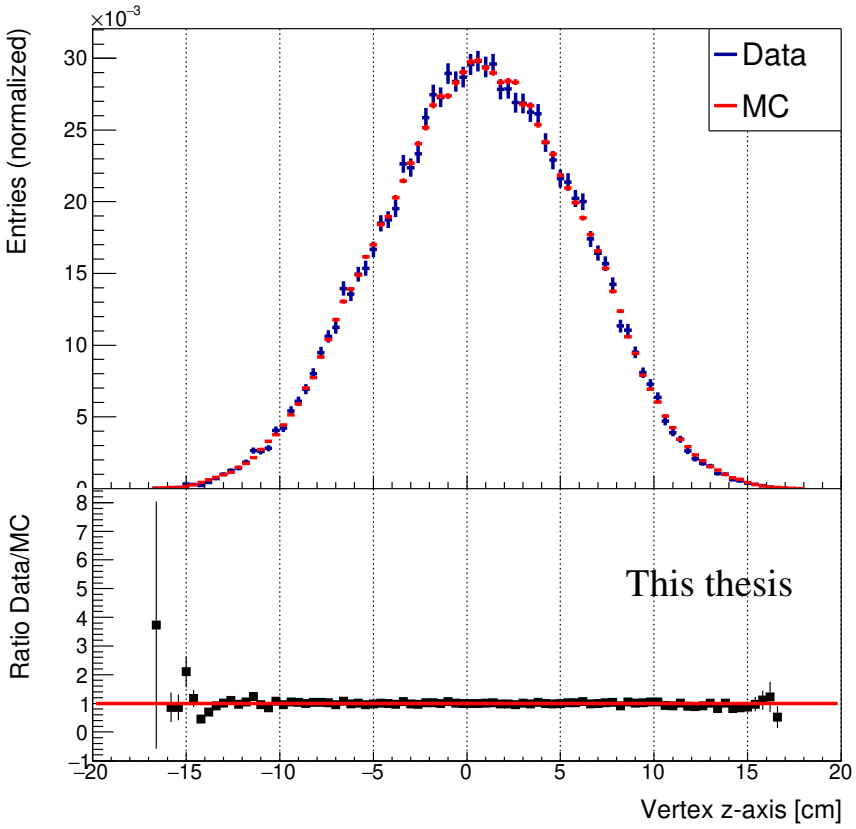

Fig. 4.4: Vertex distribution in the z-axis for Data and STARlight MC.

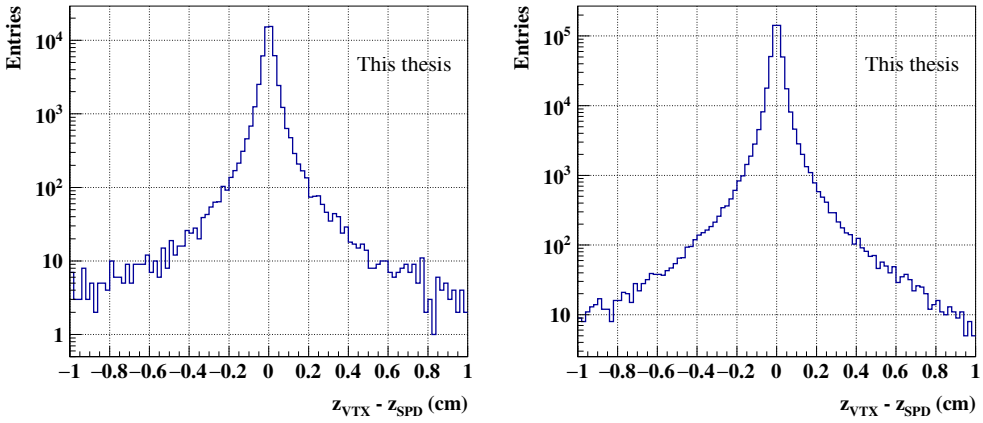

Fig. 4.5: Left: Distance between the primary vertex and the SPD vertex in data. Right: Same, but for the coherent MC.

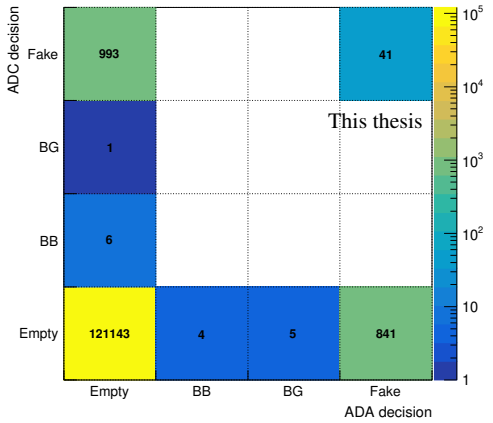

Fig. 4.6: Decision of the ADA and ADC detector.Figure obtained using only track, run and trigger selection.

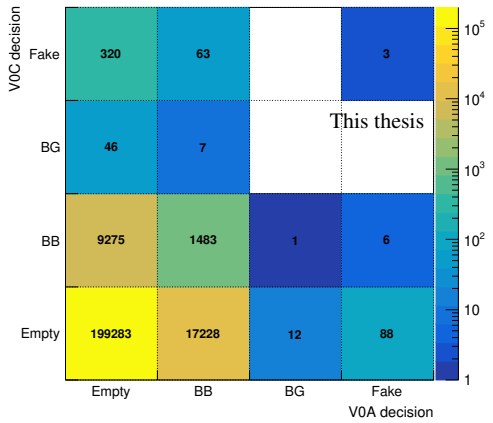

Fig. 4.7: Decision of the V0A and V0C detector. Figure obtained using only track, run and trigger selection.

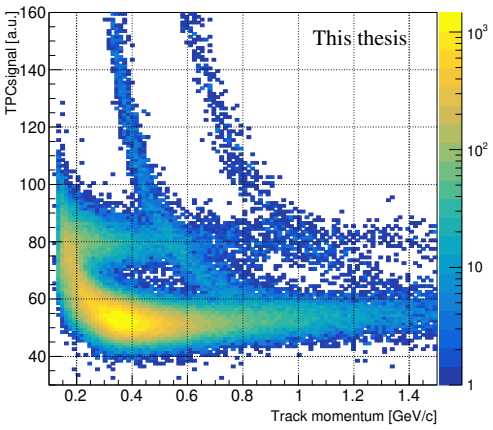

Fig. 4.8: Signal in TPC versus track momentum. Figure obtained using only track, run and trigger selection.

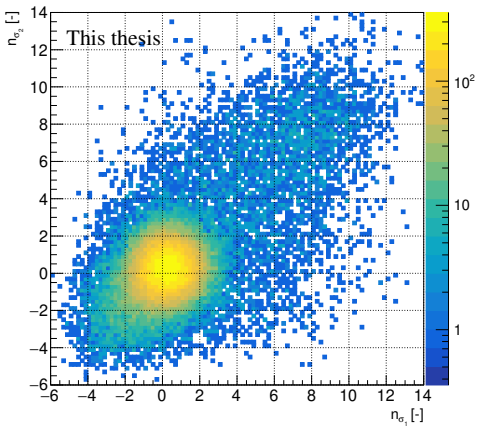

Fig. 4.9: n_σ of tracks. Figure obtained using only track, run and trigger selection.

units. The usually shown graph of TPC signal versus the track momentum of our data can be seen in Fig. 4.8. Contamination from electrons, kaons, and protons is visible.

The PID is based on the n_σ hypothesis. It is obtained from the general ALICE class AliPIDResponse.h that provides n_σ for each track under different particle hypothesis (pion, muon, electron, kaon,...). The two-dimensional

plot of both tracks using the n_σ pion hypothesis is shown in Fig. 4.9.

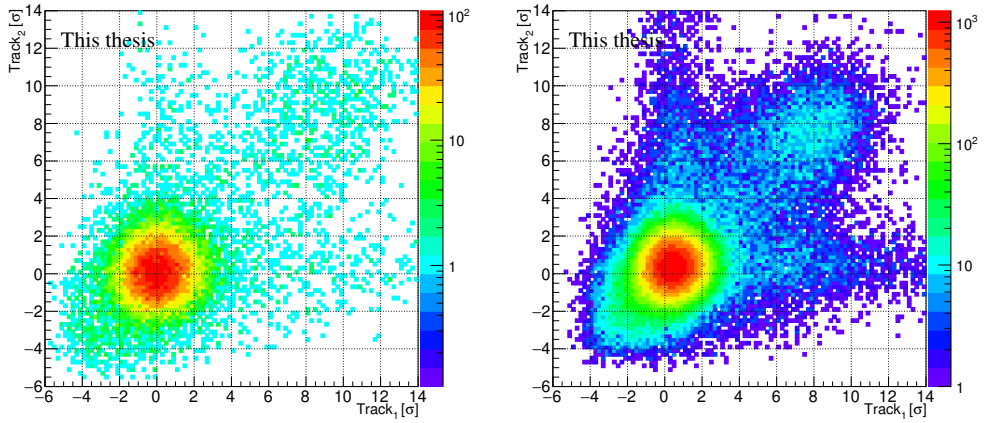

Fig. 4.10: n_σ of tracks in the low IR (left) and high IR (right) data sample. Notice the shift of the centre from (0,0) in the high IR samples.

The n_σ distribution in the high IR data sample is slightly shifted compared to the low IR sample, and its centre is not at the (0,0) point as can be seen in Fig. 4.10. The reason is the presence of large TPC distortions in LHC15o for high intensity runs. These distortions are corrected in ALICE data, however the correction is not optimised for low multiplicity data as UPCs. This effect is not properly described in MC, therefore, we decided to use a circle cut of a radius of 5 ($n_{\sigma_1}^2 + n_{\sigma_2}^2 < 5^2$) instead of the usual radius of $3n_\sigma$ to keep all possible pions and to avoid improperly discarded events.

From Fig. 4.8, it is obvious that our PID is not able to distinguish pions from electrons at very low track momentum. Using the pion and electron hypothesis cuts, we found that we are not able to distinguish pairs of electrons from pairs of pions for invariant masses of the pair below 0.55 GeV/c^2. This effect is shown in Fig. 4.11 and it is the motivation to include a lower mass cut at 0.55 GeV/c^2.

Since we are not able to distinguish muons from pions in the TPC, we will have to take them into account later during the signal extraction procedure.

SPD trigger-track matching We already mentioned that our 0STP trigger element in SPD can be fulfilled due to the presence of additional soft tracks. That would cause an overestimation of the number of events and also of the final cross section as this effect is not present in our MC simulations. We decided that this problem can be solved by ensuring that fast-OR signals of the trigger come from modules that can be related to the reconstructed tracks. We call it trigger-track matching procedure.

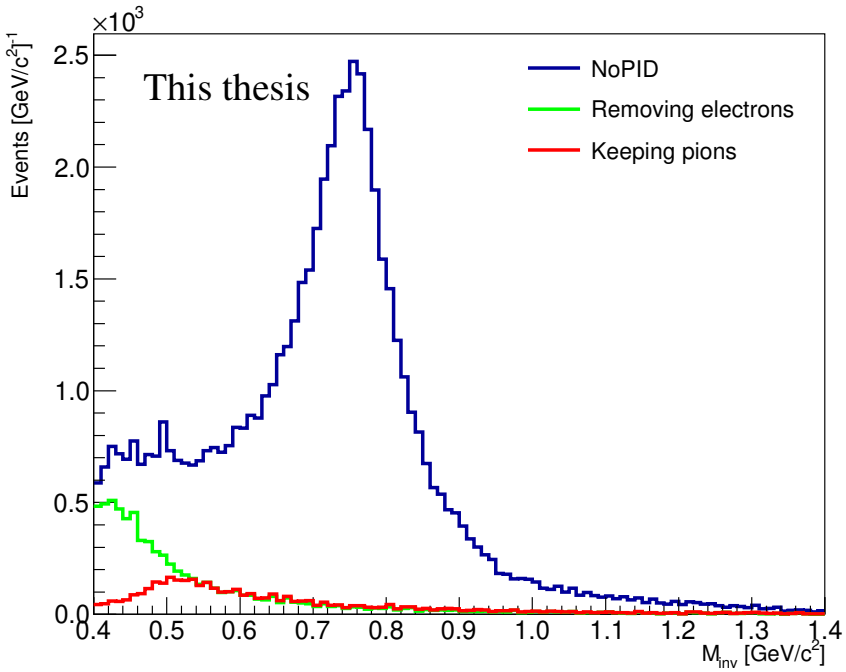

Fig. 4.11: Raw mass spectrum and comparison of PID of pions and electrons. Electrons cannot be identified from pions below 0.55 GeV.

The information of fired fast-OR chips is present in ESD files per chip and can be found for each of the 240 modules as:

```
Int_t fFOmodules[240];
for (Int_t i=0;i<240;i++) fFOmodules[i] = 0;
for(Int_t chipkey=0;chipkey<1200;chipkey++){
  if (esd->GetMultiplicity()->TestFastOrFiredChips(chipkey)){
    fFOmodules[(chipkey/5)]++;
  }
}
```

Now we know which modules provide the trigger signal. Then the index number of modules for each reconstructed track is found for both inner and outer module:

```
ITSModuleInner_T[i] = trk->GetITSModuleIndex(0)/1000000;
ITSModuleOuter_T[i] = trk->GetITSModuleIndex(1)/1000000;
```

so we get a set of four indexes and we can test if any of the corresponding modules has zero trigger inputs, in such case the track did not fire fast-OR signal and we will exclude such event.

However, one last detail remains, these four matched modules have to satisfy the 0STP trigger condition (that they are in a back-to-back topology). For completeness, the checking code is shown in Appendix B.3.

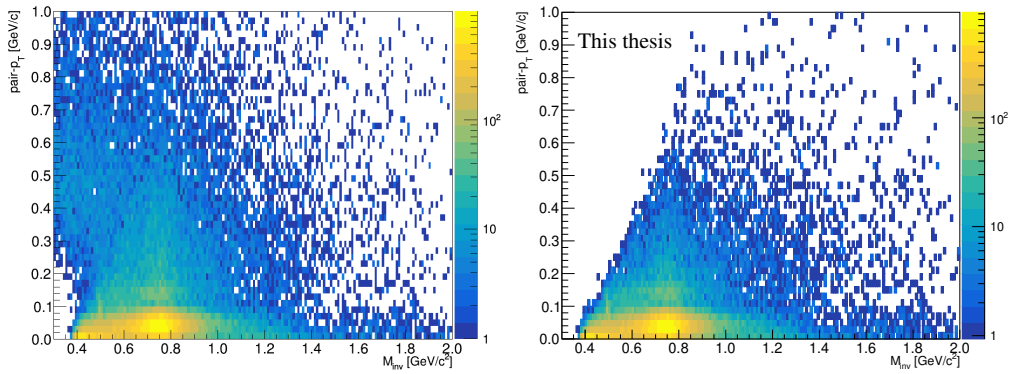

Fig. 4.12: Effect of the chip matching procedure on invariant mass versus transverse momentum distributions of selected events. Left: without the matching procedure, right: after matching. A significant reduction of the background is visible.

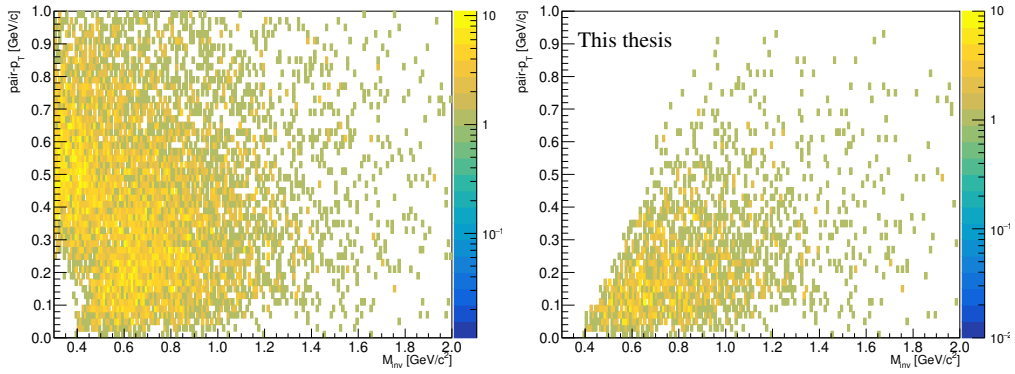

Fig. 4.13: Effect of the chip matching procedure on invariant mass versus transverse momentum distributions of like-sign events. Left: without matching procedure, right: after matching. A significant reduction of LS background is visible.

This procedure is used in both data and Monte Carlo samples and now its effect will be shown. The first effect (denoted as "chipkey cut") can be seen in Fig. 4.12, where events at low invariant mass are completely removed; these events have a larger transverse momentum in average than good events. That is the result of the back-to-back topology condition: these events are

not kinematically allowed and were misfired by an additional track. This effect is also observed in like-sign events in Fig. 4.13.

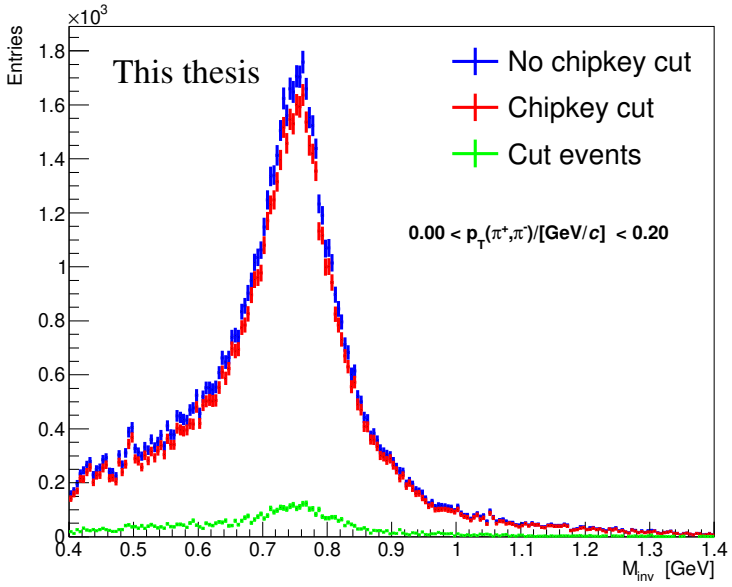

Fig. 4.14: Effect of the trigger-track matching procedure on the invariant mass spectrum. Blue: without the trigger-track matching cut, red: after applying the cut, green: portion of events that are removed.

Moreover, some events are removed although they are kinematically allowed. It can be seen in the invariant mass spectrum in Fig. 4.14. Some of the coherent ρ^0 candidates are removed as suggested also in Fig. 4.15. That is expected: these events are misfired by the trigger and such effect is negligible in MC samples. The main effect is shown in the pair-p_T tail in Fig. 4.15.

Angular distribution of candidates In Fig. 4.16, the angular distribution of pion candidates is shown. As can be seen, there is a small dip in one direction that is caused by dead modules in the ITS detector and this effect is very well reproduced in the STARlight Monte Carlo sample.

Rapidity of candidates The rapidity distribution of pion candidates in data can be seen in Fig. 4.17 and in Fig. 4.18 for the coherent ρ^0 STARlight MC. As can be seen, the detector capability to reconstruct coherent ρ^0 is up to $|y| \approx 1$. However, at the TPC edges the amount of data is very limited and also the number of simulated events in STARlight is quite poor. Therefore, we decided to use only data up to $|y| = 0.8$ to avoid large statistical and systematical uncertainties.

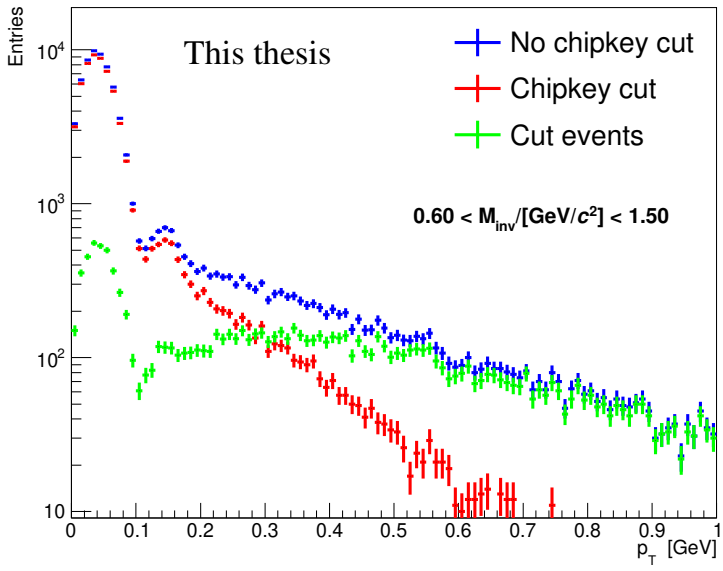

Fig. 4.15: Effect of the trigger-track matching procedure on the transverse momentum spectrum. Note the large reduction of the background tail. Blue: without the trigger-track matching cut, red: after applying the cut, green: portion of events that are removed.

The final sample was split into three rapidity bin subsamples with a similar amount of data. Because the measured cross section is expected to be symmetrical along the rapidity, we can merge the positive and negative rapidity bins together to increase the amount of data in each fitting bin. The symmetry was checked beforehand resulting in positive and negative rapidity bin compatibility. The chosen rapidity bins for the final analysis are $|y| \leq 0.2$, $0.2 \leq |y| \leq 0.45$, and $0.45 \leq |y| \leq 0.8$.

Transverse momentum The raw pair-p_T spectrum of dipion candidates can be seen in Fig. 4.19. As it is shown, there is a significant coherent peak below 0.12 GeV/c followed by a second diffractive peak at around 0.15 GeV/c. The long tail is partially explained by the like-sign contamination. The remaining portion of events in the mid-region is from incoherent ρ^0 production. The dimuon production occupies the very low p_T region up to 0.08 GeV/c. Based on the spectrum shape, we decided to apply a cut on transverse momentum at 0.2 GeV/c to keep the maximum number of coherent candidates and to remove the background tail. The contribution of incoherent ρ^0 to the region of small momentum below this cut will be estimated in the next section using a MC template fit. The contribution

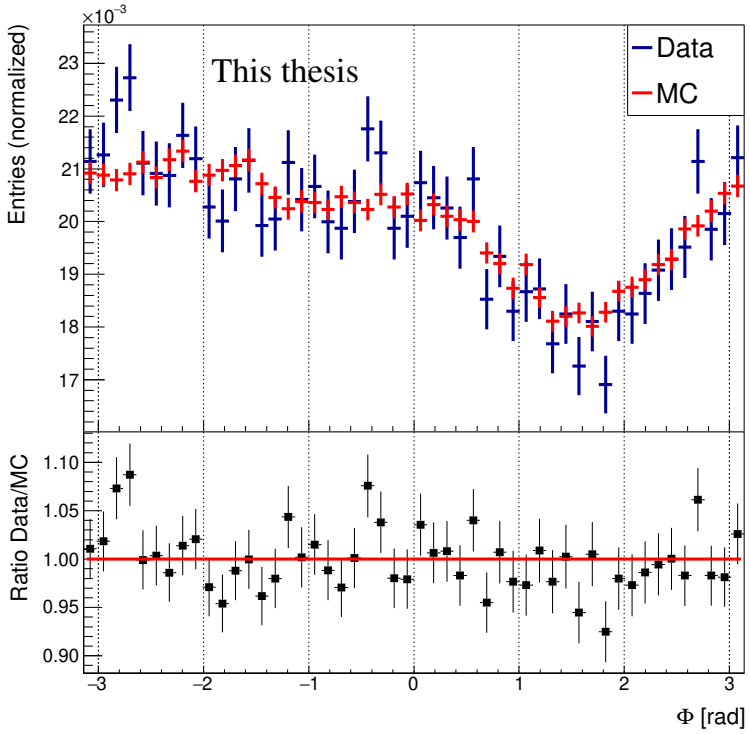

Fig. 4.16: Angular angle ϕ distribution of candidates in the data sample compared to the STARLight MC.

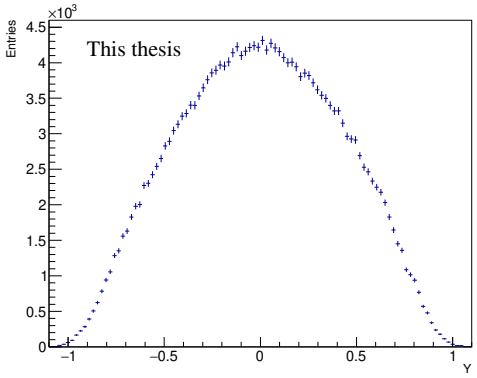

Fig. 4.17: Rapidity y distribution of pion candidates in data. Figure obtained using only the track, run, and trigger selection.

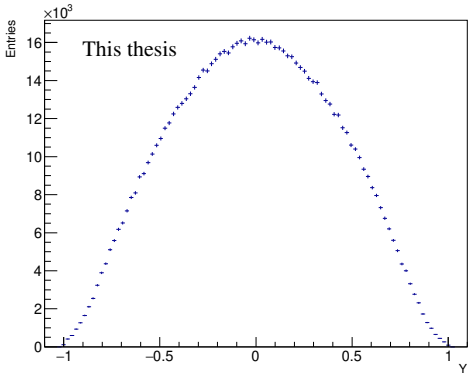

Fig. 4.18: Rapidity y distribution of pion candidates in STARlight MC. Figure obtained using only the track, run, and trigger selection.

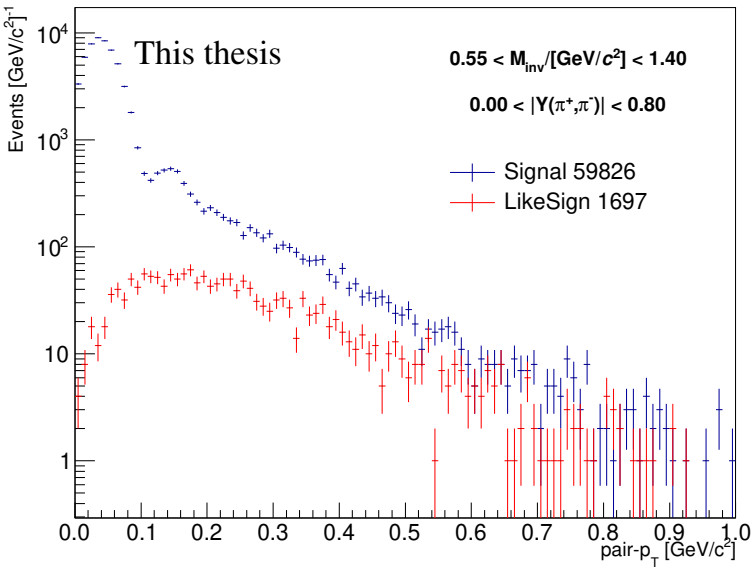

Fig. 4.19: Transverse momentum of dipion candidates for opposite-sign and like-sign events.

from dimuon events is estimated in the invariant mass spectrum using a fit as described below.

Invariant mass spectrum The raw invariant mass spectrum with all cuts applied and before the correction on acceptance and efficiency can be seen in Fig. 4.20. The peak originating from ρ^0 to two pion decay is clearly visible. The contamination from combinatorial background is around 1.4% as that is the portion of like-sign events after the same selection and it will be statistically subtracted bin-by-bin before the correction on acceptance and efficiency of the detector. The number of events above 1.4 GeV/c^2 is extremely low and can be contaminated by other resonances. Therefore, we applied a cut and they were not used in the fitting procedure. In total, 56699 events remain for further analysis after all selection criteria were applied.

4.2.5 Correction factors

Acceptance and efficiency The product of the acceptance times efficiency (AxE) to measure the coherently produced ρ^0 vector meson is determined using event samples generated with the STARlight generator. Two different samples are used: one of pure coherent ρ^0 photoproduction generated with a Breit-Wigner distribution and the other produced with a flat

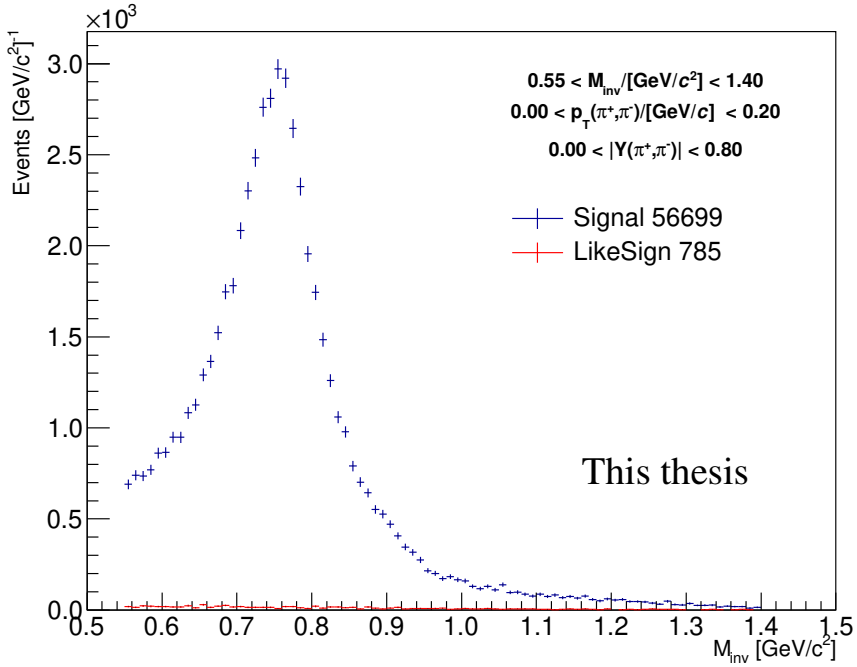

Fig. 4.20: Raw invariant mass spectrum with like-sign contamination.

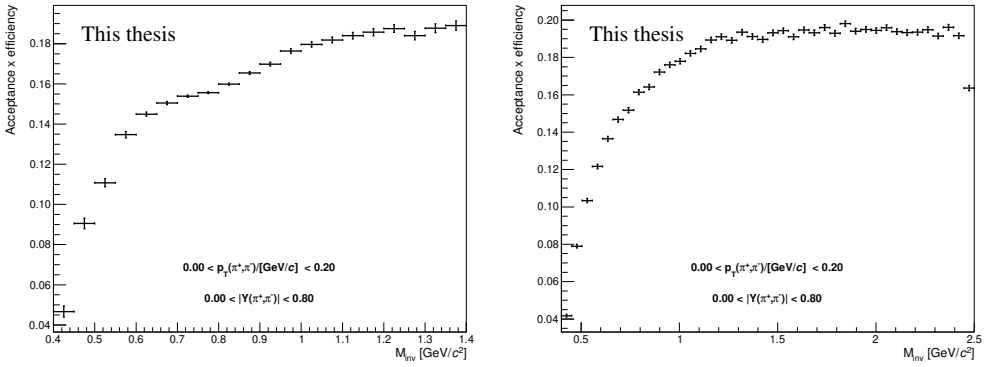

Fig. 4.21: Acceptance x efficiency obtained from STARlight (left) and flat-mass distribution (right).

mass distribution. The generated events pass trough an ALICE GEANT 3 simulation and then through the full analysis and selection criteria in order to reproduce detector and analysis effects.

The invariant mass histograms of selected events are then divided by the histogram of generated events. This procedure is needed because the AxE at low invariant mass is not constant but shows a steep dependence due to the

reconstruction of soft tracks in the TPC.

The computed AxE is shown in Fig. 4.21. Both approaches yield similar correction functions for the invariant mass spectrum. The acceptance times efficiency rises smoothly from 15% to 19% in the mass range from 0.6 GeV/c^2 to 1.2 GeV/c^2 and remains constant for larger masses. Around the invariant mass where the ρ^0 peak is expected (0.77 GeV/c^2), the STARlight AxE has smaller statistical errors due to the larger number of generated events in the Breit-Wigner peak compared to the flat mass AxE, resulting in a better description of the ρ^0 peak.

Also a small dip in this area is present in comparison to the flat mass simulation. The reason for this feature is the bin migration effect: due to the larger number of events in the peak, some portion of events is spreading to neighbour bins because of the reconstruction resolution. This dip is not present in the flat mass AxE as each bin contains approximately the same amount of events. Overall, the same migration effect is expected in data, therefore the STARlight AxE will be closer to the real reconstruction effects. The comparison of both AxE will be discussed in Sec. 4.2.9 dedicated to systematic studies.

SPD trigger efficiency We already discussed the 0STP part of the trigger, the trigger-track matching procedure, and showed the code for the back-to-back topology. However, we need to take into account the efficiency of SPD fast-OR chips for all MC samples. There are two possible solutions.

The first and the easy one was used for the preliminary results presented in the form of poster at Quark Matter 2017. The idea is to use a control trigger that does not contain the 0STP part: in this case, the CTEST60 (*0VBA *0VBC *0UBA *0UBC 0OM2) trigger was used in LHC15o period. We used these data and we selected events that are similar to our selection criteria as much as possible (in total 1757 events). Then in this sample we manually asked for the 0STP trigger input on top of CTEST60 and the resulting number of events was 1270. Dividing these numbers we can estimate the effect (72.3%) of the 0STP trigger on coherent ρ^0 candidates. The same exercise can be done also for Monte Carlo samples as the ESD files contain implicitly all possible trigger inputs. We choose (CCUP9+0OM2) and (CCUP9+0OM2-0STP) to test 0STP alone. The resulting factor was found to be 85.5%. As the MC sample does not contain 0STP trigger efficiencies (there is an assumed efficiency of 100% for each chip), the ratio of these factors is our searched correction factor on SPD trigger efficiency.

Two notes are worth mentioning. Firstly, note the limited number of events in CTEST60 resulting in a large uncertainty of this correction fac-

tor. Also it is not possible to test any dependence on the invariant mass or transverse momentum spectra. That is the main reason why the second method described below was used in the final analysis. Secondly, using real data taken by the control trigger and testing the whole 0STP trigger effect, we avoided misfiring the trigger due to soft tracks mentioned above as this effect is already included in this correction and the trigger-track matching procedure is not needed (and was not used in the preliminary results).

The second method of estimating SPD read-out chips efficiency is based on a data-driven approach using a minimum bias trigger. Tracks selected without requiring two hits in the different SPD layers are matched to the read-out chips they cross. A chip inefficiency affects each track, and thus each event, differently. This method was done by the ALICE UPC group and provides SPD chip efficiencies for each SPD chip separately and also for each run. The output of this method is then incorporated into the Monte Carlo samples and applied event-by-event. The loaded efficiency for each chip is compared to a randomly generated number to simulate the efficiency of each chip. The overall effect corresponds to a global correction of about $(17 \pm 1)\%$.

In the end, both methods provided a fair and compatible description of the SPD efficiency correction factor. Using efficiencies for each chip results in smaller systematic uncertainty, however some sort of soft track-trigger matching protection has to be used to avoid misfiring of the SPD trigger.

Pile-up correction Presence of the pile-up in the ALICE detector can result in a significant underestimation of the cross section. Pile-up comes from several sources but it can be viewed as additional signals in our data. This has several consequences.

1. It will affect the trigger veto decision and discard a potentially valid event.

2. Additional tracks can reject an event in the analysis stage, for example it will not pass through the "two tracks only" cut.

3. The EMD pile-up is expected in the ZDC detector, misidentifying a no-neutron (0n0n) event as an event accompanied with a forward neutron (0nXn or XnXn).

The CCUP9 trigger includes 0STP and a veto on any activity in V0 and AD (0VBA, 0VBC, 0UBA, and 0UBC components of the trigger). The use of the veto is dangerous since any noise or an accidental charged particle

can discard the event of interest. Therefore, the trigger efficiency has to be corrected for the effect of wrong vetoing.

This can be studied using CTRUE triggered events (a downscaled no bias trigger which is fired by the bunch-bunch crossing time). The idea of this first method is to study each veto detector separately and to find the probability that a veto will be hit in an otherwise 'empty' event. That will reveal the probability of an additional signal in the event causing a veto.

To illustrate the process with an example: let's study 0VBA. We will calculate the ratio of the number of events with a hit in the 0VBA and no hits in 0VBC, 0UBA, 0UBC and no tracklets in the barrel, to the number of events that have no hits in 0VBC, 0UBA, 0UBC and no tracklets in the barrel. Obviously, the former is a subset of the latter and reveals the searched probability. Similarly, we can estimate the probability for other online vetoes (VBC, UBA, UBC) and also offline decisions (VDA, VDC, UDA, UDC).

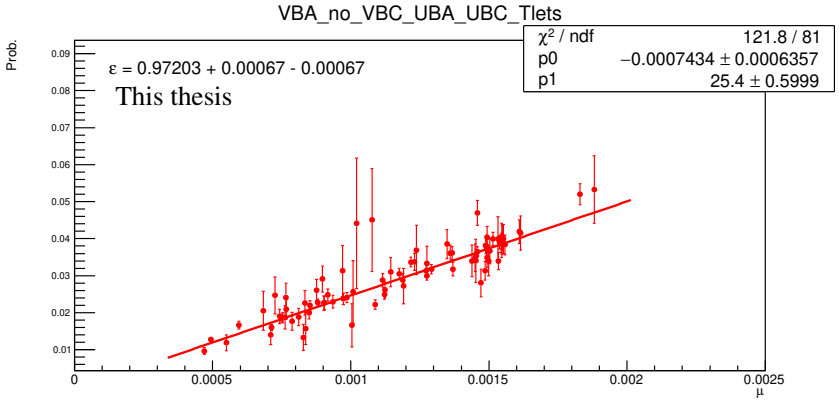

Fig. 4.22: Example of the calculation of the pile-up correction factor for the V0A trigger element (VBA). All figures in Appendix B.4.

These probabilities are calculated for each run that belongs to our selection. One could expect that this probability grows with the increase of the hadronic interaction rate and therefore with the hadronic pile-up probability μ (average number of inelastic hadronic collisions per bunch crossing) that is computed for each run. The probability, calculated as a function of μ, is presented in Fig. 4.22 and shows a clear linear dependence. The final probability is then computed as a weighted average of the luminosity of each run in our analysis. The correction factors obtained for each detector are summarised in Table 4.1 and performed fits in Appendix B.4. Notice that the correction factor on pile-up is much larger than the hadronic pile-up probability μ suggesting that this pile-up comes from electromagnetic processes as we already mentioned above.

Table 4.1: Summary of the detector inefficiencies obtained using CTRUE events.

Detector	Inefficiency
VBA	2.8 ± 0.3 %
VBC	0.3 ± 0.1 %
UBA	0.24 ± 0.08 %
UBC	0.09 ± 0.04 %
VDA	5.64 ± 0.41 %
VDC	0.91 ± 0.17 %
UDA	0.20 ± 0.07 %
UDC	0.15 ± 0.05 %
Total offline	7.3 %

The total correction factor is then obtained as:

$$f_{\mathrm{p1}} = 1/(1 - \mathrm{VDA})/(1 - \mathrm{VDC})/(1 - \mathrm{UDA})/(1 - \mathrm{UDC}) = 1.073. \quad (4.1)$$

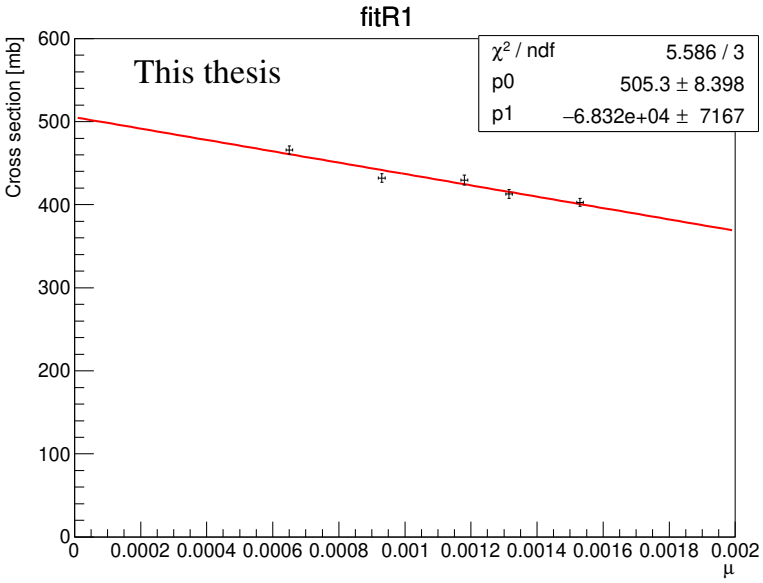

Fig. 4.23: Measured cross section for different μ-values and its extrapolation to $\mu = 0$.

The second method does not rely on the CTRUE trigger, but on analysed data, and it is the first use of this method in the UPC analysis. The

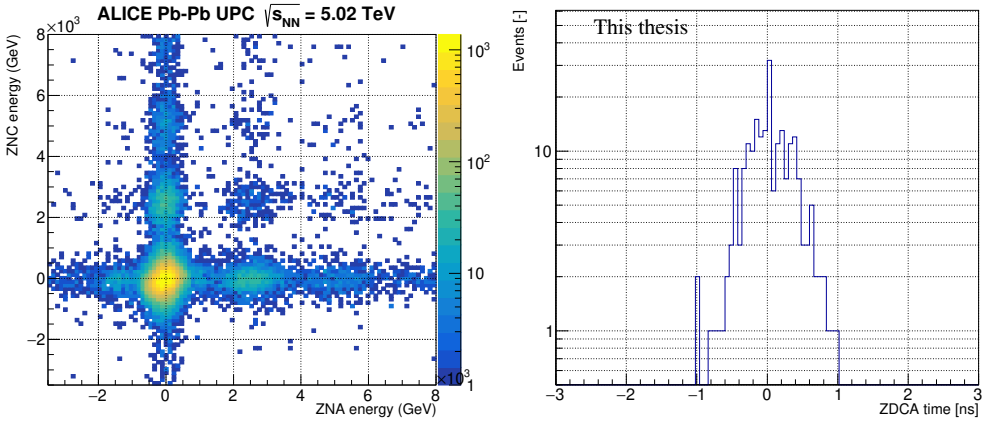

Fig. 4.24: Left: Correlation between the energy distributions of the ZNA and ZNC detectors for events selected for the analysis. Taken from [90]. Right: Time information obtained from the TDC of ZNA (only events with detected neutron have time information).

idea is based on fact that the pile-up effect on veto has to be also seen as a dependence in the measured cross section. The large dataset and wide spread of the hadronic pile-up probability μ that varied from $\mu = 0.0002$ to $\mu = 0.0015$ allows to split the data sample into five subsamples according to the expected μ–value of the run.

The luminosity of each subsample was computed and a full fit procedure was made to estimate the cross section. The result can be seen in Fig. 4.23. An expected linear dependence of the cross section is observed. Data points were fitted using a linear function and extrapolated to $\mu = 0$ as it should be the physical cross section corrected on detector pile-up. The correction factor of the second method was computed using a run–luminosity weight and estimated as $f_{\mathrm{p2}} = 1.148$.

As can be seen, there is a significant discrepancy in these two methods. It can be explained by some unknown effect in the tracking procedure as the pile-up dependence is also observed in the Monte Carlo sample. However, its origin is not proved yet and therefore an average of both methods is used as the final correction factor on pile-up ($f_{\mathrm{p}} = 1.111$) and half of the difference as its systematic uncertainty.

Forward neutron samples The analysed data are split into subsamples according to the activity in the forward neutron calorimeters ZNA and ZNC:

- ▷ 0n0n: no neutrons are visible in either side of the ALICE detector.

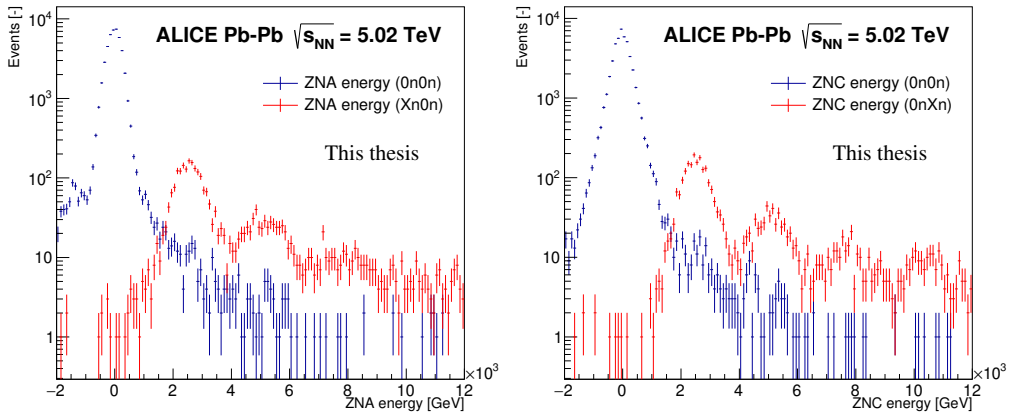

Fig. 4.25: Separation of neutron classes in ZNA (left) and ZNC (right) using a time information.

- ▷ Xn0n and 0nXn: at least one neutron is present in the A or C side but no neutrons are detected in the opposite side.
- ▷ XnXn: at least one neutron is present in each ZN.

The distribution of the energy deposited in ZDC for the selected events is shown in Fig. 4.24 (left) for both arms of the detector. The highest peak around zero corresponds to the events with no neutrons detected in the ZDC. The single and double neutron peaks are nicely seen at the beam and twice the beam energies.

The signal in the ZNA or ZNC is defined using time information from the TDC (Fig. 4.24 (right)). If any of the four TDCs has time information close to 0 ns ($\pm$ 2 ns), there is a hit from a neutron. The clean separation of neutrons from pedestal can be seen in Fig. 4.25. Using the definition of a hit, different neutron classes (0n0n, 0nXn, and XnXn) are build.

Migration in the forward neutron samples. However, events in the forward neutron sample can be misidentified due to

- ▷ The efficiency of the ZN detector: some neutrons are not detected and thus an event with neutron (0nXn or XnXn) will be identified as 0n0n or 0nXn (Xn0n).
- ▷ EMD pile-up: The EMD large cross section at LHC energies will increase the number events in 0nXn and XnXn classes that are originally 0n0n. It may also convert a 0nXn or Xn0n event into a XnXn event.

The portion of this migration between classes needs to be taken into account.

The efficiency of the ZNA and ZNC is estimated with two different methods. One uses a MC sample of events generated with the RELDIS program [43, 91] and propagated by a detailed simulation of the detector. The other method relies on a simple probabilistic model [92] applied directly to the raw data. Both methods yield compatible results, namely an efficiency of $\epsilon_{\rm A} = \epsilon_{\rm C} = (93\pm\ 1)\%$ each for the ZNA and ZNC to detect neutron activity. The propagation of this effect into the value of the measured cross sections is discussed below.

The probability of neutron pile-up in both sides ($p_{\rm A}$ and $p_{\rm C}$) was estimated using CTRUE events, a similar procedure as described above for the pile-up correction was used. The emptiness of events was defined as online+offline CCUP9 veto (0VBA or 0VBC or 0UBA or 0UBC or V0ADecision != 0 or V0CDecision != 0 or ADADecision != 0 or ADCDecision != 0). The probability of a signal in one side of the ZDC (0nXn) was found to be 3.8 %, for both sides (XnXn) a probability 0.2 % was found. Adding a requirement for no tracklets in the events results in $p_{\rm A} = p_{\rm C} = 3.3\,\%$ and 0.17 %, respectively, which was used as the main value and an error 0.3% was assigned to $p_{\rm A}$ and $p_{\rm C}$.

Moreover, events in the 0nXn and XnXn classes are also rejected when, in addition to the forward neutrons, other particles are created at large rapidities and leave a signal either in the AD or the V0 detectors. These extra particles come from the different possibilities of dissociation of nuclei, e.g. neutron emission, multi-fragmentation, or pion production, and the corresponding cross sections are expected to be large [93]. Notice that this is an extra veto inefficiency on top of the pile-up veto inefficiency discussed above and it applies only for samples with forward neutrons. The amount of good events with neutrons which are lost due to vetoes by AD and V0 is estimated using control triggers. The corrections amount to $(26 \pm 4)\%$ for events with a signal either in ZNA or in ZNC, while it is $(43 \pm 5)\%$ for events with a signal in both ZNA and ZNC [94].

The correction strategy is the following. Firstly, the 'raw' uncorrected cross-section (or number of candidates) is corrected on the veto inefficiency. Then the samples are corrected on migration, where the total cross section remains constant.

Let´s denote N as the number of observed events (or cross section) after the veto correction and before the correction on ZDC efficiency and migrations. Then denote M the corresponding number after the corrections have been applied. The number of events observed in the 0n0n class is the follow-

ing:

$$\begin{aligned} N_{\mathrm{0n0n}} &= M_{\mathrm{0n0n}} \\ &\quad -M_{\mathrm{0n0n}}p_{\mathrm{A}}(1-p_{\mathrm{C}}) \\ &\quad -M_{\mathrm{0n0n}}p_{\mathrm{C}}(1-p_{\mathrm{A}}) \\ &\quad -M_{\mathrm{0n0n}}p_{\mathrm{A}}p_{\mathrm{C}} \\ &\quad +M_{\mathrm{Xn0n}}(1-\epsilon_{\mathrm{A}})(1-p_{\mathrm{A}})(1-p_{\mathrm{C}}) \\ &\quad +M_{\mathrm{0nXn}}(1-\epsilon_{\mathrm{C}})(1-p_{\mathrm{A}})(1-p_{\mathrm{C}}) \\ &\quad +M_{\mathrm{XnXn}}(1-\epsilon_{\mathrm{A}})(1-\epsilon_{\mathrm{C}})(1-p_{\mathrm{A}})(1-p_{\mathrm{C}}). \end{aligned} \tag{4.2}$$

The first line represents the ideal case. Next three lines take into account the number of events that migrate out of this class due to pile-up, while the rest of the lines takes into account the migrations into this class due to the inefficiency of the ZN. The corresponding formulas for the 0nXn classes are:

$$\begin{aligned} N_{\mathrm{0nXn+Xn0n}} &= M_{\mathrm{0nXn+Xn0n}} \\ &\quad +M_{\mathrm{0n0n}}p_{\mathrm{A}}(1-p_{\mathrm{C}}) \\ &\quad +M_{\mathrm{0n0n}}p_{\mathrm{C}}(1-p_{\mathrm{A}}) \\ &\quad -\frac{1}{2}M_{\mathrm{0nXn+Xn0n}}[(1-\epsilon_{\mathrm{A}})(1-p_{\mathrm{A}})(1-p_{\mathrm{C}})+(\epsilon_{\mathrm{A}}p_{\mathrm{C}}+(1-\epsilon_{\mathrm{A}})p_{\mathrm{A}}p_{\mathrm{C}})] \\ &\quad -\frac{1}{2}M_{\mathrm{0nXn+Xn0n}}[(1-\epsilon_{\mathrm{C}})(1-p_{\mathrm{C}})(1-p_{\mathrm{A}})+(\epsilon_{\mathrm{C}}p_{\mathrm{A}}+(1-\epsilon_{\mathrm{C}})p_{\mathrm{C}}p_{\mathrm{A}})] \\ &\quad +M_{\mathrm{XnXn}}(1-\epsilon_{\mathrm{A}})(1-p_{\mathrm{A}})(\epsilon_{\mathrm{C}}+(1-\epsilon_{\mathrm{C}})p_{\mathrm{C}}) \\ &\quad +M_{\mathrm{XnXn}}(1-\epsilon_{\mathrm{C}})(1-p_{\mathrm{C}})(\epsilon_{\mathrm{A}}+(1-\epsilon_{\mathrm{A}})p_{\mathrm{A}}) \end{aligned} \tag{4.3}$$

and for the XnXn class:

$$\begin{aligned} N_{\mathrm{XnXn}} &= M_{\mathrm{XnXn}} \\ &\quad +M_{\mathrm{0n0n}}p_{\mathrm{A}}p_{\mathrm{C}} \\ &\quad +\frac{1}{2}M_{\mathrm{0nXn+Xn0n}}[\epsilon_{\mathrm{C}}p_{\mathrm{A}}+(1-\epsilon_{\mathrm{C}})p_{\mathrm{A}}p_{\mathrm{C}}] \\ &\quad +\frac{1}{2}M_{\mathrm{0nXn+Xn0n}}[\epsilon_{\mathrm{A}}p_{\mathrm{C}}+(1-\epsilon_{\mathrm{A}})p_{\mathrm{C}}p_{\mathrm{A}}] \\ &\quad -M_{\mathrm{XnXn}}(1-\epsilon_{\mathrm{A}})(1-p_{\mathrm{A}})(\epsilon_{\mathrm{C}}+(1-\epsilon_{\mathrm{C}})p_{\mathrm{C}}) \\ &\quad -M_{\mathrm{XnXn}}(1-\epsilon_{\mathrm{C}})(1-p_{\mathrm{C}})(\epsilon_{\mathrm{A}}+(1-\epsilon_{\mathrm{A}})p_{\mathrm{A}}) \\ &\quad -M_{\mathrm{XnXn}}(1-\epsilon_{\mathrm{A}})(1-\epsilon_{\mathrm{C}})(1-p_{\mathrm{A}})(1-p_{\mathrm{C}}). \end{aligned} \tag{4.4}$$

This set of equations is invertible and the corrected cross sections M_{0n0n}, $M_{\mathrm{0nXn+Xn0n}}$ and M_{XnXn} can be found.

The cross-check and the proof of the EMD pile-up effect can be easily found similarly to the veto inefficiency pile-up: a linear dependence of the

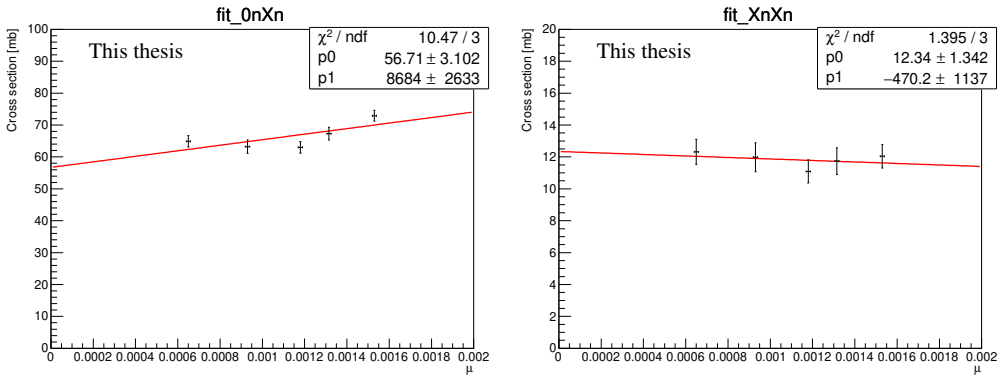

Fig. 4.26: The cross section dependence on μ in the 0nXn (left) and XnXn (right) class.

cross section on μ has to be observed. This effect is illustrated in Fig. 4.26. As can be seen, the linear dependence of the 0nXn cross section shows a mild increase with increasing μ compared to the steep decrease of the total cross section in Fig. 4.23. That can be explained as an effect of the EMD pile-up (more neutrons are detected with higher μ). In the XnXn sample a fit shows almost no dependence on μ and the veto pile-up and the EMD pile-up contributions cancel each other.

Incoherent ρ^0 The incoherent ρ^0 photoproduction is responsible for the long tail in the raw pair-p_T spectrum shown above in Fig. 4.19. It can be proved showing the invariant mass spectrum of this pair-p_T region (see Fig. 4.27). Nevertheless, some portion of the incoherently produced ρ^0 are expected also in the low pair-p_T below the chosen p_T cut. It is not possible to distinguish these events using the signal extraction method in the invariant mass spectrum described below, therefore the fitting of the raw pair-p_T spectrum method is used.

The incoherent ρ^0 was modelled using the STARlight Monte Carlo. It passed the same selection criteria in order to reproduce the analysis effects. This template is then combined with a like-sign template which is the second dominant contribution to the tail. The template was fitted to the region of transverse momentum $0.25 < p_T < 0.9$ GeV/c. Various fit ranges and binning were used (fit minimum $0.25 < p_T < 0.35$ GeV/c, fit maximum $0.6 < p_T < 0.9$ GeV/c) and binning $50 - 100$ bins) to eliminate fluctuations and estimate the fit error. In total, 100 fits were done, each with randomly chosen fit minimum, fit maximum, and binning. These fits had a mean χ^2/NDF of about 1.7.

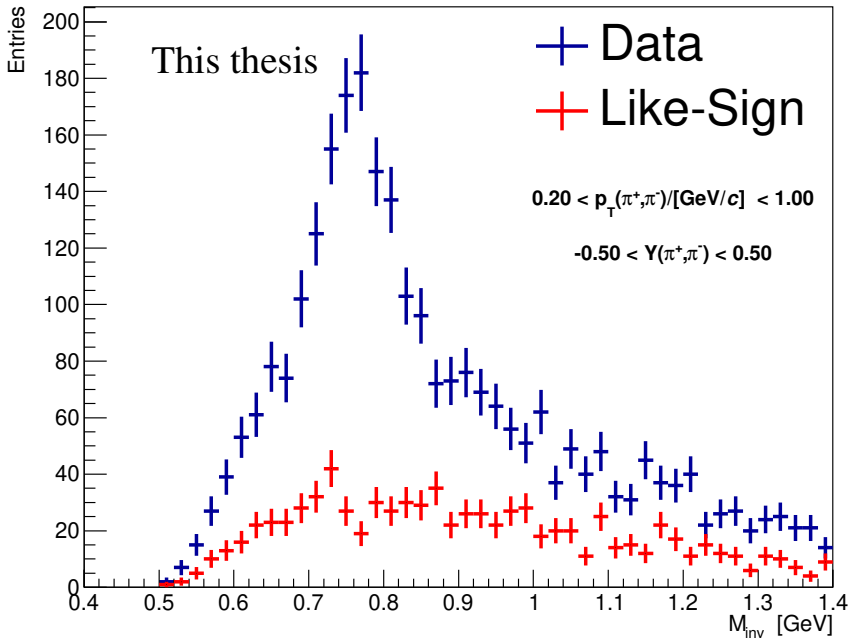

Fig. 4.27: Raw invariant mass spectrum with like-sign contamination for the high pair-p_T region proving the presence of the incoherent ρ^0 production.

As can be seen in the fit example in Fig. 4.28, the shape of the like-sign and incoherent templates is very similar. Therefore the like-sign template had to be set to a fixed value to avoid singular fit results. The like-sign normalisation factor was set to 1 as the same amount of randomly present same-sign events is expected in data. The incoherent contribution in the $p_T < 0.2$ GeV/c region was then estimated by the bin counting method. The portion of muon contamination present in this region was fixed using the STARlight prediction. The final contribution was taken as the mean of all fits and amounts to $(4 \pm 0.5)\%$. The error is taken as combination of the mean of the statistical errors and the spread of the results.

A final note on the incoherent ρ^0: Fig. 4.27 may suggest an option to fit the invariant mass spectrum. The extraction of incoherent contamination would sadly not be beneficial: the procedure is complex and the final systematic error would not decrease substantially. However, it is definitely worth a further study that is out of the scope of this work. The incoherent ρ^0 photoproduction cross section can be estimated, but a more detailed study of the trigger is needed as it is not designed to cover the higher transverse momentum region. Also the incoherent ρ^0 can be accompanied by forward neutrons and other charged particles that may affect veto signals. The amount of inco-

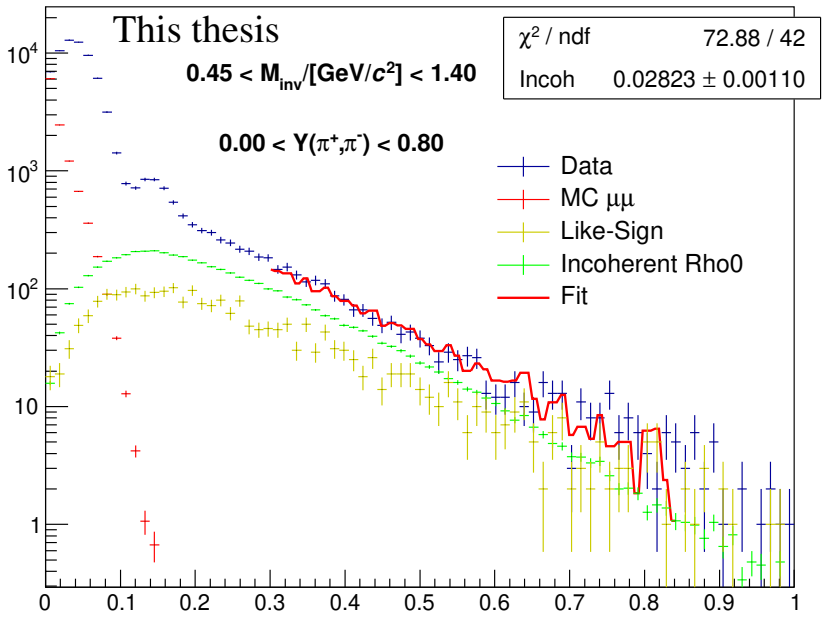

Fig. 4.28: Example of the pair-p_T fit used for estimation of contamination from incoherent ρ^0.

herent ρ^0 data in 2015 is limited and an addition of 2018 data may solve this problem. Otherwise, the samples expected in Run 3 will be ideal to perform these studies.

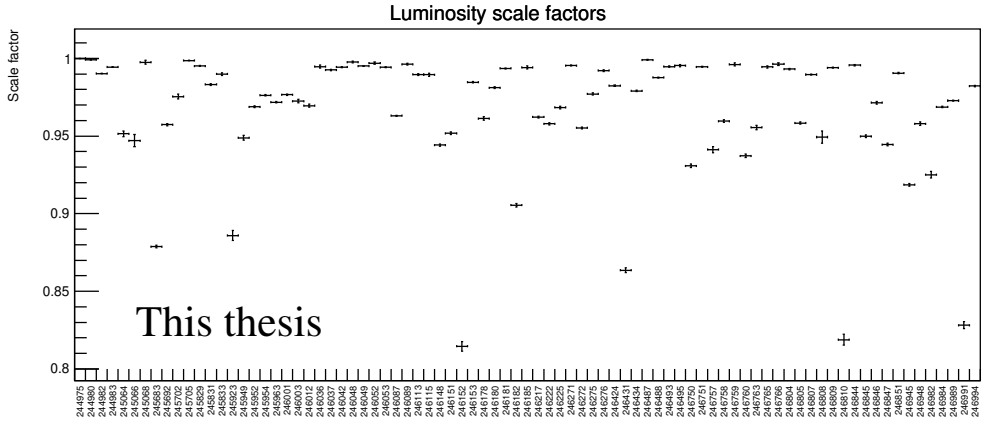

Fig. 4.29: Luminosity scale factors per run.

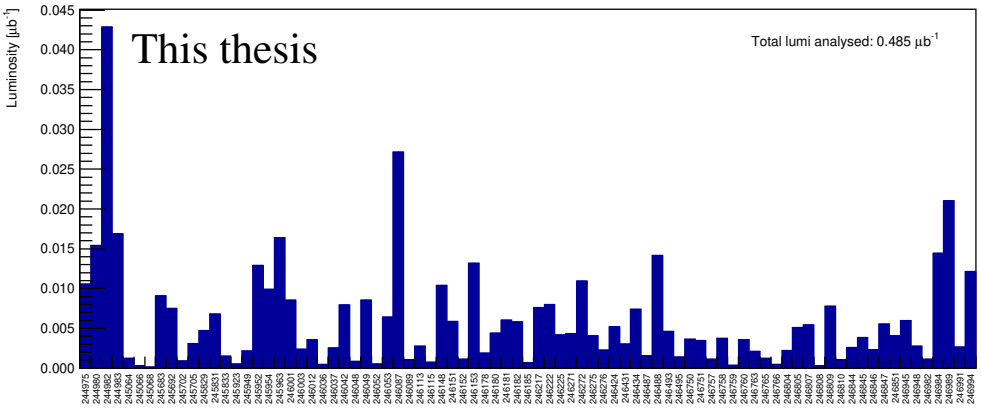

Fig. 4.30: Analysed luminosity per run.

Luminosity Run by run luminosities were calculated by the UPC group as described in an internal ALICE analysis note [95]. The luminosity is determined using a reference trigger based on the multiplicity measured by the V0A and V0C detectors. The corresponding cross section is obtained using a Glauber model for hadronic Pb–Pb collisions [96].

The analysed luminosity was scaled for the reconstruction and LEGO train efficiency run-by-run as can be seen in Fig. 4.29. The total integrated luminosity for the measurements presented below is 485 mb^{-1} with a relative systematic uncertainty of 5%. The run-by-run values are shown in Fig. 4.30. Notice that the low IR data (start of the period) contain a large amount of data compared to high IR runs due to the trigger downscaling (factor 1/200) in the high IR dataset.

4.2.6 Signal extraction

To obtain the number of ρ^0 candidates in data, a fit of the invariant mass distribution is made. Because the ρ^0 peak is spread over about 400 MeV/c^2 where the acceptance and efficiency of the detector varies substantially, the raw invariant mass spectrum has to be corrected on AxE first.

Fit functions Both Söding and Ross-Stodolsky models are implemented in the fitting macro. The fitting class is performing fits using the ROOT library.

The Söding formula is implemented in the updated version (Eq. (3.4)) to account for the ω term. The function is written in C++ and its input are eight parameters (A, B/A, m_{ρ^0}, $\Gamma(m_{\rho^0})$, m_ω, $\Gamma(m_\omega)$, C, Φ), a ninth parameter (N) is then used as a normalisation factor of the background

template. Notice that the second parameter is defined as B/A because it is a measured variable. Complex numbers are used in the following function definition:

```
Double_t SodingOmegaComplex(Double_t *x, Double_t *par)
{
  Double_t m = x[0];
  Double_t A = par[0];
  Double_t B = par[0]*par[1];
  Double_t Mrho = par[2];
  Double_t Wrho = par[3];
  Double_t Momg = par[4];
  Double_t Womg = par[5];
  Double_t C = par[6];
  Double_t Phi = par[7];

  Double_t Grho =
    Wrho*(Mrho/m)*TMath::Power(TMath::Abs(m*m-4.0*kMpi*kMpi)
      /(Mrho*Mrho-4.0*kMpi*kMpi), 3./2.);
  std::complex <double> Drho = m*m - Mrho*Mrho + 1i*Mrho*Grho;
  std::complex <double> RhoTerm = A*TMath::Sqrt(m*Mrho*Grho)/Drho;
  Double_t Gomg =
    Womg*(Momg/m)*TMath::Power(TMath::Abs(m*m-9.0*kMpi*kMpi)
      /(Momg*Momg-9.0*kMpi*kMpi), 3./2.);
  Double_t Gomgpi =
  0.0153*Womg*(Momg/m)*TMath::Power(TMath::Abs(m*m-4.0*kMpi*kMpi)
    /(Momg*Momg-4.0*kMpi*kMpi), 3./2.);
  std::complex <double> Domg = m*m - Momg*Momg + 1i*Momg*Gomg;
  const std::complex<double> i(0, 1);
  std::complex <double> EXP = std::exp(i*Phi);
  std::complex <double> OmgTerm =
    C*EXP*TMath::Sqrt(m*Momg*Gomgpi)/Domg;
  std::complex <double> total = RhoTerm + B + OmgTerm;

  return abs(total*total);
}
```

The Ross-Stodolsky model is implemented in the form of Eq. (3.7) using four parameters (f, k, m_{ρ^0}, and $\Gamma(m_{\rho^0})$).

```
Double_t RSFun(Double_t *x, Double_t *par)
{
```

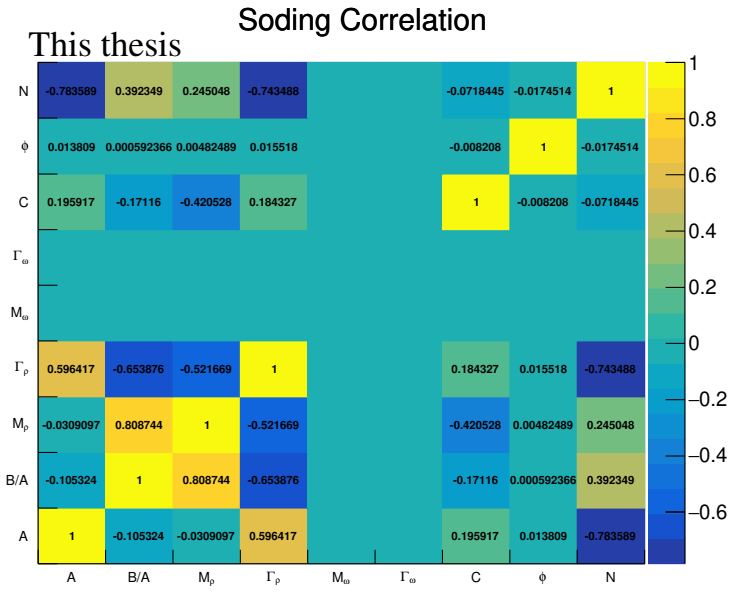

Fig. 4.31: Correlation matrix of fit parameters in the Söding function.

```
  Double_t m = x[0];
  Double_t f = par[0];
  Double_t k = par[1];
  Double_t Mrho = par[2];
  Double_t Wrho = par[3];
  Double_t Grho =
    Wrho*(Mrho/m)*TMath::Power(TMath::Abs(m*m-4.0*kMpi*kMpi)
    /(Mrho*Mrho-4.0*kMpi*kMpi), 3./2.);

  Double_t Z2 = m*Mrho*Grho;
  Double_t X = m*m - Mrho*Mrho;
  Double_t Y = Mrho*Grho;
  Double_t W = TMath::Power(Mrho/m,k);
  Double_t S = f*(Z2/(X*X+Y*Y))*W;
  return S;
}
```

Estimation of parameters Both fitting functions are quite complex functions and good estimation of the parameter's starting points and their range limits is necessary to obtained well converged results. The overview of parameters can be seen in Tab. 4.2

Table 4.2: Summary of fit parameters, their starting points, lower and upper limits.

Söding parameter	Starting value	Lower limit	Upper limit
A	1	0	100
B/A	1	-0.75	-0.35
m_{ρ^0}	0.769	0.759	0.779
$\Gamma(m_{\rho^0})$	0.149	139	159
m_ω	0.78265	0.76	0.80
$\Gamma(m_\omega)$	0.0085	0.007	0.04
C	1	0	10
Φ	1	0.5	3
N	1	0	10
R-S parameter	Starting value	Lower limit	Upper limit
f	1000	0	10000
k	4	3.3	4.8
m_{ρ^0}	0.769	0.759	0.779
$\Gamma(m_{\rho^0})$	0.149	139	159
N	1	0	10

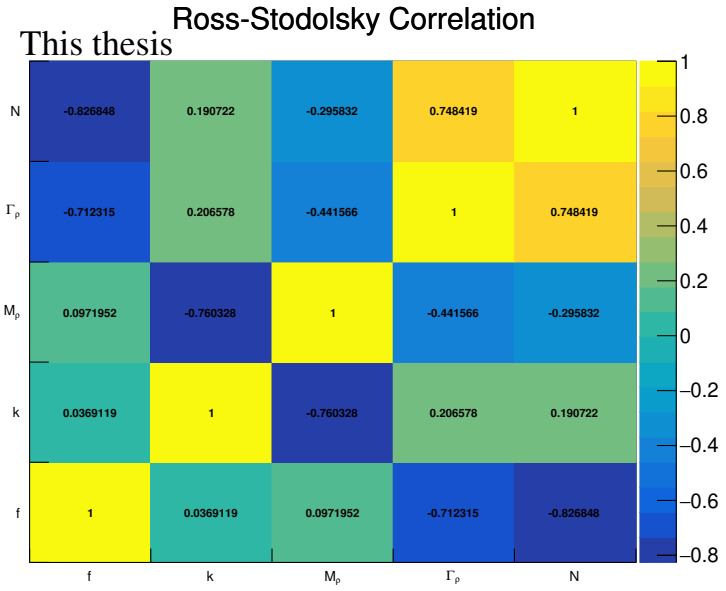

Fig. 4.32: Correlation matrix of fit parameters in the Ross-Stodolsky function.

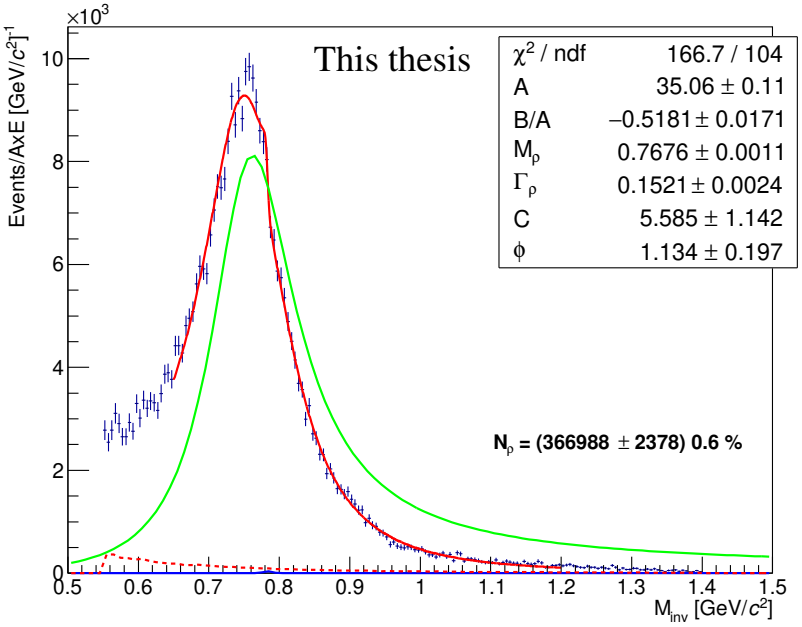

Fig. 4.33: Example fit of the Söding function.

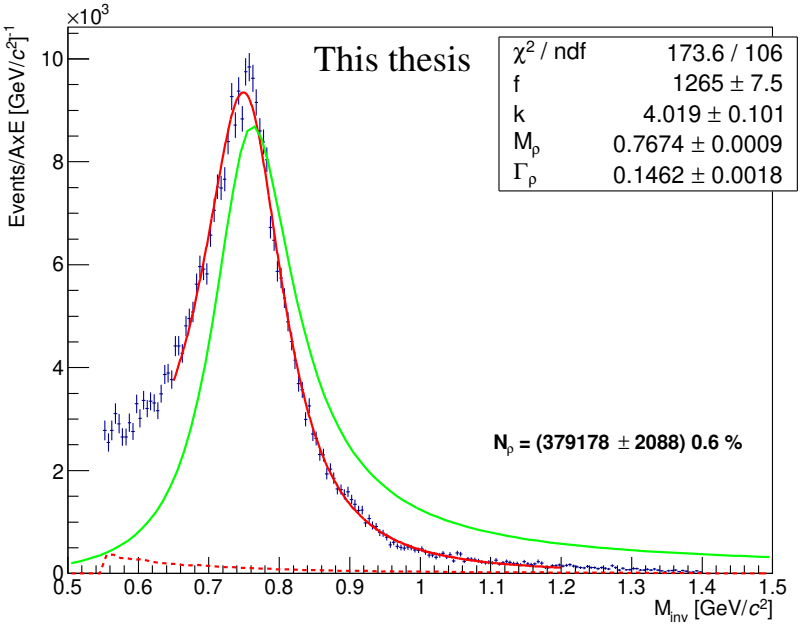

Fig. 4.34: Example fit of the Ross-Stodolsky function.

Both Söding and Ross-Stodolsky fits were performed with free parameters to study the correlation matrices shown in Fig. 4.31 and Fig. 4.32. In the Söding case, the ω mass and width have to be fixed to the PDG values otherwise the fit would not converge. Worth mentioning is a strong correlation between the amplitude parameters (A and f) and the ρ^0 width $\Gamma(m_{\rho^0})$ and background normalisation N implying that $\Gamma(m_{\rho^0})$ and N should be fixed to a prediction to avoid strong fluctuations in our bin samples. Also the skewing parameters (B/A and k) show a strong correlation with the ρ^0 mass m_{ρ^0}.

We checked that mass and width of ρ^0 are compatible with the PDG [62] values. Examples of these fits performed on the full sample can be seen in Fig. 4.33, Fig. 4.34, and the distributions over 1000 performed fits with various fit ranges and binning (described below) are shown in Fig. 4.35 and Fig. 4.36.

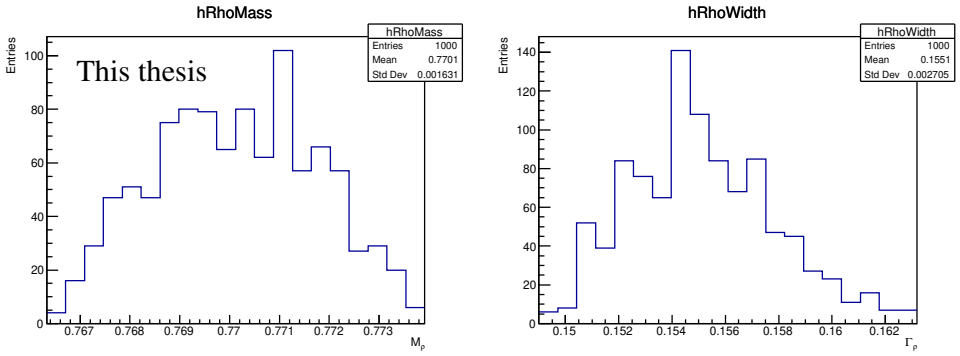

Fig. 4.35: Distribution of ρ^0 mass and width obtained by 1000 Söding fits.

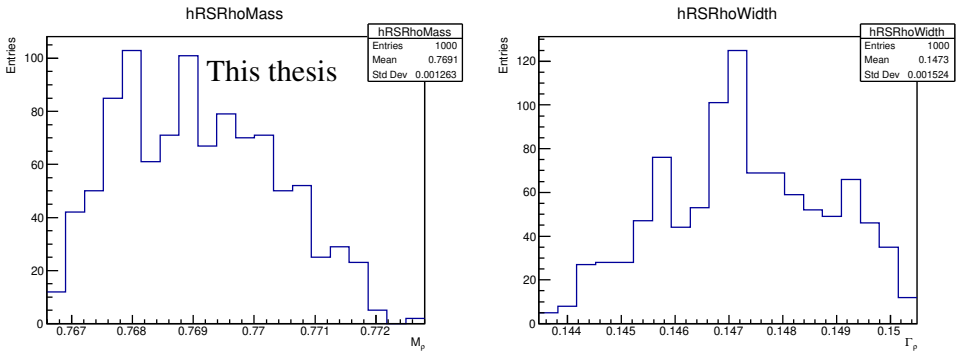

Fig. 4.36: Distribution of ρ^0 mass and width obtained by 1000 Ross-Stodolsky fits.

Based on this study and because of the correlations shown above, the

masses and widths of ρ^0 and ω were fixed to the following PDG values for subsamples to eliminate fluctuation:

- $M_\rho^{PDG} = 0.769$ GeV/c^2,
- $\Gamma_\rho^{PDG} = 0.149$ GeV/c^2,
- $M_\omega^{PDG} = 0.7826$ GeV/c^2,
- $\Gamma_\omega^{PDG} = 0.0085$ GeV/c^2.

Muon background The dominant remaining background contamination in the data sample comes from the $\gamma\gamma \to \mu^+\mu^-$ process. Because it is not possible to distinguish muons from pions in the TPC, it is necessary to take them into account during the signal extraction process. The best option is to use a template (M in Eq.(3.4) and Eq.(3.7)) from STARLight to describe the muon background. The template passed through the same analysis as data and was scaled by the same AxE as data.

In the preliminary results, the shape of this template was fitted by a sixth order polynomial function to describe the shape in invariant mass spectrum and used with a free normalisation factor N. However, during a more detailed study the strong correlation with other parameters was found causing a slight overestimating of the background. Therefore the overall normalisation factor was fixed to the expected cross section from STARLight ($N = 0.01707$). This is motivated by the $\gamma\gamma \to \mu^+\mu^-$ analysis on 2010 data, where the measured cross section was compatible with STARLight prediction within 10%. These $\pm 10\%$ were used for estimation of the background uncertainty.

Fitting ranges and binning To take into account statistical fluctuations and to estimate the systematic uncertainty, each spectrum was fitted using random-generated fit ranges and number of bins. For each result, 1000 fits were performed.

The lower fit limit was generated in the mass range of (0.6,0.65) GeV/c^2. This fit range is motivated by the presence of a small contamination of the so-called omega shoulder — omega decaying to three pions ($\pi^+\pi^-\pi^0$), where π^0 is not seen by the detector — below 0.6 GeV/c^2. This fit range will cover the small omega-reflection contamination into the fit systematic error. The upper fit limit was generated in the range of (1.0,1.4) GeV/c^2. The number of bins was generated in the range of (50,300) bins over the range (0.5,1.5) GeV/c^2, for smaller subsamples a maximum of 100 bins was used.

For results a common χ^2 method was used in all fitting procedures, however a log-likelihood method was used for another check giving the same results within less than 1%.

Number of candidates The number of ρ-candidates from the fit was obtained by integration of the BW_ρ part of the Söding function (setting parameters $B = 0$, $C = 0$, and $N = 0$ in Eq.(3.4)) and similarly for the Ross-Stodolsky function ($k = 0$ and $N = 0$). The standard integration range ($2m_\pi$,$M_\rho^{PDG} + 5\Gamma_\rho^{PDG}$) was used. The error was computed using the covariance matrix narrowed to only the BW parameters, other parameters were set to zero.

For each result, 1000 fits with randomly generated binning and fit ranges were used. The number of candidates was then taken as the average over all fits and its RMS was taken as the systematic uncertainty of this extraction. The full list of figures can be seen in Appendix B.5 and the obtained values are summarised in Tab. 4.3.

Omega The presence of the ω meson can be found in the data sample in several ways. Firstly, it can be seen also in the $\pi^+\pi^-$ decay mode on top of the ρ^0. That is described by the third amplitude term with coefficient C in the updated Söding formula (Eq.(3.4)). However, its branching ratio to pions is only 1.53 % and together with its small predicted cross section it is impossible to spot a peak in the data. Fortunately, the interference between ω and ρ^0 terms is causing a noticeable change ("a kink") in the shape of the ρ^0 peak around the ω mass.

Secondly, the dominant (89.2 %) decay channel of ω is to $\pi^+\pi^-\pi^0$. The π^0 is usually not detected by ALICE detectors and therefore such events have to be looked for in the data sample. Missing π^0 means that the invariant mass of the $\pi^+\pi^-$ pair will be lower than the ω mass and their pair-p_T will be higher. The expected shift can be predicted by STARlight: the mean pair-p_T is expected to be 0.2 GeV/c. The mean invariant mass is expected at 0.55 GeV/c^2 with upper limit at 0.65 GeV/c^2. The excess events can be seen as a bump in this region, usually called the ω-shoulder.

The ω-shoulder is not noticeable in the data. For safety reasons, the lower fit limit was chosen in the range of (0.6,0.65) GeV/c^2 where the ω presence in the coherent region of the data sample is expected to be low or none.

The interference sign of coherent ω production is seen in the signal as a small kink in the mass spectrum. Performed fits (Fig. 4.35) suggested the presence of ω. The bin width has to be kept very small as the interference is restricted to a very small mass region. That resulted in large statistical

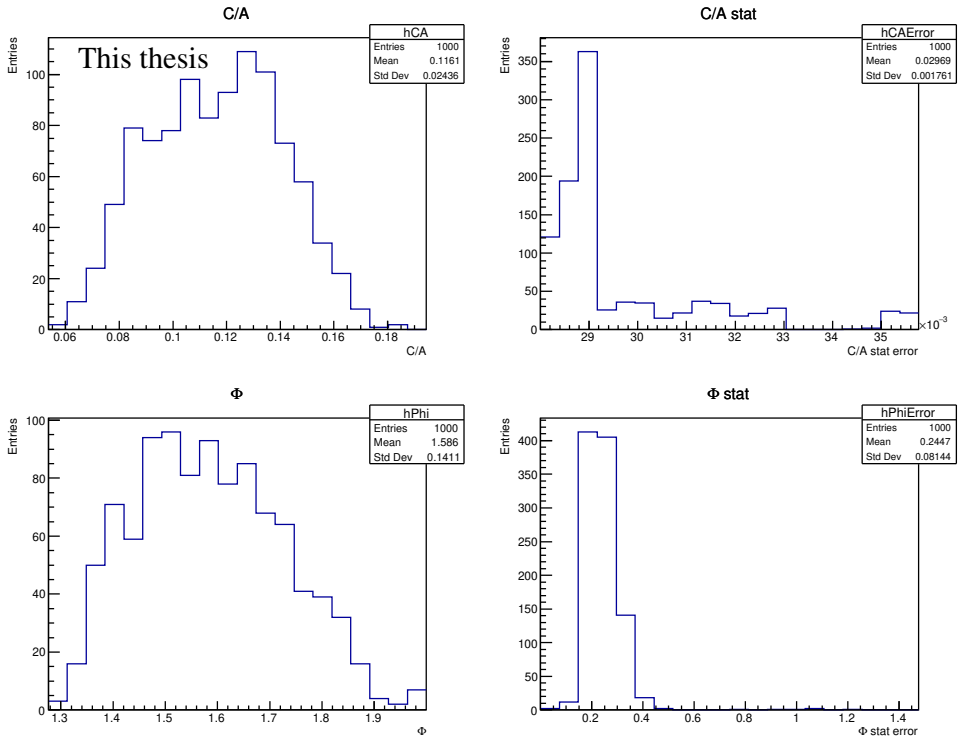

Fig. 4.37: Distribution of results for performed fits on ω.

uncertainties of these bins. Fit results averaged over 1000 fits can be seen in Fig. 4.37. Overall, fits are very unstable due to the limited amount of data. The extracted C/A ratio spreads from 0.06 to 0.18 with mean value 0.12. The extracted ϕ ranges from 1.3 to 2.0.

4.2.7 Estimation of the B/A parameter

The $|B/A|$ ratio, see Eq. (3.4), quantifies the contribution of the continuum in relation to the resonance production cross section. The value found at midrapidity for no forward-neutron selection is $(0.57 \pm 0.01\ (\text{stat.}) \pm 0.02\ (\text{syst.}))\ (\text{GeV}/c^2)^{-\frac{1}{2}}$, where it has been checked that most of the effects cancel in the ratio and the only remaining contributions to the systematic uncertainty are the variations in the fit procedure.

Within the current systematic uncertainties, the ratio can be taken as constant both as a function of rapidity and for the different forward-neutron classes. Nonetheless data seems to indicate a small decrease of the ratio with rapidity for the no forward selection case: $|B/A| = (0.56 \pm 0.01\ (\text{stat.}) \pm 0.02\ (\text{syst.}))\ (\text{GeV}/c^2)^{-\frac{1}{2}}$ and $|B/A| = (0.52 \pm 0.01\ (\text{stat.}) \pm 0.01\ (\text{syst.}))$

$(\mathrm{GeV}/c^2)^{-\frac{1}{2}}$ for the $0.2 < |y| < 0.45$ and $0.45 < |y| < 0.8$ intervals, respectively.

4.2.8 Cross section calculation

The cross section was estimated in several subsamples according to ZDC activity (total, 0n0n, 0nXn, and XnXn). The obtained values are summarised in Tab. 4.3. The 'raw' uncorrected cross section in Tab. 4.3 is computed as:

$$\frac{\mathrm{d}\sigma}{\mathrm{d}y} = \frac{N_c \cdot f_p \cdot f_{inc}}{\Delta y \cdot L}, \tag{4.5}$$

where N_c is the number of the Söding candidates, $L = 485$ mb^{-1} luminosity of the sample, Δy width of the rapidity bin, $f_p = 1.111$ pile-up factor, and $f_{inc} = 0.96$ correction on incoherent ρ^0. This cross section is further processed and corrected on ZDC effects as described in Sec 4.2.5.

4.2.9 Systematic uncertainties

The fit to extract the number of candidates is repeated choosing random combinations of the lower and upper limits of the fit range as well as of the bin width. The lower and upper limits are varied in the ranges (0.6,0.65) GeV/c^2 and (1.0,1.4) GeV/c^2, respectively, while the bin widths are varied within the (0.05, 0.2) GeV/c^2 interval. Results reported below, as well as the above quoted values for the pole mass and width of the ρ^0, are an average of the values obtained in these fits, while the RMS provides the systematic uncertainty, which varies from 0.4% to 5.9%, the largest values corresponding to the XnXn sample. The statistical uncertainty is taken as the average of the statistical uncertainty of each one of the fits. This uncertainty is uncorrelated across rapidity and forward neutron classes. The fit procedure is performed using both a χ^2 approach and a binned extended log-likelihood. The results from both methods are consistent.

A Ross-Stodolsky function Eq.(3.7) without ω contribution is used as an alternative model. This model yields cross sections larger by 3.5 % than those obtained from the Söding model with $C = 0$. A test using randomly generated data with a Söding model fitted with the Ross-Stodolsky function and vice versa was performed. In both cases a similar difference of around 3.0% was found. As the underlying distribution is not known, the 3.5 % difference observed in data is considered as a systematic uncertainty.

The uncertainty on the track selection is estimated by changing the selection criteria within reasonable values and repeating the full analysis. We varied the minimum number of TPC points per track in the range 70-90,

Table 4.3: Estimated number of candidates and its statistical and systematical uncertainties obtained from fits in each rapidity bin and neutron sample. The 'raw' uncorrected cross-section (CS) is estimated using Eq. 4.5

Total	Söding cand.	stat.	syst.	R-S cand.	stat.	syst.	CS [mb]
$\|y\| < 0.2$	91060	780	385	94360	800	290	500.4
$0.2 < \|y\| < 0.45$	114300	939	545	118400	960	420	502.5
$0.45 < \|y\| < 0.8$	162300	1452	640	167500	1500	550	509.6
0n0n							
$\|y\| < 0.2$	76000	699	771	78750	713	730	417.6
$0.2 < \|y\| < 0.45$	95570	843	824	98970	862	754	420.1
$0.45 < \|y\| < 0.8$	134700	1303	913	138900	1340	900	423.0
0nXn							
$\|y\| < 0.2$	14110	290	181	14610	296	162	77.5
$0.2 < \|y\| < 0.45$	17280	347	192	17890	353	187	76.0
$0.45 < \|y\| < 0.8$	24710	540	302	25570	552	282	77.6
XnXn							
$\|y\| < 0.2$	2417	127	142	2528	123	125	13.3
$0.2 < \|y\| < 0.45$	3030	145	93	3119	147	96	13.3
$0.45\|y\| < 0.8$	4442	231	109	4580	235	113	13.9

maximum χ^2/NDF from 3.5 to 4.5, compared the number of events of two TPC regions and lowIR and highIR runs. The uncertainty corresponds to the full variation of the results and amounts to ±1.5%. The uncertainty on the matching of TPC and ITS tracks is obtained by comparing the behaviour of real and simulated data under different detector conditions; it amounts to ±4%.

The uncertainty on the acceptance and efficiency to reconstruct the ρ^0 vector meson is estimated from the full variation of the results while using the two different MC samples discussed above. It amounts to ±1%.

The uncertainty on the normalisation of the template for the $\gamma\gamma \to \mu^+\mu^-$ process is estimated as follows. The statistical uncertainty of the $\gamma\gamma \to e^+e^-$ cross section in our previous measurement [97] is around 10 % and within this precision, it agrees with the prediction from STARlight, validating the use of this MC in this mass range. Changing the normalisation of the $\gamma\gamma \to \mu^+\mu^-$ template in the fit by ±10% produces a ±0.3% systematic uncertainty on the extracted ρ^0 cross section.

The fit to extract the incoherent contribution is repeated using different lower and upper limits as well as different bin widths. The respective ranges in transverse momenta are (0.25–0.4) GeV/c, (0.6–0.9) GeV/c, and bin width range (0.06–0.18) GeV/c. These variations produce a 0.5 % systematic uncertainty.

The uncertainty associated to the determination of the trigger efficiency of the SPD chips is obtained by changing the requirements on the events used for this data-driven method. Variations include the running conditions, the maximum amount of activity allowed in the event, and the definition of tracks accepted in the efficiency computation. This uncertainty amounts to 1 %.

The uncertainty on the pile-up correction from the difference of the two procedures described above is ±3.8% for the ρ^0 cross section. The systematic uncertainty due to pile-up contamination affecting the classification of the forward-neutron classes is discussed below.

Cross sections obtained in positive and negative rapidity ranges agree within statistical uncertainties, as expected from the symmetry of the process. Similarly, cross sections for the 0nXn class with neutrons at positive rapidities are compatible within statistical uncertainties with those with the neutrons at negative rapidities.

Except the fit variations, all other sources of systematic uncertainties discussed above are correlated across different rapidity intervals and forward-neutron classes. They are summarised in Table 4.4. The total uncertainty is obtained by adding in quadrature the individual contributions.

The uncertainties on the correction for good 0nXn and XnXn accompa-

Table 4.4: Summary of the systematic uncertainties. See text for details.

Source	Uncertainty
Variations to the fit procedure	0.4–5.9 %
Ross-Stodolsky fit model	+3.5%
Track selection	±1.5%
Track matching	±4.0%
Acceptance and efficiency	±1.0%
Muon background ($\gamma\gamma \to \mu^+\mu^-$)	±0.3%
Incoherent contribution	±0.5%
Trigger efficiency of SPD chips	±1.0%
Pile-up	±3.8%
Luminosity	±5.0%
Total	$^{+(8.5-10.3)}_{-(7.8-9.7)}$ %

nied by particle production leaving a signal in the AD and V0 and being rejected due to the vetoes imposed in these detectors are estimated by varying the selection criteria in the control samples as well as by modifying the pile-up probability in these samples within their uncertainties. The uncertainty on the correction factors amounts to 4% and 5% for the 0nXn and XnXn cases, respectively. The effect of these uncertainties on the final cross sections is reported in Table 4.5. There is an effect in the 0n0n cross section due to the migrations among neutron classes discussed in a further paragraph.

The cross sections for the different forward-neutron classes have another uncertainty related to migrations across classes. It is estimated by propagating the uncertainty in the pile-up and efficiency factors in ZNA and ZNC. The uncertainty in the efficiency is obtained from the comparison between both models used to estimate it and amounts to 1% for both ZNA and ZNC. The uncertainty in the pile-up in ZDC originates from the statistical uncertainty of the different samples of unbiased events for each μ value and amounts to 0.3%. The effect of these uncertainties on the cross sections in forward-neutron classes is summarised in Table 4.6. These uncertainties only move events from one class to another, meaning that some of the uncertainties are anti-correlated among the classes. Note that the 0nXn cross section is particularly sensitive to the pile-up uncertainty. This is due to the large difference in the values of the 0n0n and 0nXn cross sections which, in the case of pile-up, produces sizeable migrations into the 0nXn class.

Table 4.5: Summary of the systematic uncertainties on the cross sections related to the correction factors to account for the events with neutrons which are vetoed by the AD or V0 detectors. See text for details. The numbers correspond to the variations of the cross sections in percentage.

Source	Total	0n0n	0nXn	XnXn
Signal either in ZNA or in ZNC	$^{-1.0}_{+1.1}$	± 0.1	$^{-6.6}_{+7.3}$	$^{+0.6}_{-0.7}$
Signal in both ZNA and ZNC	$^{-0.3}_{+0.4}$	± 0.7	$^{+0.3}_{-0.4}$	$^{-8.9}_{+10.6}$

Table 4.6: Summary of the systematic uncertainties related to the forward-neutron class selection. The percentile variation of the cross sections is shown. See text for details.

Source	0n0n	0nXn	XnXn
		$\lvert y\rvert < 0.2$	
ZDC efficiency	∓ 0.1	± 0.6	± 2.2
ZDC pile-up	∓ 0.7	$^{+5.4}_{-4.8}$	± 1.4
		$0.2 < \lvert y\rvert < 0.45$	
ZDC efficiency	∓ 0.1	± 0.5	± 2.2
ZDC pile-up	∓ 0.7	$^{+5.6}_{-5.0}$	± 1.4
		$0.45 < \lvert y\rvert < 0.8$	
ZDC efficiency	∓ 0.1	± 0.5	± 2.2
ZDC pile-up	∓ 0.7	$^{+5.5}_{-4.9}$	± 1.3

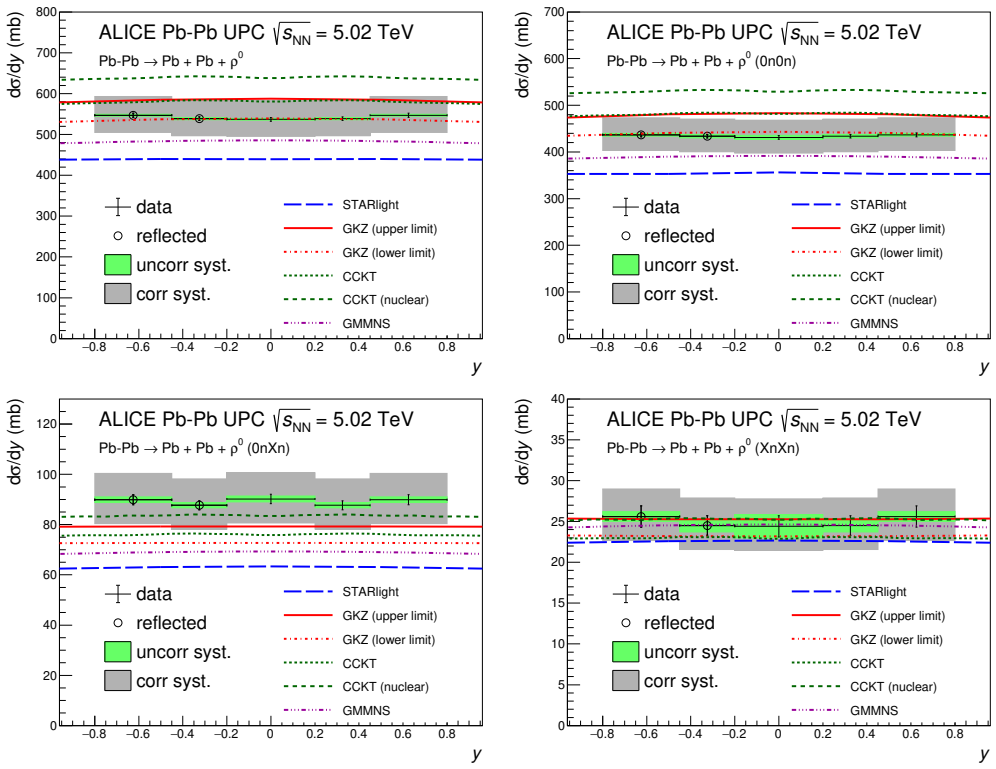

Fig. 4.38: Cross section for the coherent photoproduction of ρ^0 vector mesons in Pb–Pb UPCs as a function of rapidity for no forward-neutron selection (upper left), and for the 0n0n (upper right), 0nXn (lower left), and XnXn (lower right) classes. The lines show predictions of the different models described in the text. Taken from [90].

4.2.10 The cross section for various nuclei break-up scenarios

Fig. 4.38 shows the cross section for the coherent photoproduction of ρ^0 vector mesons in Pb–Pb UPCs as a function of rapidity. The measurements are performed for ranges in the absolute value of rapidity. For display purposes, the measurements are shown in Fig. 4.38 at positive rapidities and reflected into negative rapidities. The green bands correspond to uncorrelated systematic errors obtained by the fit variation in each bin. All other systematic uncertainties are summed in quadrature and shown as a grey band. The cross sections values are reported numerically in Table 4.7.

Table 4.7: Numerical values in mb of the cross section for the coherent photoproduction of ρ^0 vector mesons in Pb–Pb UPCs at $\sqrt{s_{\rm NN}} = 5.02$ TeV.

Total	Cross section	stat.	syst.
$\|y\| < 0.2$	537.0	4.6	$^{+46.1}_{-42.0}$
$0.2 < \|y\| < 0.45$	538.6	4.4	$^{+46.2}_{-42.1}$
$0.45 < \|y\| < 0.8$	547.0	4.9	$^{+46.9}_{-42.8}$
0n0n			
$\|y\| < 0.2$	431.1	4.0	$^{+36.8}_{-33.6}$
$0.2 < \|y\| < 0.45$	433.8	3.8	$^{+37.0}_{-33.8}$
$0.45 < \|y\| < 0.8$	436.7	4.2	$^{+37.3}_{-34.0}$
0nXn			
$\|y\| < 0.2$	90.2	1.9	$^{+10.5}_{-9.5}$
$0.2 < \|y\| < 0.45$	87.7	1.8	$^{+10.2}_{-9.3}$
$0.45 < \|y\| < 0.8$	89.9	2.0	$^{+10.4}_{-9.5}$
XnXn			
$\|y\| < 0.2$	24.4	1.3	$^{+3.4}_{-2.9}$
$0.2 < \|y\| < 0.45$	24.5	1.2	$^{+3.4}_{-3.0}$
$0.45\|y\| < 0.8$	25.6	1.3	$^{+3.5}_{-3.1}$

4.2.11 A high mass state

A high mass state at 1.7 GeV/c^2 was observed in the photoproduction of ρ^0 mesons by the STAR collaboration [84]. We observe a similar state.

The same event selection is used as in the coherent ρ^0 analysis except the mass range that is chosen in the range from 1.2 to 2.2 GeV. A large background contamination was subtracted bin-by-bin from like-sign events. The remaining signal was fitted in the range from 1.2 to 2.2 GeV using the same formula as by the STAR collaboration:

$$\frac{d\sigma}{dm_{\pi\pi}} = A \cdot \exp\left(-B \cdot (m_{\pi\pi} - 1.2)\right) + C + D \cdot \exp\left(-(m_{\pi\pi} - M_x)^2/\Gamma_x^2\right) \quad (4.6)$$

as can be seen in Fig. 4.39. The model yields a mass of (1725 ± 17) MeV/c^2 and width (143 ± 21) MeV/c^2, where the quoted uncertainties correspond to statistical fluctuations only. As shown in Fig. 4.40, this resonance-like object has very low transverse momentum as expected from a coherent-production process.

The mass M_x and width Γ_x^2 of the unknown resonance obtained from our fit is in agreement with the values obtained by STAR. We estimate the

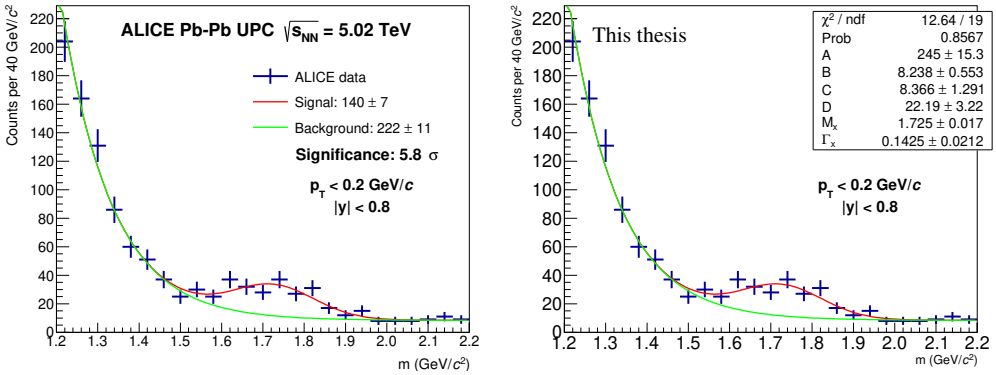

Fig. 4.39: Left: Fit of a high mass candidate. Taken from [90]. Right: Figure with the fit parameters. Only statistical errors are shown.

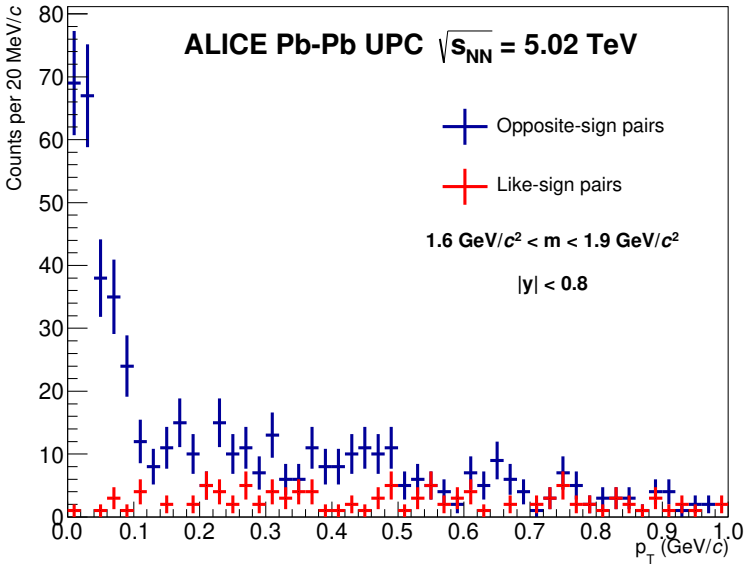

Fig. 4.40: Transverse momentum distribution for a high mass state candidates. Taken from [90].

significance of our measurement:

$$significance = \frac{signal}{\sqrt{signal + 2 \cdot background}} = 5.8\,\sigma, \tag{4.7}$$

where signal and background values were obtained by integration in the $M_x \pm 2 \cdot \Gamma_x^2$ region.

4.2.12 Discussion

In this section, the results for the coherent ρ^0 measurement in Pb–Pb UPCs [90] are discussed.

The preliminary results presented at Quark Matter 2017 were reported in only one rapidity bin for the total cross section. Methods that were used to obtain those results are slightly different to those reported as the final results published in JHEP. The main difference is a different method to correct on false triggering and non-fixing the muon background component of the fit. That leads to a slightly lower value of the reported cross section compared to the published results.

The final measured cross section is reported in Fig. 4.38 as function of rapidity for different classes on forward neutron activity (0n0n, 0nXn, and XnXn), and compared to several models (STARlight, GKZ, GMMNS, and CCKT).

Cross section Figure 4.38 shows that the lower limit of the GKZ model gives a good description of the 0n0n cross section and underestimates a little bit the 0nXn and XnXn cross sections while the upper limit of the same model overestimates the 0n0n, slightly underestimates the 0nXn and describes the XnXn cross sections. The STARlight predictions underestimate all the cross sections at around 2 sigma level, except XnXn where the difference is smaller. The behaviour of the CCKT model based on hot spots is quite similar to the upper limit of GKZ; the CCKT (nuclear) variant of this model is some 10% larger than the predictions of the original CCKT model with hot spots. Finally, the GMMNS model predicts cross sections larger than STARlight, but still underestimating the measurements except in the XnXn class.

Taking into account the spread of the models and the uncertainties of data, the agreement between the models and the measurement appears in most cases satisfactory, particularly for the predictions of the GKZ model. This overall description of data by models suggests that the method to obtain the individual photonuclear contributions to the coherent production of ρ^0 using forward-neutron classes [39, 98] may be applied to the data, especially once the uncertainties in the measurements are reduced and the spread on the theoretical predictions is better understood.

The reduction of systematic uncertainties in future measurements will be a challenging task as the main contribution comes from the luminosity measurement. The improvement on track matching can be expected after the ITS and TPC upgrade of the ALICE detector for Run 3. A large contribution to the uncertainty originates in the pile-up correction that is done by two different methods. This may be understood better in the near future, however, an

analysis on a large amount of data from different periods and various trigger classes is needed to understood its origin. The Ross-Stodolsky prescription results in a yield systematically higher by 3.5%. Pure MC studies, where signal is generated with a Söding function and fitted with a Ross–Stodolsky model, and vice versa, show a similar behaviour. This may indicate that these models are not compatible at current precision and the underlying physics of the ρ^0 skewing should be studied. The fit procedure uncertainty clearly depends on the size of the data sample. This may be explained by the correlation between the statistical and systematical uncertainties of the procedure. Overall, the statistical uncertainties obtained in the cross section measurement are excellent even in the smallest XnXn sample and the systematical uncertainties are the dominant ones.

$|B/A|$ ratio Within the current systematic uncertainties, the $|B/A|$ ratio can be taken as constant both as a function of rapidity and for the different forward-neutron classes, but data seems to indicate a small decrease of the ratio with rapidity for the no forward selection case. It would be interesting if such a trend is observed with the large data sample and its improved precision, expected from the LHC Run 3 and 4 [99].

The corresponding ratio in coherent Au–Au UPCs measured by STAR at $\sqrt{s_{\mathrm{NN}}} = 200$ GeV is $(0.79 \pm 0.01\ (\mathrm{stat.}) \pm 0.08\ (\mathrm{syst.}))\ (\mathrm{GeV}/c^2)^{-\frac{1}{2}}$ [64]. These results for production off heavy nuclear targets can be compared with those from exclusive ρ^0 photoproduction off protons. Note that value of $|B/A|$ might depend on the range in $|t|$ selected to perform the measurement, where t is the square of the four momentum transfer at the target vertex. The CMS Collaboration measured $(0.50 \pm 0.06\ (\mathrm{stat.}))\ (\mathrm{GeV}/c^2)^{-\frac{1}{2}}$ in p–Pb UPCs at $\sqrt{s_{\mathrm{NN}}} = 5.02$ TeV [78] for $|t| < 0.5\ \mathrm{GeV}^2$. The ZEUS Collaboration, using a sample of positron–proton collisions at a centre-of-mass energy of 300 GeV, reports $(0.67 \pm 0.02\ (\mathrm{stat.}) \pm 0.04\ (\mathrm{syst.}))\ (\mathrm{GeV}/c^2)^{-\frac{1}{2}}$ for their full analysed sample, and $\approx 0.8\ (\mathrm{GeV}/c^2)^{-\frac{1}{2}}$ for t values similar to those of coherent ρ^0 production in Pb–Pb UPCs [77].

Overall, the ratio of the continuum to the resonance production of $\pi^+\pi^-$ pairs seems to be sensitive to both the kinematics of the interaction and the type of the target, but no clear picture has yet emerged.

Observation of a resonance-like structure As shown in Fig. 4.39, there seems to be a resonance-like structure in the region $m > 1.2\ \mathrm{GeV}/c^2$. Such an object is also seen by the STAR Collaboration [84] albeit at a slightly lower mass of $1.65\ \mathrm{GeV}/c^2$, but with a similar width. ZEUS reports a peak around $1.8\ \mathrm{GeV}/c^2$ for exclusive electroproduction of $\pi^+\pi^-$ pairs [100]. More

recently, H1 reports a peak at 1.6 GeV/c^2 in the exclusive photoproduction of the ρ^0 meson [101]. As suggested in [84], this resonance is also compatible with the $\rho_3(1690)$ listed in the PDG, which has a total angular momentum $J = 3$ [102].

The large data samples expected in Run 3 and Run 4 at the LHC [99] may help to shed light on the origin and structure of this object.

Observation of coherent ω The interference sign of coherent ω production is seen in the signal as a small kink in the mass spectrum. The study was done on the full data sample and resulted in large statistical uncertainties. Moreover, fits are very unstable due to the limited amount of data. The extracted C/A ratio spreads from 0.06 to 0.18 with a mean value of 0.12 which is about 1/3 of the value reported by STAR [64]. The extracted ϕ ranges from 1.3 to 2.0.

The C/A ratio measurement would be particularly interesting as it was measured at STAR at an energy more than one order in magnitude lower than what can be reached at the LHC. The preliminary value obtained in this work may suggest interesting result of such measurement in the future as no change in C/A ratio is expected with energy. The ALICE data taken in 2018 may improve the extraction procedure, especially with combining both results, but most probably about 10× larger data sample will be needed in order to reduce the statistical uncertainty in bins that will allow to make a physical conclusion.

A comment on f2 In previous ALICE analysis [67] a hint of a resonance around 1.3 GeV/c^2 was seen. "This may be understood from two-photon production of the $f2(1270)$ meson followed by its decay into two pions, $\gamma + \gamma \to f2(1270) \to \pi^+\pi^-$ [67]." No such excess is however observed in the new data reported in this thesis.

4.3 Coherent ρ^0 measurement in Xe–Xe UPCs

The following section presents my work in ALICE on "First measurement of coherent ρ^0 photoproduction in ultra-peripheral Xe–Xe collisions at $\sqrt{s_{NN}} = 5.44$ TeV" published in PLB [103].

4.3.1 Data used

Collisions of ^{129}Xe (atomic number 54) took place at the LHC on October 12, 2017, at a centre-of-mass energy of $\sqrt{s_{NN}} = 5.44$ TeV per nucleon pair. In ALICE, this period was labelled as LHC17n and the data were taken with a reduced magnetic field setting of 0.2 T. The filling scheme was Single_16Xe_8_16_8_1bpi_16inj_cor, i.e. with 16 interacting bunches in ALICE.

In the corresponding fill, 6295, there are two runs with data available to be used for physics analyses: 280234 and 280235. Only run 280235 has been used in the measurement because of lack of statistics in run 280234 as discussed below.

All data were processed on ESD pass1 data because of the SPD trigger-track matching procedure. Both data and MC samples are preselected on the ALICE GRID using AliAnalysisTaskUpcRho0.cxx running in LEGO train. Namely train 267 was used for data. This class is responsible for selecting triggered events with two good-quality tracks and calculating the ρ^0 kinematic variables. Its output is only several Megabytes in the form of a TTree allowing further processing locally and fast changing of other selection criteria such as kinematics or binning.

The integrated luminosity of the data sample corrected on LEGO train efficiency is (279.5 ± 29.9) mb^{-1}.

4.3.2 Monte Carlo data

In order to reproduce detector and analysis effects, the STARlight MC was used. The generated events passed through an ALICE GEANT 3 simulation and then through the same analysis procedure as the data.

Following sub-samples are used:

- kCohRhoToPi: simulation of a coherent ρ^0 sample with a Breit-Wigner invariant mass distribution
- kCohRhoToPiFlat: simulation of a coherent ρ^0 sample using a flat (uniform) distribution in invariant mass to estimate the systematic uncertainty of the simulation due to the shape of the mass distribution

- ▷ kCohRhoToPiWithCont: simulation of coherent ρ^0 using the Breit-Wigner distribution with non-resonant pion continuum. This is the main MC used for the acceptance and efficiency as it provides the best data description.

- ▷ kIncohRhoToPi: simulation of an incoherent ρ^0 sample

- ▷ kTwoGammaToMuLow: simulation of a $\gamma\gamma \to \mu^+\mu^-$ sample used for background simulation.

The generated data belong to the LHC17k2 and LHC20f13 productions. The latter one is used for the final measurement as it provides new TOF maps. More detailed discussion is in the TOF section 4.3.6.

4.3.3 UPC trigger

The UPC group had the following triggers to select ρ^0 candidates at midrapidity in the LHC17n period:

- ▷ CCUP2 = 0OM2 *0VBA *0VBC 0SH1

- ▷ CCUP25 = *0VBA *0VBC 0STG 0OM2

- ▷ CCUP26 = *0VBA *0VBC 0SH1

- ▷ CCUP27 = *0VBA *0VBC 0STG

The meaning of the trigger inputs is:

- ▷ 0STG required two pairs of hits, each pair consisting of a hit in the inner and a hit in the outer layer of SPD such that they are in the same azimuth region (even if not in the same z region, that is, they do not need to form tracklets); the opening angle in the azimuth between the two pairs is larger than about 54 deg.

- ▷ 0SH1 required at least two fired hits in each the inner and also the outer SPD barrel.

- ▷ 0OM2 requires at least two TOF pads with a trigger signal.

- ▷ The other elements veto L0 activity in V0A (*VBA) and V0C (*VBC) within the beam-beam time window.

Some of these triggers have been downscaled. In run 280234 CCUP2 was downscaled by a factor 0.1, CCUP26 by 0.001, and CCUP27 by 0.01; while in run 280235 CCUP27 was downscaled by 0.015, CCUP26 by 0.001, and CCUP2 was not downscaled. This makes CCUP2 in run 280235 the trigger of choice for this analysis as it contains most of the data.

Notice that the CCUP2 trigger is a more open trigger compared to CCUP9 used in the Pb–Pb analysis. This will result in a larger acceptance and also larger contamination of background.

4.3.4 Event selection

The class AliAnalysisTaskUpcRho0 preselects events that fulfil the following criteria:

1. They have fired the CCUP2 trigger.
2. They have exactly two good-quality tracks.

The tracks used for the analysis (good-quality track) are required to:

- ▷ have a distance of closest approach to the event primary vertex below $0.0182 + 0.035/p_T^{1.01}$ and 2 cm in the transverse plane and in the longitudinal direction, respectively;
- ▷ be a TPC-global track refitted in both TPC and ITS;
- ▷ have more than 50 TPC clusters;
- ▷ have 2 SPD hits, one in each layer, matched to the track. This criterion is motivated by the 0STG trigger input.

The selected events are required to:

- ▷ belong to run 280235;
- ▷ have two tracks with opposite electric charges (in addition, a complementary sample with like-sign events is used for the estimation of combinatorial background);
- ▷ have n_σ(pion) from TPC PID of both particles limited by $n_{\sigma_1}^2 + n_{\sigma_2}^2 < 5^2$. This criterion effectively removes electron-positron pairs and other contamination from kaons and protons;
- ▷ have fast-OR fired SPD chips matched to the reconstructed tracks as explained below;

- ▷ have a vertex located in the z direction within $\pm 10\,\mathrm{cm}$
- ▷ have a track pseudorapidity related to TOF acceptance within ± 0.8

The selection criteria related to kinematics are:

- ▷ To have the absolute value of the pair rapidity below 0.8 to get reasonable acceptance for the pion tracks.
- ▷ A pion mass is assumed to form the momentum four-vector from the track kinematics.
- ▷ The invariant mass of the pair (under the pion hypothesis) has to be above 550 MeV/c^2. The reason for that is the selection on n_σ(pion) does not remove low mass di-electrons below this value due to overlapping $\mathrm{dE/d}x$ curves of pions and electrons.
- ▷ The invariant mass of the pair (under the pion hypothesis) has to be below 1500 MeV/c^2.
- ▷ The transverse momentum of the pair, p_T, has to be below 150 MeV/c. This is motivated by the p_T distribution expected from coherent photonuclear production.

The STARlight MC events passed the same analysis procedure as real data, using the ESD LEGO train number 281(LHC17k2) and 295 (LHC20f13).

4.3.5 Data Quality

In this section, we present information to study the characteristics of the selected data. The starting point is the data after the preselection (events with two good-quality tracks that are triggered). Distributions of variables either used in the selection process or of importance to the analysis are shown and their impact on analysis procedure is discussed. Where possible, they are compared with equivalent distributions from the MC samples.

Effects of the selection criteria on real data The number of CCUP2 recorded events in run 280235 according to the logbook is 45235. The number of events that passed each selection criterion is shown in Appendix C.1. The final number of events after all selections is 1827.

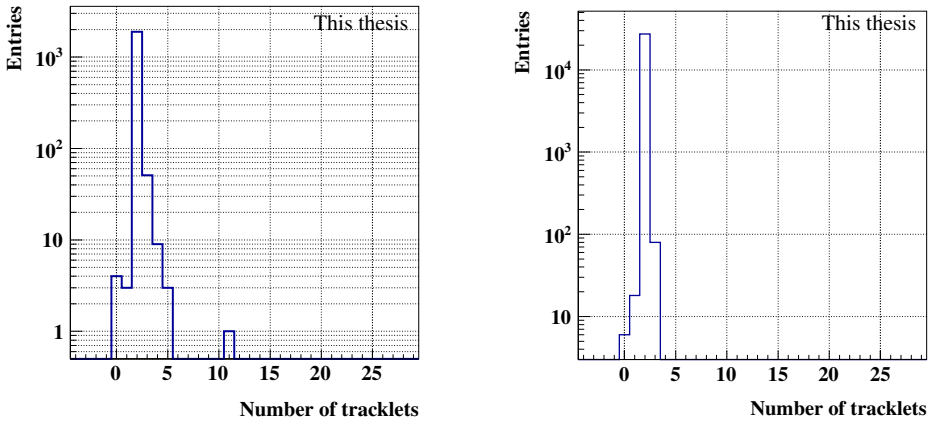

Fig. 4.41: Left: Number of tracklets after all cuts applied. Right: In Coherent MC.

Track distributions Figure 4.41 shows the number of tracklets found in the selected sample. The majority of events feature 2 tracklets suggesting that no strong soft electron-positron background is present in the ITS. That is a big difference compared to the Pb–Pb analysis that was theoretically expected as its cross section scales with Z^2.

Figure 4.42 shows the track momentum in data and MC. Notice that the track momentum obtained from the STARlight coherent ρ^0 with continuum described the data the best. The coherent ρ^0 modelled with pure Breit-Wigner distribution showed slightly different shape, however, the flat-mass distribution produced a substantially different shape of track momentum. That could explain the difference in computed acceptance and efficiency distributions that was observed also in the Pb–Pb analysis. Therefore, the coherent ρ^0 with continuum is used as a baseline for computing AxE of this analysis. The Breit-Wigner model is then used for the systematic uncertainty of the AxE as described below.

The azimuthal angle distribution of tracks is shown in Fig. 4.43. Large gaps are produced by dead SPD modules after years of service. The MC well reproduced this behaviour in the whole region. The effect on ρ^0 candidates is shown in Fig. 4.44, the overall effect is nicely described by MC.

Figure 4.45 shows the correlation between the pseudorapidity of both tracks for real and MC data. A similar pattern is found in both cases.

Vertex distribution Figure 4.46 shows the distribution of the z coordinate of the primary vertex as well as the difference found between the primary and the SPD vertices. The distributions are compared to MC. A small devia-

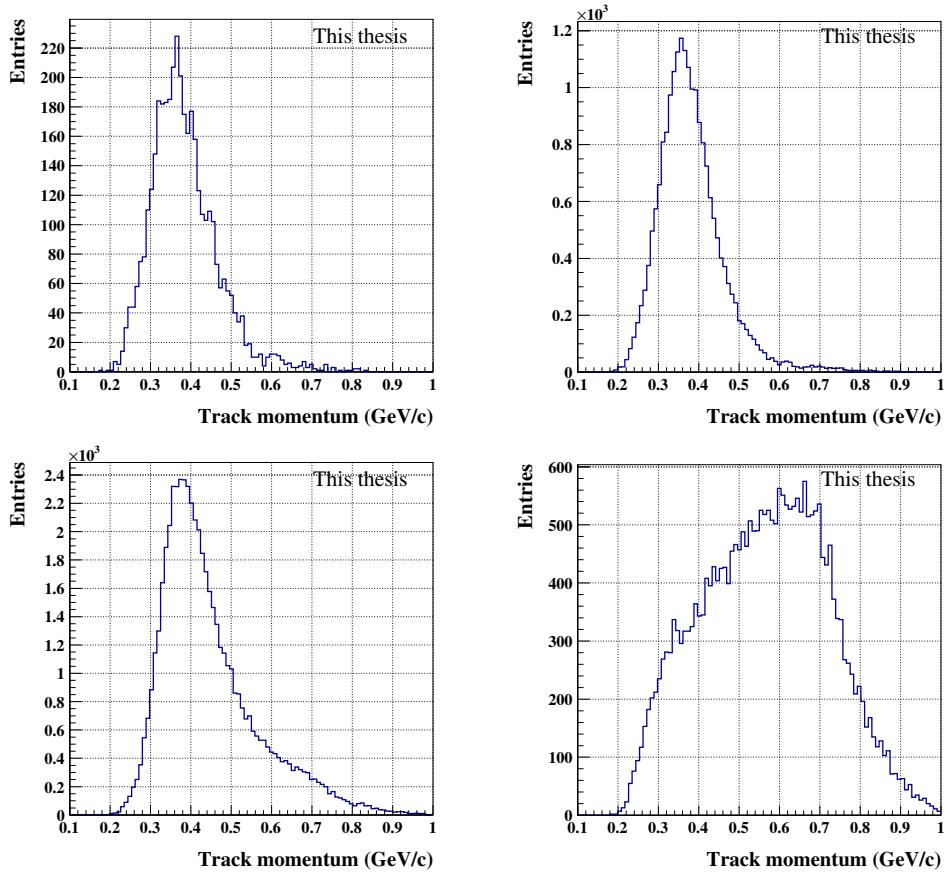

Fig. 4.42: Upper Left: Track momentum after all cuts applied. Upper Right: In Coherent MC with continuum. Bottom Left: Coherent MC with pure Breit-Wigner. Bottom Right: Coherent MC using flat-mass distribution.

tion of MC from data is observed above 10 cm from midpoint that motivates the 10 cm cut in the vertex position.

V0 and AD offline decisions The V0 and AD detectors offer the possibility to compute precise offline decision flags. The offline decisions in real data are shown in Fig. 4.47. In MC, all decisions are empty so the corresponding plot is not shown.

For the signal extraction we do not consider any offline veto, but the V0 offline veto was used for determining the inefficiency in events accompanied by electromagnetic dissociation (EMD) as described in Sec. 4.3.7. The reason for not using the offline veto is that although the final total cross sections with and without using offline decision after pile-up corrections are compat-

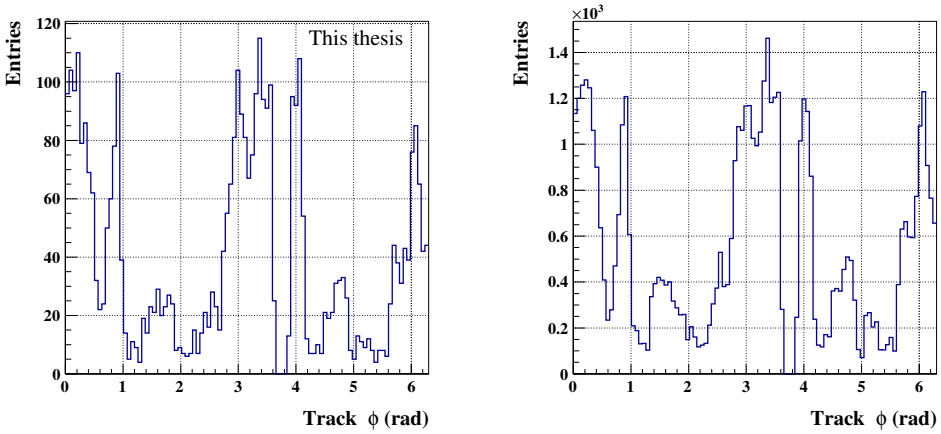

Fig. 4.43: Left: Track azimuthal angle after all cuts applied. Right: In Coherent MC.

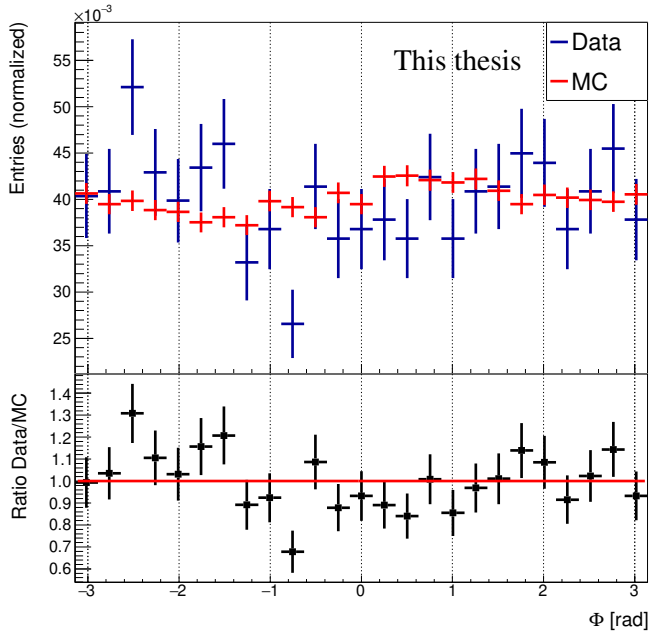

Fig. 4.44: Azimuthal angle Φ distribution of the ρ^0 candidates compared in data and MC.

ible, the small subsamples with forward neutron activity in ZDC were not compatible and they differ by about O(10) percent. We believe that the reason behind this lies in the charged pions that are commonly produced together with neutrons in the forward direction. This effect was observed in previous studies, however its production rate is not yet measured and sim-

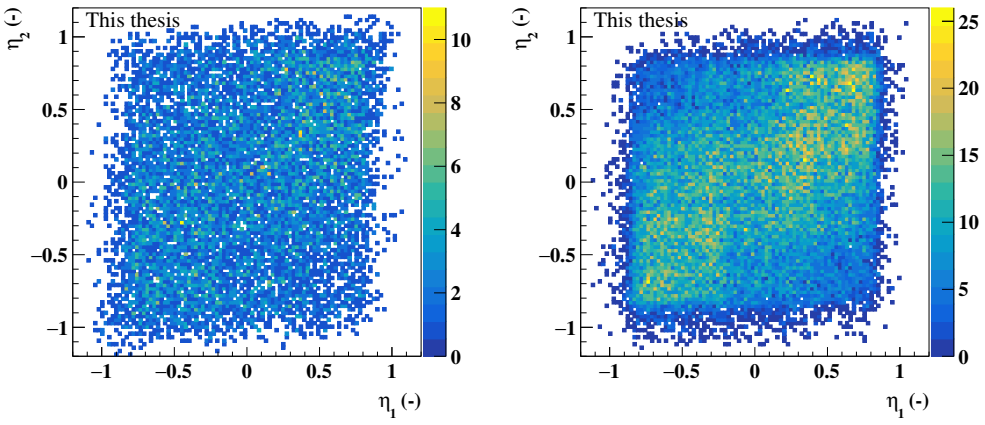

Fig. 4.45: Left: Correlation between the pseudorapidity of both tracks in data using only track selection. Right: The same distribution for coherent STARlight sample.

ulated. Therefore, we considered the best choice to not use the offline BB decisions and thus keep such events in the analysis.

Particle identification Particle identification (PID) was done using the TPC n_σ pion hypothesis. The TPC signal versus the track momentum can be seen in Fig. 4.48. Contamination from electrons, kaons, and protons is visible. The two-dimensional plot of both tracks using the n_σ pion hypothesis is shown in Fig. 4.48. Using the pion and electron hypothesis we found that we are not able to distinguish electrons from pions below 0.55 GeV. This feature was extensively studied in Pb–Pb analysis and it motivates us to include a selection on the invariant mass of the pair to be above 0.55 GeV/c^2. For these masses, the n_σ distribution in data shows that there is a clean separation of particle species. For the PID selection we decided to use the n_σ plot and make a circle cut around (0,0) with a radius of $5n_\sigma$ ($n^2_{\sigma_1} + n^2_{\sigma_2} < 5^2$).

SPD efficiencies The SPD efficiencies were simulated similarly to previous Pb–Pb analysis and then applied in each event. The systematic uncertainty was estimated using the trigger-track matching procedure described in the next section.

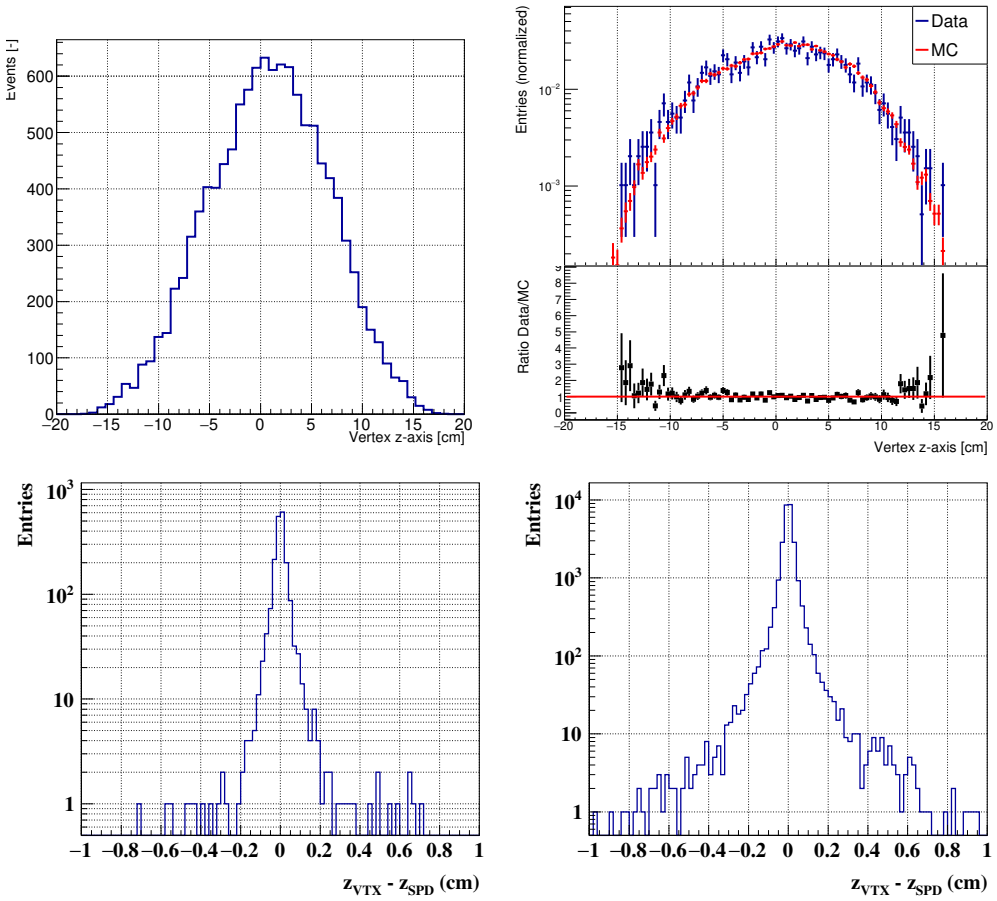

Fig. 4.46: Upper left: Vertex distribution along the z-axis. Upper right: Comparison to Coherent MC. Bottom Left: Distance between the primary vertex and the SPD vertex in data. Bottom right: Same, but for the coherent MC.

4.3.6 Trigger-track matching procedure

The trigger condition 0SH1 in SPD asked for at least two hits in the both inner and outer layers. However, some of these hits originate in soft electron-positron pairs and can fire the trigger although the pions from ρ^0 did not triggered this event (e.g. because of a dead pixel). Such event would not be accepted in our MC and therefore we have to avoid this situation.

The situation is quite similar to the one described above in Sec. 4.2.4 and it is taken care of in the same way. For each track, two chips (four in total) are found that should provide the trigger. Only if all four fast-OR chips are fired, the event is accepted (both in data and MC). Compared to previous

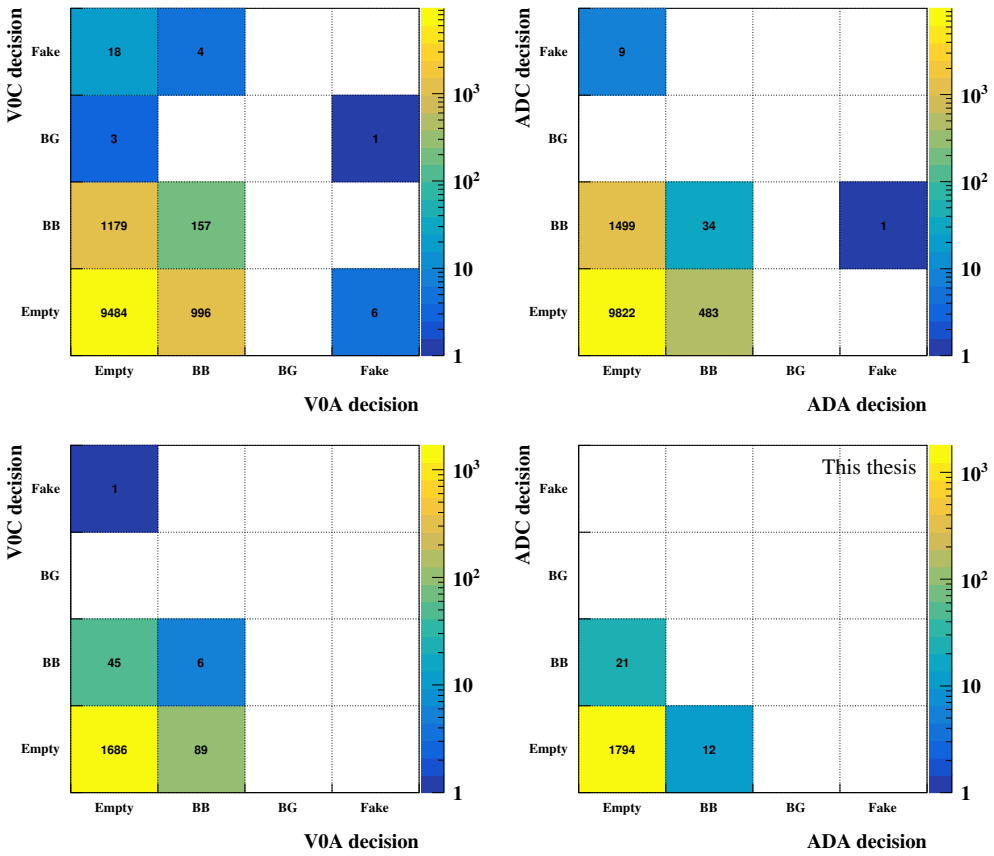

Fig. 4.47: Decisions of the V0 (left) and AD (right) detectors. Upper figures obtained using only track, run and trigger selection. Bottom figures after all selection have been applied.

Pb–Pb analysis that used a topological trigger CCUP9, no additional check on topology is needed in CCUP2.

As can be seen in Fig. 4.49, the trigger-track matching procedure has an effect of about 25% in the selected data sample. It is much larger effect than in the previous Pb–Pb analysis because CCUP2 is more open trigger than CCUP9 used in Pb–Pb. In the MC sample the effect is only 1.7% in the sample with continuum and 2.0% in the pure BW sample. The explanation could be that about 2% of events are badly described by the SPD efficiencies and it will be counted as a systematic uncertainty.

TOF efficiencies The trigger condition includes the TOF trigger input 0OM2 that requires at least two TOF pads with a trigger signal. Similarly to SPD, the pad efficiencies have to be taken into account.

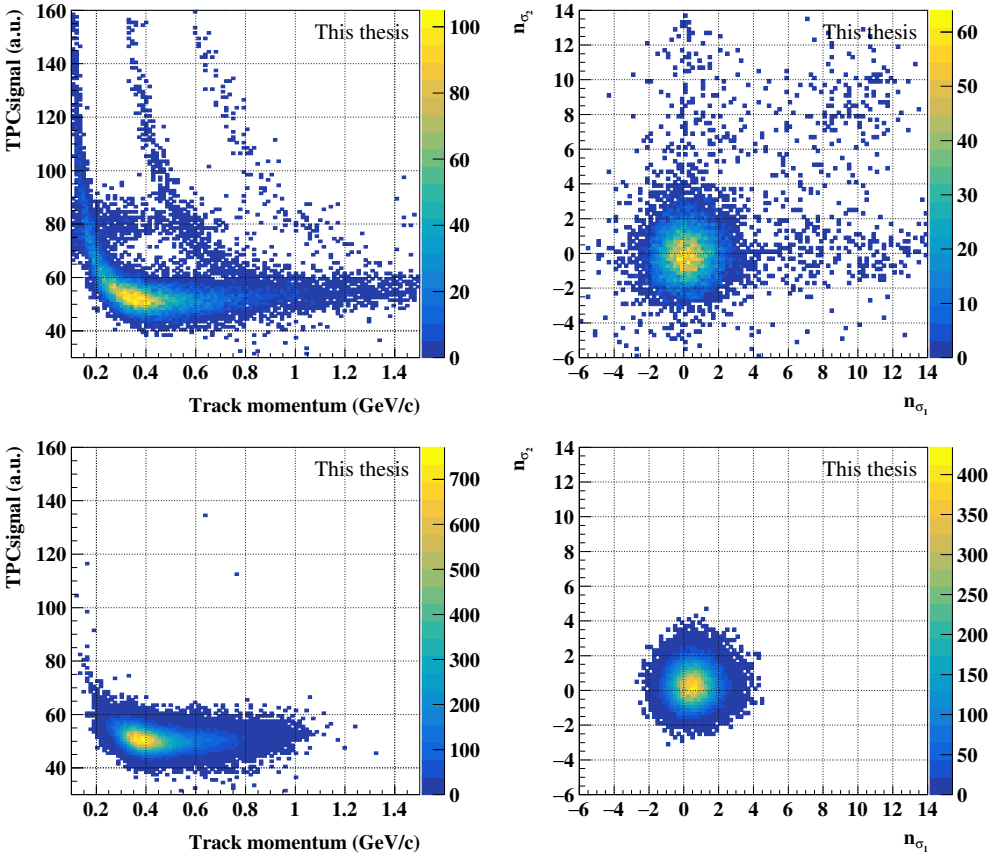

Fig. 4.48: Left: Signal in TPC versus track momentum. Right: n_σ of tracks. Figures obtained using only track, run, and trigger selection. Bottom figures for Coherent MC.

The difference in AxE using the LHC17k2 period STARlight MC sample without efficiencies and the latest LHC20f13 sample that includes TOF efficiencies maps produced a 2.8% difference that is included as a systematic uncertainty.

Rapidity of candidates The detector capability to reconstruct coherent ρ^0 is up to $|y| \approx 1$. However, at the TPC edges the amount of data is very limited and also the simulation precision in STARlight is quite poor. Therefore, we decided to use only data up to $|y| = 0.8$ to avoid large statistical and systematical uncertainties. Due to the limited amount of data in the data sample only one rapidity bin is chosen for estimating of the cross section.

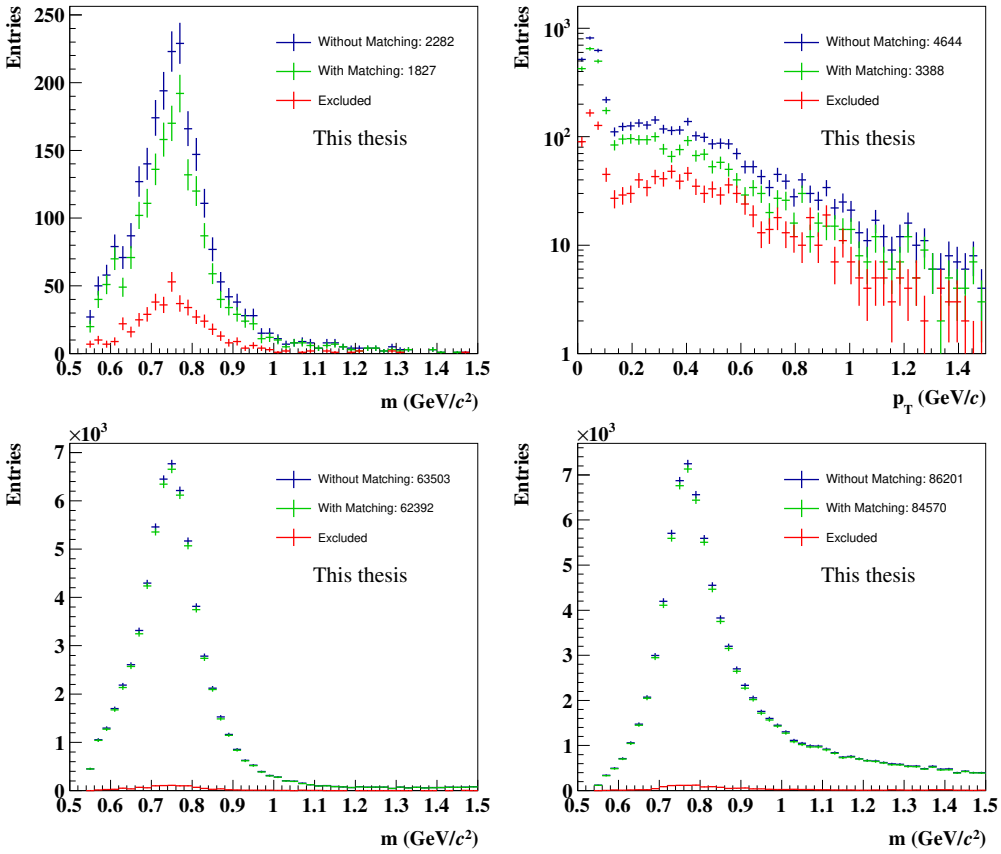

Fig. 4.49: Effect of the chip-matching procedure. Top figures for data. Bottom: MC samples.

Transverse-momentum spectrum The raw pair-p_T spectrum can be seen in Fig. 4.50. As shown in this figure there is a significant coherent peak below 0.15 GeV/c (chosen pair-p_T cut) followed by a long tail, which is partially explained by the like-sign contamination. The unexplained portion of events in the mid-p_T region originates from incoherent ρ^0 production and its contribution to the region of small momentum will be estimated using a MC template fit in the next section.

Invariant mass spectrum The raw invariant mass spectrum using all cuts and before the corrections on acceptance and efficiency can be seen in Fig. 4.51. The contamination from combinatorial background is around 1% and it will be statistically subtracted bin-by-bin before the correction on AxE. The invariant mass distribution is also shown for STARlight coherent ρ^0 samples generated with the Breit-Wigner and flat-mass distributions after

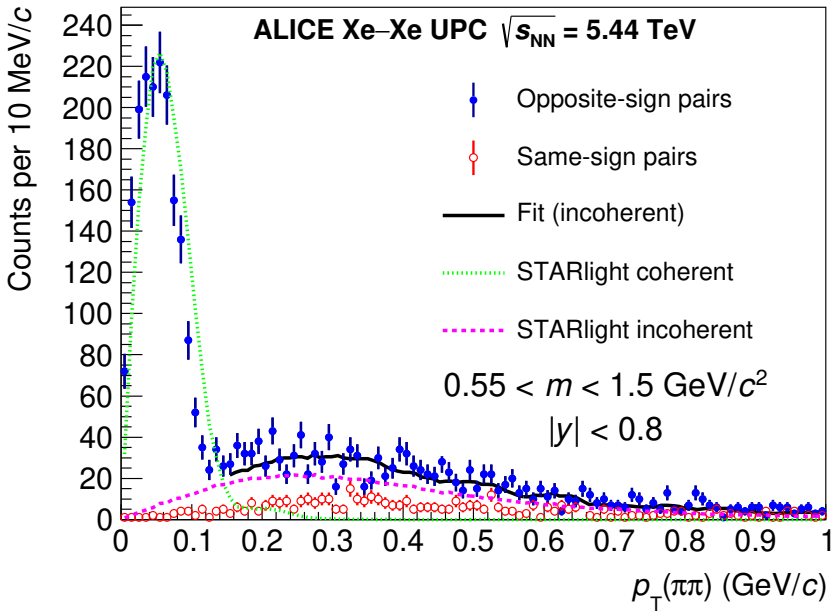

Fig. 4.50: Raw mass spectrum with like-sign contamination and fit of the incoherent contribution. STARlight MC shapes for illustration. Taken from [103].

the selection criteria were applied.

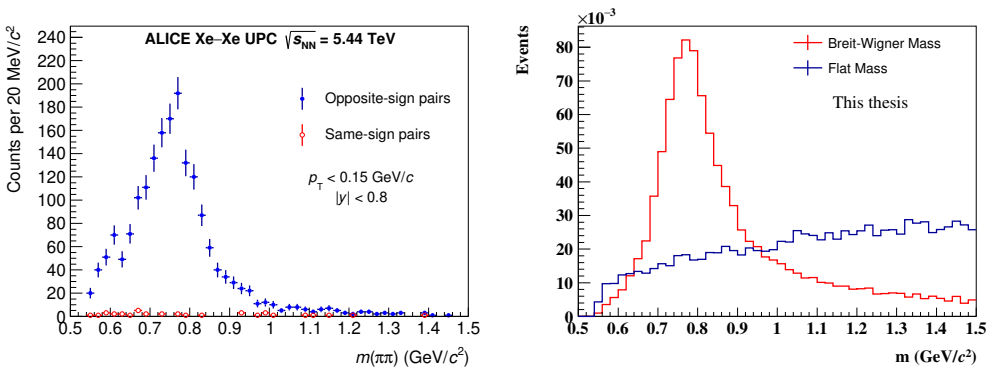

Fig. 4.51: Left: Raw mass spectrum with like-sign contamination. Taken from [103] Right: Mass spectrum of selected events for Coherent and Flat mass MC.

Energy spectra of neutrons emitted at beam rapidities Zero-degree calorimeters (ZDC) can be used to detect particles travelling at beam rapidi-

ties. Specifically in this analysis, we are using information obtained from the neutron calorimeters: ZNA and ZNC.

Using the time information we can estimate very precisely if there is at least one neutron detected in the ZNA or ZNC. The time selection requires the ZN time to be in a ± 2 ns window. Based on this we can split our data sample into 4 samples:

- ▷ 0n0n: no neutrons are visible in either side of the ALICE detector.
- ▷ Xn0n and 0nXn: at least one neutron is present in the A or C side but no neutrons are detected in the opposite side.
- ▷ XnXn: at least one neutron is present in each ZN.

The energy deposition in these calorimeters can be seen in Fig. 4.52. The 2D plot is shown in Fig. 4.53. As can be seen, the largest peak around zero is a pedestal for events where no neutron is detected by the detector. Peaks for 1, 2, and 3 neutrons are visible in the data. It is worth mentioning that the majority of events belongs to the 0n0n class and only few events are spotted as XnXn, showing that the excitation of the xenon nuclei is smaller than of the lead nuclei in previous analysis.

4.3.7 Correction factors

Acceptance and efficiency corrections

Acceptance and efficiency of the ALICE detector for coherent ρ^0 events was estimated using the STARLight MC generator. The generated events pass trough an ALICE GEANT 3 simulation and then trough the full analysis chain in order to reproduce detector and analysis effects.

We used LHC20f13 train 295 for these results. Compared to simulations with LHC17k2, it provides better TOF simulation and substantial increase in the number of generated events. The final cross section was computed using the Breit-Wigner with continuum MC sample since it describes the data better compared to only pure Breit-Wigner and flat-mass distributions. The ratio of events that passed the selection criteria to generated events (AxE) are shown in Fig. 4.54

Subtraction of the incoherent contribution

The amount of the contribution of ρ^0 vector mesons produced in incoherent interactions was estimated by fitting a template of the transverse momentum distribution of the incoherent ρ^0 production produced by STARlight. The

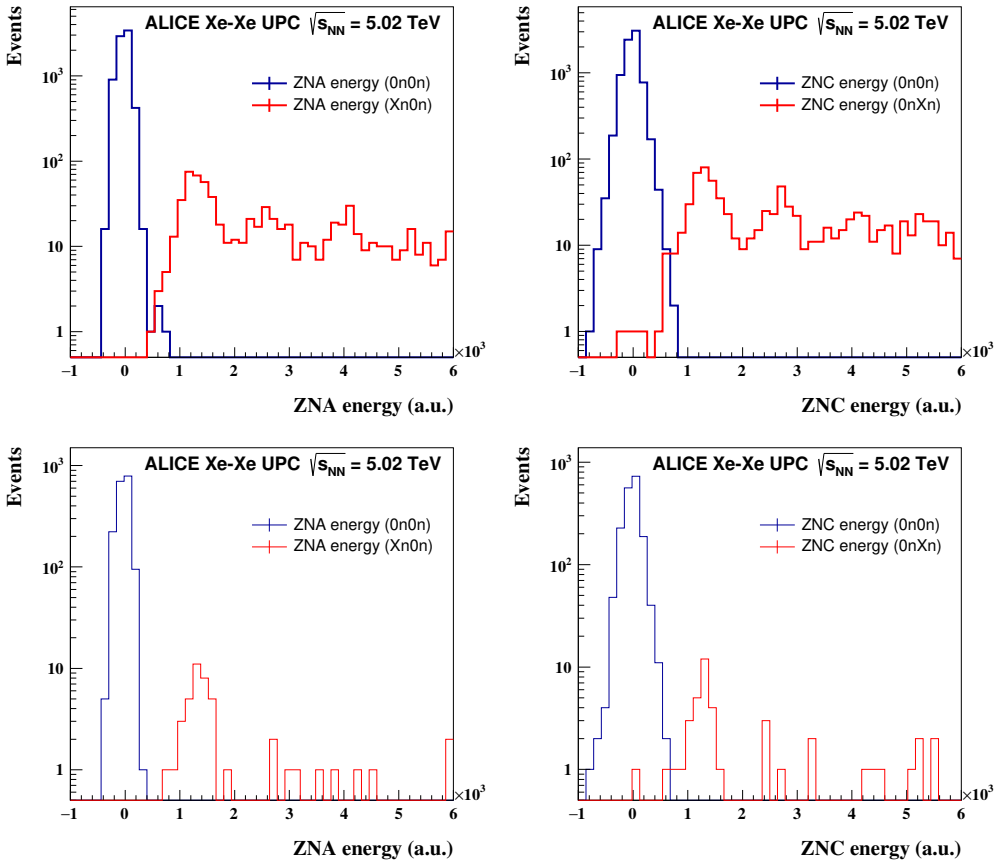

Fig. 4.52: Left: Energy deposition in the ZNA after preselection. Right: Energy deposition in the ZNC. Bottom figures after all selections applied.

method was improved compared to the method presented above in Pb–Pb analysis. Two methods of description of like-sign events are used and also this contribution is estimated in different classes with forward neutrons.

Bin widths and fit ranges (see Tab. 4.8) were randomly chosen and the final correction factor is computed as an average over 100 fits.

The fraction of incoherent candidates was estimated by the bin counting method in the region below our pair-p_T cut $p_T < 0.15$ GeV/c. We also used two methods for the like-sign template distribution:

- ▷ fixed like-sign contribution
- ▷ free like-sign contribution

The former is based on the fact that we should see the same portion of random background in our data. The latter is motivated by the bad χ^2 of the former

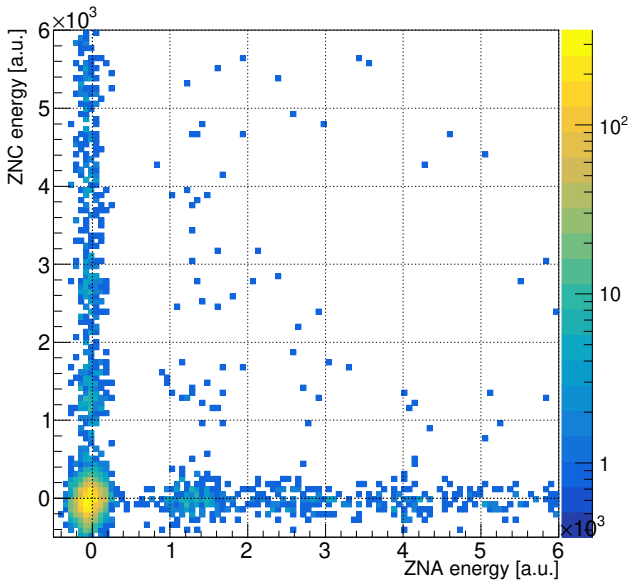

Fig. 4.53: 2D distribution of the energy deposited in the ZN calorimeters. Only track selection required.

one and by allowing more freedom to the fit. As can be seen for example in Fig. 4.55, the free like-sign method provides a better χ^2, moreover, the minimisation procedure removed all like-sign contributions and the tail is fully explained by the incoherent component. Therefore, the free like-sign method provides a higher contribution of incoherent ρ^0 and it was estimated as $(12.2 \pm 0.7(\text{stat}) \pm 0.7(\text{syst}))\%$ compared to $(8.2 \pm 0.4(\text{stat}) \pm 0.4(\text{syst}))\%$ using the fixed like-sign method for the total sample.

These results are summarised in Tab. 4.9 for each ZDC class. As can be seen, classes with forward neutrons have a larger contamination from

Table 4.8: Summary of bin widths and fit ranges that were used for the extraction of incoherent candidates.

Value	Min	Max
Bin width (total, 0n0n)	10 MeV/c	20 MeV/c
Bin width (0nXn, XnXn)	25 MeV/c	50 MeV/c
Fit minimum	0.2 GeV/c	0.3 GeV/c
Fit maximum	0.6 GeV/c	1.0 GeV/c

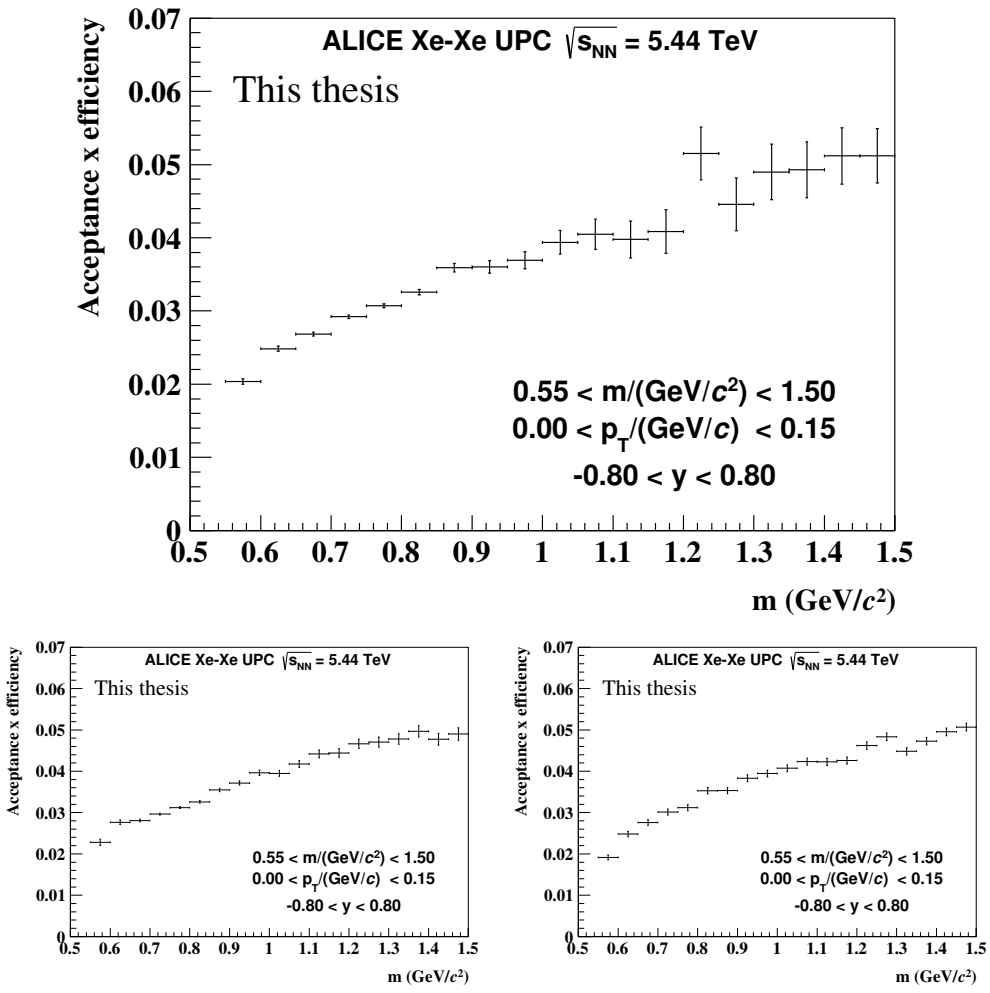

Fig. 4.54: Upper: Acceptance and efficiency obtained from STARlight using a Breit-Wigner with continuum mass distribution. Bottom Left: AxE obtained using only Breit-Wigner mass distribution. Bottom Right: AxE obtained using flat-mass distribution.

incoherent ρ^0. The classes with forward neutrons were merged together into one class 0nXn+Xn0n+XnXn due to the limited amount of data in the XnXn class.

Based on these studies and considering other systematic uncertainties, we can safely choose the mean of both methods and take our correction factor on incoherent ρ^0 in the $p_T < 0.15$ GeV/c region as $(10.2 \pm 2.0(\text{syst}))\%$ in the total sample.

We did the subtraction of incoherent candidates and signal for three dif-

Table 4.9: Summary of contamination by incoherent candidates in our $p_T <$ 0.15 GeV/c region for each ZDC class. Neutrons = 0nXn + Xn0n + XnXn

Class	Fixed LS	Free LS	mean
Total	$(8.2 \pm 0.4 \pm 0.4)\%$	$(12.2 \pm 0.7 \pm 0.7)\%$	$(10.2 \pm 2.0(\text{syst}))\%$
0n0n	$(4.8 \pm 0.3 \pm 0.4)\%$	$(7.3 \pm 0.4 \pm 0.5)\%$	$(6.1 \pm 3.0(\text{syst}))\%$
Neutrons	$(31.5 \pm 2.5 \pm 2.4)\%$	$(40.1 \pm 5.6 \pm 4.2)\%$	$(35.8 \pm 4.3(\text{syst}))\%$

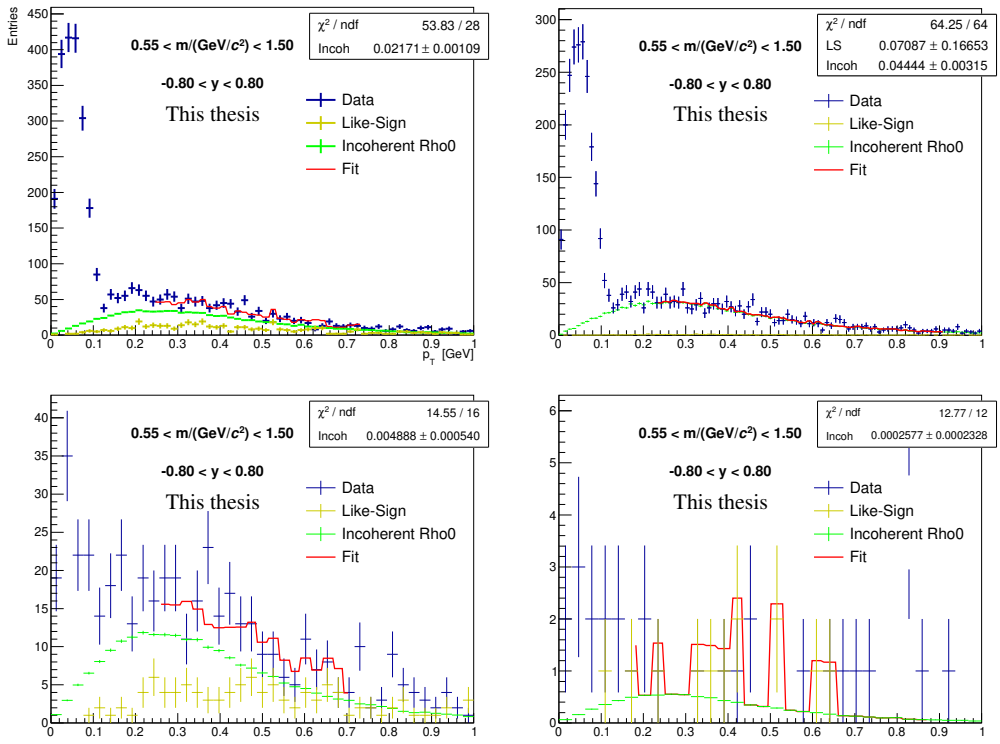

Fig. 4.55: Upper Left: Fit of the pT distribution using a fixed like-sign term. Upper Right: Fit using template like-sign as a free parameter. Bottom Left: Fit of the 0nXn+Xn0n class. Bottom Right: Fit in the XnXn class.

ferent p_T cuts: $p_T < 0.150$ GeV/c, $p_T < 0.175$ GeV/c and $p_T < 0.200$ GeV/c. The overall effect was smaller than 1% which is compatible with the errors obtained for the procedure. Therefore, the $p_T < 0.15$ GeV/c cut was used for the analysis to keep the contamination low.

Pile-up correction

The situation with pile-up in xenon data is similar to the one in the Pb–Pb analysis but slightly easier. The CCUP2 trigger contains only the V0 veto. There are two reasons why events may be lost due to the veto implemented with the V0 trigger:

- Signals in the V0 are produced by a pair of interacting ions different from the pair that creates the ρ^0 vector meson. This process is called pile-up.

- Signals in V0 are produced by an independent electromagnetic interaction of the same pair that creates the ρ^0 vector meson such that at least one of the nuclei is excited. This is called electromagnetic dissociation (EMD). If the nucleus produced charged particles upon de-excitation, these particles may hit V0 and veto the event.

The pile-up correction is treated in a similar way as in the Pb–Pb analysis. The pile-up correction factor was found to be $f_p = 0.89$ and the correction on the EMD effect was found to be $f_{EMD} = 1.027$.

4.3.8 Signal extraction

The general procedure of signal extraction is exactly the same as described above in Sec. 4.2.6.

Both Söding and Ross-Stodolsky functions were used. We perform a set of fits with all parameters set to be free. The ω term C was set to zero as the limited amount of data excluded any attempt to estimate the ω contribution. As can be seen in Fig. 4.56, all fits provide a good χ^2/NDF. The estimated mass of the ρ^0 is in agreement with the PDG value. The width, however, is about 2σ under the PDG value. This is caused by a strong correlation between the width and the background parameter (correlation matrices in the Appendix C.2). Both mass and width were fixed to PDG values.

The $\gamma\gamma \to \mu^+\mu^-$ template mentioned above was used to model the remaining background. This template passed the same selection criteria and was corrected using the same acceptance and efficiency as the signal. The statistical uncertainty of the $\gamma\gamma \to e^+e^-$ cross section in our previous measurement [97] is around 10% and within this precision it agrees with the prediction from STARlight. Changing the normalisation of the $\gamma\gamma \to \mu^+\mu^-$ template in the fit by $\pm 10\%$ produces a -0.2% and $+0.5\%$ systematic uncertainty on the extracted ρ^0 cross section.

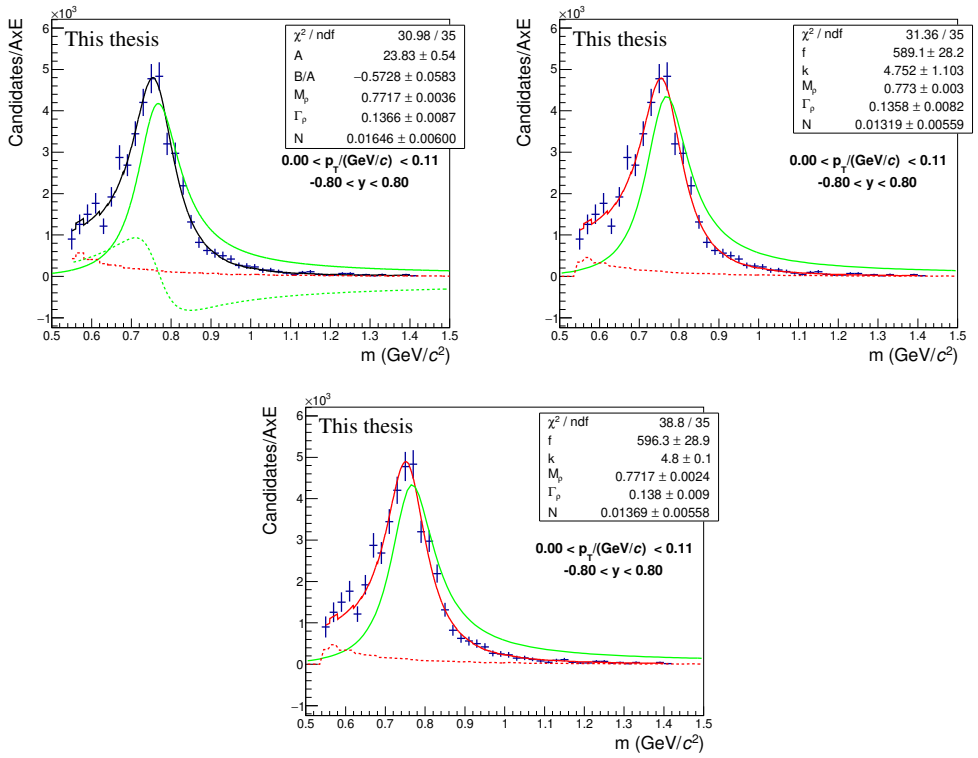

Fig. 4.56: Upper Left: Example of a Söding fit. Upper Right: Ross-Stodolsky fit. Bottom: Ross-Stodolsky 2 fit (another ρ^0 width definition).

For results a χ^2 method was used in all fitting procedures, however a log-likelihood method was used for another check giving the same results within less than 1% difference.

The number of ρ-candidates from the fit was obtained by integration of the BW_ρ part of the Söding function using the standard range ($2m_\pi$,$M_\rho^{PDG} + 5\Gamma_\rho^{PDG}$). The error was computed using the covariance matrix narrowed to the BW parameters, other parameters were set to 0.

For the signal extraction procedure, 1000 fits with randomly generated binning and fit ranges were used that are summarised in Tab. 4.10. The number of candidates N_c was then taken as an average over all fits and its

Table 4.10: Fit ranges and bin widths used for extraction of candidates.

Fit minimum	Fit maximum	Bin width
(0.55–0.65) GeV	(0.9–1.4) GeV	(10–50) MeV

StdDev was taken as the systematic uncertainty of this extraction. The resulting plots used for the estimation of the number of candidates in each sample can be seen in Appendix C.2.

4.3.9 Systematic uncertainties

The uncertainty of the luminosity determination is dominated by the uncertainty of the Glauber MC which in turn is dominated by the limited knowledge of the shape parameters of xenon, and results into a ±10.7% contribution.

A Ross-Stodolsky function Eq.(3.7) is used as an alternative model. This model yields cross sections larger by 3.5% than those obtained from the Söding model. This difference is considered as a systematic uncertainty.

The uncertainty on the track selection is estimated by changing the selection criteria within reasonable values and repeating the full analysis. The number of TPC points per track was varied in the range 50-90. The analysis was also repeated using the Geometrical cut

```
AliESDtrackCuts::SetCutGeoNcrNcl(3.,130.,1.5,0.85,0.7)
```

that removed specific areas of TPC affected by charge distortions and was suggested by some experts. The uncertainty corresponds to the full variation of the results and amounts to ±3.0%. Likewise for the uncertainty when matching track segments in the ITS to their counterparts in the TPC. This uncertainty amounts to 4%.

The uncertainty on the acceptance and efficiency to reconstruct the ρ^0 vector meson is estimated from the full variation of the results when using the two different MC samples (Breit-Wigner with continuum and pure Breit-Wigner) as discussed above. The flat-mass MC did not reproduce data well, therefore it was not taken into account. The difference after the full signal extraction procedure yields ±0.5%. (Note: the difference between continuum and flat-mass is about 6%)

The fit to extract the incoherent contribution is repeated using different lower and upper limits, as well as bin widths as was discussed above. The procedure produced a 2.0% systematic uncertainty.

Vertex cut: As was shown above, there is a small discrepancy between data and MC above 10 cm from the center of IP that motivates a 10 cm cut along z-axis. The difference in final cross section between using and not using this cut was found to be ±1.5% and it was taken as a systematic uncertainty.

SPD efficiencies: Using the chip-matching procedure, we found about 2% of events are excluded in our MC sample. We can consider this number as

Table 4.11: Summary of the systematic uncertainties for the measured cross section. See text for details.

Source	Uncertainty
Variations to the fit procedure	$\pm 2.5\%$
Ross–Stodolsky fit model	$+3.5\%$
Acceptance and efficiency	$\pm 0.5\%$
Track selection	$\pm 3.0\%$
Track ITS–TPC matching	$\pm 4.0\%$
SPD trigger-to-track matching	$\pm 2.0\%$
TOF trigger efficiencies	$\pm 2.8\%$
Vertex selection	$\pm 1.5\%$
Incoherent contribution	$\pm 2.0\%$
Pile-up	$\pm 1.0\%$
Muon background ($\gamma\gamma \to \mu^+\mu^-$)	$^{+(0.5)}_{-(0.2)}\%$
Electromagnetic dissociation	$\pm 0.2\%$
Luminosity	$\pm 10.7\%$
Total	$^{+(13.3)}_{-(12.8)}\ \%$

a systematic uncertainty as the chip-matching procedure should not remove any MC events and this 2% disagreement probably originated in the bad SPD-efficiency description.

TOF efficiencies: The difference in AxE using the LHC17k2 period and LHC20f13 period that includes TOF efficiencies maps produced 2.8% difference that is included as a systematic uncertainty.

Background: The statistical uncertainty of the $\gamma\gamma \to e^+e^-$ cross section in our previous measurement [97] is around 10% and within this precision it agrees with the prediction from STARlight. Changing the normalisation of the $\gamma\gamma \to \mu^+\mu^-$ template in the fit by $\pm 10\%$ produces a -0.2% and $+0.5\%$ systematic uncertainty on the extracted ρ^0 cross section.

Electromagnetic dissociation producing the beam-rapidity neutrons is accompanied on occasion by other charged particles. These charged particles, if they hit the V0, may cause the event to be lost. The probability for this to happen is estimated to be $(1.7 \pm 0.2)\%$ using the unbiased sample. The statistical precision of this procedure is taken as a systematic uncertainty ($\pm 0.2\%$).

Table 4.11 enumerates the sources of the systematic uncertainties.

Table 4.12: Estimated number of candidates and its stat. and syst. uncertainty obtained from fits. The total cross section is estimated using Eq. 4.8

Used AxE model	Söding cand.	stat.	syst.
B-W with continuum	56760	2368	1334
Pure B-W	57010	2385	1520
Flat-mass	54130	2417	1418
Total cross section		131.5 ± 5.6(stat.)	[mb]

4.3.10 B/A ratio

The ratio of non-resonant to resonant pion production can be estimated within reasonable errors only for the full sample. As can be seen from Fig. C.3, the value obtained from fits is $|B/A| = (0.61 \pm 0.04$ (stat.) $\pm$ 0.03 (syst.)) $(\mathrm{GeV}/c^2)^{-\frac{1}{2}}$ using the Breit-Wigner with continuum AxE and $|B/A| = (0.56 \pm 0.04$ (stat.) $\pm$ 0.04 (syst.)) $(\mathrm{GeV}/c^2)^{-\frac{1}{2}}$ using the pure B-W AxE. The quoted systematic uncertainty is the uncertainty of various fit conditions. Both values are compatible within their systematic errors and we will use an average of both as the measured value: $|B/A| = (0.58 \pm 0.04$ (stat.) ± 0.03 (syst.)) $(\mathrm{GeV}/c^2)^{-\frac{1}{2}}$.

4.3.11 Cross section

The total cross section in Tab. 4.12 is estimated using the equation:

$$\frac{\mathrm{d}\sigma}{\mathrm{d}y} = \frac{N_c \cdot f_{inc} \cdot f_{EMD}}{f_p \cdot \Delta y \cdot L}, \tag{4.8}$$

where N_c is the number of the Söding candidates from Table 4.12 , $L = 279.5$ mb^{-1} luminosity of the sample, $\Delta y = 1.6$ the width of the rapidity bin, the $f_p = 0.89$ pile-up factor, the $f_{EMD} = 1.027$ correction on EMD, and $f_{inc} = 0.898$ the correction on incoherent ρ^0.

Figure 4.57 shows the cross section for the coherent photoproduction of ρ^0 vector mesons in Xe–Xe UPCs at midrapidity. Data are compared to theoretical models. The cross sections are reported numerically in Table 4.12.

4.3.12 Fraction in neutron classes

The fraction of the cross section in forward neutron classes is computed from the number of events that were corrected on migration and pile-up effects described above. The values are summarised in Tab. 4.13. The measured values are also compared with the prediction from the $\mathbf{n}^{\mathbf{O}}_{\mathbf{O}}\mathbf{n}$ MC [60].

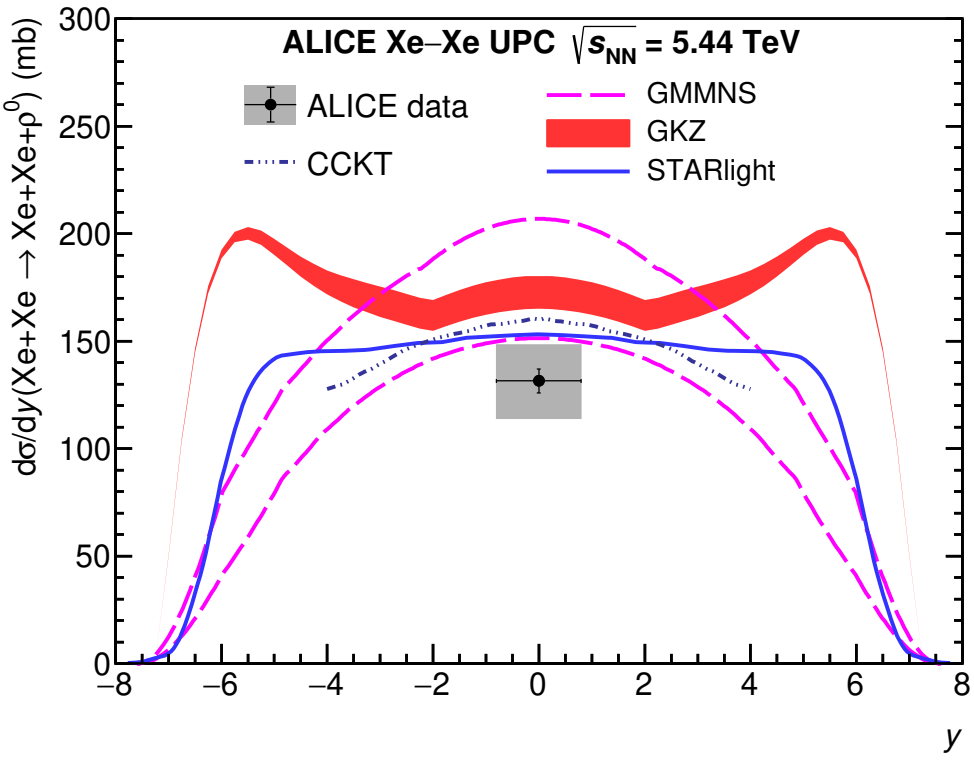

Fig. 4.57: Measured total cross section and its comparison to models. Taken from [103].

4.3.13 Dependence on the atomic mass number

The measurement of the UPC coherent cross section at midrapdities for Pb–Pb [90] and for Xe–Xe [103] has been converted into a γA measurement by dividing the cross sections by two times the corresponding photon fluxes of 59 (Xe) and 128 (Pb). A flux uncertainty of 2% is considered, which is uncorrelated between both nuclei (because it mainly originates in the knowledge of the nuclear geometry). The uncertainties coming from the Ross-Stodolsky fit model and from the ITS-TPC matching are correlated between Xe and Pb. The rest of the uncertainties are uncorrelated and considered when performing the fit.

The γA cross section values are then

- Pb: (2.10 ± 0.15) mb.
- Xe: (1.11 ± 0.14) mb.

The centre-of-mass energy is slightly different in both systems, but the

Table 4.13: Fraction of the cross section in each one of the classes defined by the presence or absence of beam-rapidity neutrons compared with the predictions from the $\mathbf{n^{O}_{O}n}$ model [60]. The first uncertainty is statistical, the second comes from the variations in the ZNA and ZNC pile-up factors and efficiencies, while the third comes from the variation in the number of events which is dominated by the subtraction of the incoherent contribution. The use of $\pm$ or $\mp$ reflects the correlation between the classes. Taken from [103]

Class	Measured fraction	$\mathbf{n^{O}_{O}n}$ prediction
0n0n	$(90.46 \pm 0.70 \pm 0.17 \mp 0.68)\%$	92.4%
0nXn+Xn0n	$(8.48 \pm 0.66 \mp 0.13 \pm 0.64)\%$	6.9%
XnXn	$(1.07 \pm 0.25 \mp 0.04 \pm 0.07)\%$	0.7%

.

cross section is expected to change around 1%, well within the uncertainties, so both energies are considered to be the same: 65 GeV.

These cross sections have been fit to a power law model using also the cross section measured by H1 at this energy [74]: (11.8 ± 0.9) μb. The fit is shown in Fig. 4.58. It has a $\chi^2 = 1.6$ (for one degree of freedom). The parameters are $\sigma_0 = 0.0117 \pm 0.0009$ and $\alpha = 0.962 \pm 0.019$. Varying the flux by $\pm 2\%$ produces a change in the slope of 0.005. The correlation between them is -0.78. The fit is compared with three generic expectations and two models.

4.3.14 Discussion

Cross section The cross section for the coherent photoproduction of ρ^0 vector mesons in ultra-peripheral Xe–Xe collisions at $\sqrt{s_{\mathrm{NN}}} = 5.44$ TeV measured at midrapidity is

$$\frac{\mathrm{d}\sigma}{\mathrm{d}y} = (131.5 \pm 5.6\ (\mathrm{stat.})^{+17.5}_{-16.9}\ (\mathrm{syst.}))\ \mathrm{mb}. \tag{4.9}$$

The main systematic uncertainty comes from the luminosity measurement. Its uncertainty is caused by the extremely short period of data taking in xenon runs which did not allow for a Van der Meer scan to measure the luminosity more precisely.

At midrapidity, all models are relatively close to one another and overestimate the data. The lower band of GMMNS as well as the STARlight and CCKT predictions are slightly more than one standard deviation above the

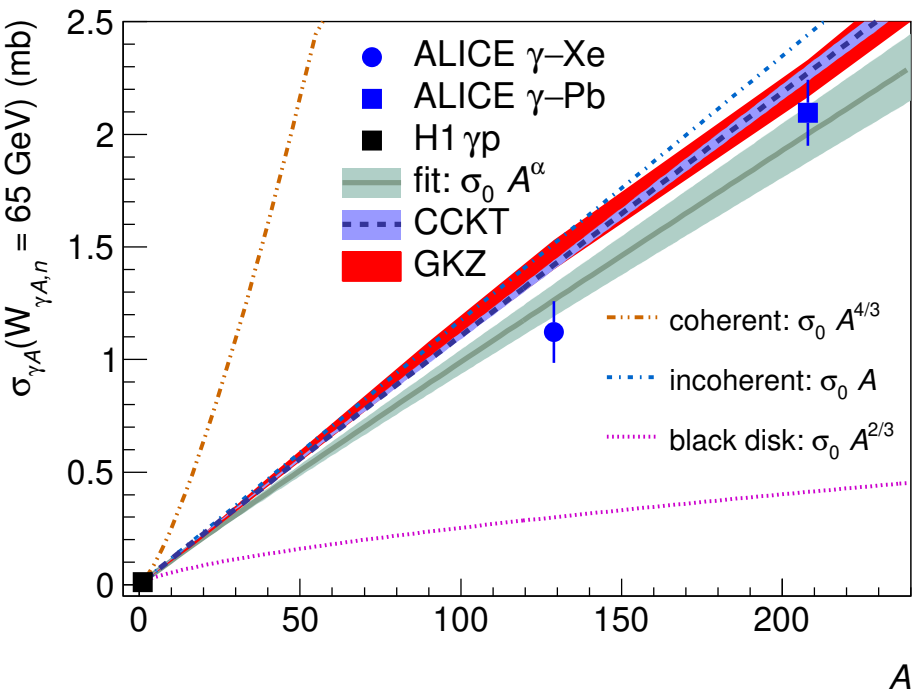

Fig. 4.58: Dependence of the γA cross section on the atomic mass number. Taken from [103].

data. Only the upper band of GMMNS is disfavoured by more than three standard deviations.

$|B/A|$ ratio The ratio of non-resonant to resonant pion production $|B/A|$ was measured to be $|B/A| = (0.58 \pm 0.04\ (\text{stat.}) \pm 0.03\ (\text{syst.}))\ (\text{GeV}/c^2)^{-\frac{1}{2}}$. The main uncertainty comes from the correction for acceptance and efficiency, closely followed by variations from the signal extraction procedure. This value is consistent with those obtained in Pb–Pb UPCs at $\sqrt{s_{\text{NN}}} = 2.76$ TeV [67] and $\sqrt{s_{\text{NN}}} = 5.02$ TeV [90], namely $|B/A| = (0.50 \pm 0.04(\text{stat.}) \pm^{0.10}_{0.04}$ $(\text{syst.}))(\text{GeV/c}^2)^{-\frac{1}{2}}$ and $|B/A| = (0.57 \pm 0.01\ (\text{stat.}) \pm 0.02\ (\text{syst.}))(\text{GeV}/c^2)^{-\frac{1}{2}}$, respectively. The corresponding ratio in coherent Au–Au UPCs measured by STAR at $\sqrt{s_{\text{NN}}} = 200$ GeV is $(0.79 \pm 0.01\ (\text{stat.}) \pm 0.08\ (\text{syst.}))\ (\text{GeV}/c^2)^{-\frac{1}{2}}$ [64]. The CMS Collaboration measured $(0.50 \pm 0.06\ (\text{stat.}))\ (\text{GeV}/c^2)^{-\frac{1}{2}}$ in p–Pb UPCs at $\sqrt{s_{\text{NN}}} = 5.02$ TeV [78] for $|t| < 0.5$ GeV^2. The ZEUS Collaboration, using a sample of positron–proton collisions at a centre-of-mass energy of 300 GeV, reports $(0.67 \pm 0.02\ (\text{stat.}) \pm 0.04\ (\text{syst.}))\ (\text{GeV}/c^2)^{-\frac{1}{2}}$ for their full analysed sample, and $\approx 0.8\ (\text{GeV}/c^2)^{-\frac{1}{2}}$ for t values similar to those of

coherent ρ^0 production in Pb–Pb UPCs [77].

Fraction of cross section in neutron classes The fraction of the cross section in each one of the classes defined by the presence or absence of beam-rapidity neutrons is shown in Tab. 4.13, where the measurement is also compared with the prediction from the $\mathbf{n^0_0n}$ MC [60].

The agreement of the model with data is at the level of one standard deviation. Similar description of the corresponding cross sections was observed in Pb–Pb UPCs at $\sqrt{s_{\mathrm{NN}}} = 5.02$ TeV [90] suggesting that the emission of neutrons at beam-rapidity is well understood for the coherent photoproduction of ρ^0 vector mesons off Pb and Xe nuclei.

A dependence The dependence of Pb–Pb and Xe–Xe cross sections on A was shown in Fig. 4.58. The fit is compared with three generic expectations having different dependence on A resulting in slopes α of 4/3, 1, and 2/3 for full coherence disregarding any other dynamical effect, for a total incoherent behaviour, and for the black-disc limit, respectively.

The slope found in data is significantly different from 4/3 signalling important shadowing effects. The closeness of data to a slope of 1 does not imply incoherent behaviour, but it is just a coincidence produced by the large shadowing suppression. The black-disc limit seems to be quite distant at this energy of $W_{\gamma A} = 65$ GeV.

Fitting to the predictions of the Gribov–Glauber approach (GKZ [52, 53]) and of the colour dipole model with subnucleon degrees of freedom (CCKT [55, 104]) yields slopes of (0.985 ± 0.007) and (0.984 ± 0.003), respectively. Both slopes are in good agreement with that found in data. This was expected given that both approaches give a reasonable description of the different available data.

Chapter 5

Conclusion

The LHC can provide ultra-peripheral collisions at the highest energy nowadays. The ALICE experiment is the best detector at the LHC to study soft processes, as coherent ρ^0 photoproduction, which can provide important information about the gluon distribution in the target nuclei.

This thesis is a collection of my results at ALICE. The presented results on coherent ρ^0 photoproduction in Pb–Pb and Xe–Xe ultra-peripheral collisions were published in JHEP [90] and PLB [103].

In particular, the new cut (SPD trigger-track matching) introduced in this work shed a new light on the pile-up caused by the UPC trigger. Also the extensive work on samples with forward neutrons, the correction on EMD pile-up, and migration of events between these samples is completely new and it is already used in other UPC analysis on J/Ψ production.

The measured cross section of coherent ρ^0 photoproduction extends the ALICE results from Run 1 measured at a lower energy and completed the picture. Both measurements have good precision and confirmed that the cross section predicted by various models including nuclear shadowing effects is well understood.

There are two interesting ways which can be further explored. The first one is to move to higher energy of the collision which can provide important answers to saturation effects. However, this could be achieved only by a new generation of accelerators or by a new detector that will be able to study this process at forward rapidity. The second way is to increase the amount of available data. That will open several doors for possible measurements. Firstly, the transverse momentum spectra can be examined in more detail. It will enable to measure the cross section of the incoherent ρ^0 photoproduction and the spectrum can be transformed into an impact-parameter distribution of the target as shown by STAR at lower energy [64]. Secondly, other resonances can be studied and their cross section can be measured. However,

at least 10 times larger data sample will be necessary to study ω and higher mass states that are already visible in Pb–Pb data. This could be achieved in the near future with the ALICE upgrade for Run 3 and Run 4.

Bibliography

[1] Oliver Sim Brüning et al. *LHC Design Report*. CERN Yellow Reports: Monographs. Geneva: CERN, 2004. DOI: 10.5170/CERN-2004-003-V-1. URL: https://cds.cern.ch/record/782076.

[2] G. Aad et al. "Observation of a new particle in the search for the Standard Model Higgs boson with the ATLAS detector at the LHC". In: *Physics Letters B* 716.1 (Sept. 2012), pp. 1–29. ISSN: 0370-2693. DOI: 10.1016/j.physletb.2012.08.020. URL: http://dx.doi.org/10.1016/j.physletb.2012.08.020.

[3] S. Chatrchyan et al. "Observation of a new boson at a mass of 125 GeV with the CMS experiment at the LHC". In: *Physics Letters B* 716.1 (Sept. 2012), pp. 30–61. ISSN: 0370-2693. DOI: 10.1016/j.physletb.2012.08.021. URL: http://dx.doi.org/10.1016/j.physletb.2012.08.021.

[4] *LEP design report*. Copies shelved as reports in LEP, PS and SPS libraries. Geneva: CERN, 1984. URL: https://cds.cern.ch/record/102083.

[5] "LHC Machine". In: *JINST* 3 (2008). Ed. by Lyndon Evans and Philip Bryant, S08001. DOI: 10.1088/1748-0221/3/08/S08001.

[6] Esma Mobs. "The CERN accelerator complex - 2019. Complexe des accélérateurs du CERN - 2019". In: (July 2019). General Photo. URL: https://cds.cern.ch/record/2684277.

[7] CERN. *Longer term LHC schedule*. 2020. URL: https://lhc-commissioning.web.cern.ch/schedule/LHC-long-term.htm (visited on 05/30/2021).

[8] M. Bajko et al. *Report of the task force on the incident of 19th September 2008 at the LHC*. Tech. rep. Mar. 2009. URL: https://cds.cern.ch/record/1168025/files/LHC-PROJECT-REPORT-1168.pdf (visited on 10/12/2021).

[9] K. Aamodt et al. "The ALICE experiment at the CERN LHC". In: *JINST* 3 (2008), S08002. DOI: 10.1088/1748-0221/3/08/S08002.

[10] Betty Abelev et al. "Performance of the ALICE Experiment at the CERN LHC". In: *Int. J. Mod. Phys.* A29 (2014), p. 1430044. DOI: 10.1142/S0217751X14300440. arXiv: 1402.4476 [nucl-ex].

[11] P Cortese et al. "ALICE: Physics performance report, volume I". In: *J. Phys. G* 30 (2004). Ed. by F Carminati et al., pp. 1517–1763. DOI: 10.1088/0954-3899/30/11/001.

[12] Christian Wolfgang Fabjan et al. "ALICE: Physics performance report, volume II". In: *J. Phys. G* 32 (2006). Ed. by B Alessandro et al., pp. 1295–2040. DOI: 10.1088/0954-3899/32/10/001.

[13] Arturo Tauro. "ALICE Schematics". General Photo. May 2017. URL: https://cds.cern.ch/record/2263642.

[14] Domenico Colella. "ALICE Inner Tracking System Upgrade: Construction and Commissioning". In: *Springer Proc. Phys.* 250 (2020). Ed. by Domenico Elia et al., pp. 485–488. DOI: 10.1007/978-3-030-53448-6_76. arXiv: 1912.12188 [physics.ins-det].

[15] Saikat Biswas. *ALICE TPC upgrade for High-Rate operations*. 2015. arXiv: 1511.04988 [physics.ins-det].

[16] Nicolò Jacazio. *PID performance of the ALICE-TOF detector in Run 2*. 2018. arXiv: 1809.00574 [physics.ins-det].

[17] Abraham Villatoro Tello. "AD, the ALICE diffractive detector". In: *AIP Conf. Proc.* 1819.1 (2017). Ed. by Marcella Capua et al., p. 040020. DOI: 10.1063/1.4977150.

[18] Alla Maevskaya. "Fast Interaction Trigger for the upgrade of the ALICE experiment at CERN: design and performance". In: *EPJ Web of Conferences* 204 (2019). Ed. by S. Bondarenko, V. Burov, and A.Editors Malakhov, p. 11003. ISSN: 2100-014X. DOI: 10.1051/epjconf/201920411003. URL: http://dx.doi.org/10.1051/epjconf/201920411003.

[19] Betty Abelev et al. "Measurement of the Cross Section for Electromagnetic Dissociation with Neutron Emission in Pb-Pb Collisions at $\sqrt{s_{NN}} = 2.76$ TeV". In: *Phys. Rev. Lett.* 109 (2012), p. 252302. DOI: 10.1103/PhysRevLett.109.252302. arXiv: 1203.2436 [nucl-ex].

[20] *Technical Design Report for the Muon Forward Tracker*. Tech. rep. Jan. 2015. URL: https://cds.cern.ch/record/1981898.

[21] P Antonioli, A Kluge, and W Riegler. *Upgrade of the ALICE Readout and Trigger System*. Tech. rep. Sept. 2013. URL: http://cds.cern.ch/record/1603472.

[22] M. Krivda et al. "The ALICE trigger system for LHC Run 3". In: *PoS* TWEPP-17 (2017), p. 149. DOI: 10.22323/1.313.0149. arXiv: 1711.01200 [physics.ins-det].

[23] F. Carminati and A. Morsch. "Simulation in ALICE". In: *eConf* C0303241 (2003), TUMT004. arXiv: physics/0306092.

[24] I. Antcheva et al. "ROOT: A C++ framework for petabyte data storage, statistical analysis and visualization". In: *Comput. Phys. Commun.* 180 (2009), pp. 2499–2512. DOI: 10.1016/j.cpc.2009.08.005. arXiv: 1508.07749 [physics.data-an].

[25] S Bagnasco et al. "AliEn: ALICE environment on the GRID". In: *Journal of Physics: Conference Series* 119.6 (July 2008), p. 062012. DOI: 10.1088/1742-6596/119/6/062012. URL: https://doi.org/10.1088/1742-6596/119/6/062012.

[26] Yan Pei et al. "An Elementary Introduction to Kalman Filtering". In: *Commun. ACM* 62.11 (Oct. 2019), pp. 122–133. ISSN: 0001-0782. DOI: 10.1145/3363294. URL: https://doi.org/10.1145/3363294.

[27] René Brun et al. *GEANT: detector description and simulation tool; March 1994*. CERN Program Library. Long Writeup W5013. Geneva: CERN, 1993. URL: http://cds.cern.ch/record/1073159.

[28] S. Agostinelli et al. "Geant4—a simulation toolkit". In: *Nuclear Instruments and Methods in Physics Research Section A: Accelerators, Spectrometers, Detectors and Associated Equipment* 506.3 (2003), pp. 250–303. ISSN: 0168-9002. DOI: https://doi.org/10.1016/S0168-9002(03)01368-8. URL: https://www.sciencedirect.com/science/article/pii/S0168900203013688.

[29] T.T. Böhlen et al. "The FLUKA Code: Developments and Challenges for High Energy and Medical Applications". In: *Nuclear Data Sheets* 120 (2014), pp. 211–214. ISSN: 0090-3752. DOI: https://doi.org/10.1016/j.nds.2014.07.049. URL: https://www.sciencedirect.com/science/article/pii/S0090375214005018.

[30] Alfredo Ferrari et al. "FLUKA: A multi-particle transport code (Program version 2005)". In: (Oct. 2005). DOI: 10.2172/877507.

[31] CERN. *ALICE O2 Project*. 2018. URL: https://alice-o2-project.web.cern.ch/ (visited on 05/30/2021).

[32] Enrico Fermi. "On the Theory of Collisions between Atoms and Electrically Charged Particles". In: *Electromagnetic Probes of Fundamental Physics* (Sept. 2003). DOI: 10.1142/9789812704214_0026. URL: http://dx.doi.org/10.1142/9789812704214_0026.

[33] David Horák. "Exclusive production of Rho in p-Pb Ultra-Peripheral Collisions". MA thesis. Czech technical University in Prague, 2015. URL: http://physics.fjfi.cvut.cz/publications/ejcf/DP_David_Horak.pdf.

[34] J. G. Contreras and J. D. Tapia Takaki. "Ultra-peripheral heavy-ion collisions at the LHC". In: *Int. J. Mod. Phys.* A30 (2015), p. 1542012. DOI: 10.1142/S0217751X15420129.

[35] J. Adam et al. "Measurement of an Excess in the Yield of J/ψ at Very Low pT in Pb–Pb Collisions at $\sqrt{s_{\mathrm{NN}}} = 2.76$ TeV". In: *Physical Review Letters* 116.22 (June 2016). ISSN: 1079-7114. DOI: 10.1103/physrevlett.116.222301. URL: http://dx.doi.org/10.1103/PhysRevLett.116.222301.

[36] C. F. von Weizsacker. "Radiation emitted in collisions of very fast electrons". In: *Z. Phys.* 88 (1934), pp. 612–625. DOI: 10.1007/BF01333110.

[37] E. J. Williams. "Nature of the high-energy particles of penetrating radiation and status of ionization and radiation formulae". In: *Phys. Rev.* 45 (1934), pp. 729–730. DOI: 10.1103/PhysRev.45.729.

[38] Gerhard Baur et al. "Coherent gamma gamma and gamma-A interactions in very peripheral collisions at relativistic ion colliders". In: *Phys. Rept.* 364 (2002), pp. 359–450. DOI: 10.1016/S0370-1573(01)00101-6. arXiv: hep-ph/0112211.

[39] Anthony J. Baltz, Spencer R. Klein, and Joakim Nystrand. "Coherent vector meson photoproduction with nuclear breakup in relativistic heavy ion collisions". In: *Phys. Rev. Lett.* 89 (2002), p. 012301. DOI: 10.1103/PhysRevLett.89.012301. arXiv: nucl-th/0205031 [nucl-th].

[40] Suraj N. Gupta. "Multiple Bremsstrahlung". In: *Phys. Rev.* 99 (3 Aug. 1955), pp. 1015–1019. DOI: 10.1103/PhysRev.99.1015. URL: https://link.aps.org/doi/10.1103/PhysRev.99.1015.

[41] Mikhail Kzosov. "Approximation of photonuclear interaction cross-sections". In: *European Physical Journal A* 14 (July 2002), pp. 377–392. DOI: 10.1140/epja/i2002-10008-x.

[42] B. L. Berman and S. C. Fultz. "Measurements of the giant dipole resonance with monoenergetic photons". In: *Rev. Mod. Phys.* 47 (1975), pp. 713–761. DOI: 10.1103/RevModPhys.47.713.

[43] I. A. Pshenichnov et al. "Mutual heavy ion dissociation in peripheral collisions at ultrarelativistic energies". In: *Phys. Rev. C* 64 (2001), p. 024903. DOI: 10.1103/PhysRevC.64.024903. arXiv: nucl-th/0101035.

[44] J.J Sakurai. "Theory of strong interactions". In: *Annals of Physics* 11.1 (1960), pp. 1–48. ISSN: 0003-4916. DOI: https://doi.org/10.1016/0003-4916(60)90126-3. URL: https://www.sciencedirect.com/science/article/pii/0003491660901263.

[45] J.J. Sakurai and D. Schildknecht. "Generalized vector dominance and inelastic electron-proton scattering". In: *Physics Letters B* 40.1 (1972), pp. 121–126. ISSN: 0370-2693. DOI: https://doi.org/10.1016/0370-2693(72)90300-0. URL: https://www.sciencedirect.com/science/article/pii/0370269372903000.

[46] Spencer R. Klein and Joakim Nystrand. "Exclusive vector meson production in relativistic heavy ion collisions". In: *Phys. Rev.* C60 (1999), p. 014903. DOI: 10.1103/PhysRevC.60.014903. arXiv: hep-ph/9902259 [hep-ph].

[47] Alfred H. Mueller. "Small x Behavior and Parton Saturation: A QCD Model". In: *Nucl. Phys. B* 335 (1990), pp. 115–137. DOI: 10.1016/0550-3213(90)90173-B.

[48] Nikolai N. Nikolaev and B. G. Zakharov. "Color transparency and scaling properties of nuclear shadowing in deep inelastic scattering". In: *Z. Phys. C* 49 (1991). Ed. by I. M. Khalatnikov and V. P. Mineev, pp. 607–618. DOI: 10.1007/BF01483577.

[49] H. Kowalski, L. Motyka, and G. Watt. "Exclusive diffractive processes at HERA within the dipole picture". In: *Physical Review D* 74.7 (Oct. 2006). ISSN: 1550-2368. DOI: 10.1103/physrevd.74.074016. URL: http://dx.doi.org/10.1103/PhysRevD.74.074016.

[50] Spencer R. Klein et al. "STARlight: A Monte Carlo simulation program for ultra-peripheral collisions of relativistic ions". In: *Comput. Phys. Commun.* 212 (2017), pp. 258–268. DOI: 10.1016/j.cpc.2016.10.016. arXiv: 1607.03838 [hep-ph].

[51] L. Frankfurt et al. "Nuclear shadowing in photoproduction of ρ mesons in ultraperipheral nucleus collisions at RHIC and the LHC". In: *Phys. Lett.* B752 (2016), pp. 51–58. DOI: 10.1016/j.physletb.2015.11.012. arXiv: 1506.07150 [hep-ph].

[52] V. Guzey, E. Kryshen, and M. Zhalov. "Coherent photoproduction of vector mesons in ultraperipheral heavy ion collisions: Update for run 2 at the CERN Large Hadron Collider". In: *Phys. Rev. C* 93.5 (2016), p. 055206. DOI: 10.1103/PhysRevC.93.055206. arXiv: 1602.01456 [nucl-th].

[53] V. Guzey, E. Kryshen, and M. Zhalov. "Photoproduction of light vector mesons in Xe–Xe ultraperipheral collisions at the LHC and the nuclear density of Xe-129". In: *Phys. Lett. B* 782 (2018), pp. 251–255. DOI: 10.1016/j.physletb.2018.05.058. arXiv: 1803.07638 [hep-ph].

[54] J. Cepila, J. G. Contreras, and J. D. Tapia Takaki. "Energy dependence of dissociative J/ψ photoproduction as a signature of gluon saturation at the LHC". In: *Phys. Lett.* B766 (2017), pp. 186–191. DOI: 10.1016/j.physletb.2016.12.063. arXiv: 1608.07559 [hep-ph].

[55] J. Cepila et al. "Mass dependence of vector meson photoproduction off protons and nuclei within the energy-dependent hot-spot model". In: *Nucl. Phys. B* 934 (2018), pp. 330–340. DOI: 10.1016/j.nuclphysb.2018.07.010. arXiv: 1804.05508 [hep-ph].

[56] N. Armesto. "A Simple model for nuclear structure functions at small x in the dipole picture". In: *Eur. Phys. J.* C26 (2002), pp. 35–43. DOI: 10.1007/s10052-002-1021-z. arXiv: hep-ph/0206017 [hep-ph].

[57] V. P. Goncalves and M. V. T. Machado. "Vector Meson Production in Coherent Hadronic Interactions: An update on predictions for RHIC and LHC". In: *Phys. Rev. C* 84 (2011), p. 011902. DOI: 10.1103/PhysRevC.84.011902. arXiv: 1106.3036 [hep-ph].

[58] V. P. Gonçalves et al. "Color dipole predictions for the exclusive vector meson photoproduction in pp , pPb , and PbPb collisions at run 2 LHC energies". In: *Phys. Rev. D* 96.9 (2017), p. 094027. DOI: 10.1103/PhysRevD.96.094027. arXiv: 1710.10070 [hep-ph].

[59] E. Iancu, K. Itakura, and S. Munier. "Saturation and BFKL dynamics in the HERA data at small x". In: *Phys. Lett.* B590 (2004), pp. 199–208. DOI: 10.1016/j.physletb.2004.02.040. arXiv: hep-ph/0310338 [hep-ph].

[60] M. Broz, J. G. Contreras, and J. D. Tapia Takaki. "A generator of forward neutrons for ultra-peripheral collisions: $\mathbf{n}^{\mathbf{O}}_{\mathbf{O}}\mathbf{n}$". In: *Comput. Phys. Commun.* (2020), p. 107181. ISSN: 0010-4655. DOI: https://doi.org/10.1016/j.cpc.2020.107181. arXiv: 1908.08263 [nucl-th].

[61] A. R. Erwin et al. "Evidence for a $\pi\pi$ Resonance in the I = 1, $J = 1$ State". In: *Phys. Rev. Lett.* 6 (1961), pp. 628–630. DOI: 10.1103/PhysRevLett.6.628.

[62] P A Zyla and others (Particle Data Group). "Review of Particle Physics". In: *Prog. Theor. Exp. Phys.* 2020.8 (Aug. 2020). 083C01. ISSN: 2050-3911. DOI: 10.1093/ptep/ptaa104. URL: https://doi.org/10.1093/ptep/ptaa104.

[63] P. Soding. "On the Apparent shift of the rho meson mass in photoproduction". In: *Phys. Lett.* 19 (1966), pp. 702–704. DOI: 10.1016/0031-9163(66)90451-3.

[64] L. Adamczyk et al. "Coherent diffractive photoproduction of ρ^0 mesons on gold nuclei at 200 GeV/nucleon-pair at the Relativistic Heavy Ion Collider". In: *Phys. Rev.* C96 (2017), p. 054904. DOI: 10.1103/PhysRevC.96.054904. arXiv: 1702.07705 [nucl-ex].

[65] Marc H. Ross and Leo Stodolsky. "Photon dissociation model for vector meson photoproduction". In: *Phys. Rev.* 149 (1966), pp. 1172–1181. DOI: 10.1103/PhysRev.149.1172.

[66] M. L. Good and W. D. Walker. "Diffraction disssociation of beam particles". In: *Phys. Rev.* 120 (1960), pp. 1857–1860. DOI: 10.1103/PhysRev.120.1857.

[67] Jaroslav Adam et al. "Coherent ρ^0 photoproduction in ultra-peripheral Pb-Pb collisions at $\sqrt{s_{\mathrm{NN}}} = 2.76$ TeV". In: *JHEP* 09 (2015), p. 095. DOI: 10.1007/JHEP09(2015)095. arXiv: 1503.09177 [nucl-ex].

[68] J. Ballam et al. "Bubble-Chamber Study of Photoproduction by 2.8- and 4.7-GeV Polarized Photons. I. Cross-Section Determinations and Production of ρ^0 and Δ^{++} in the Reaction $\gamma p \to p\pi^+\pi^-$". In: *Phys. Rev. D* 5 (3 Feb. 1972), pp. 545–589. DOI: 10.1103/PhysRevD.5.545. URL: https://link.aps.org/doi/10.1103/PhysRevD.5.545.

[69] W. Struczinski et al. "Study of photoproduction on hydrogen in a streamer chamber with tagged photons for 1.6 GeV $< E_\gamma <$ 6.3 GeV Topological and reaction cross sections". In: *Nucl. Phys. B* 108 (1976), pp. 45–74. DOI: 10.1016/0550-3213(76)90123-1.

[70] J. Ballam et al. "Vector-Meson Production by Polarized Photons at 2.8, 4.7, and 9.3 GeV". In: *Phys. Rev. D* 7 (11 June 1973), pp. 3150–3177. DOI: 10.1103/PhysRevD.7.3150. URL: https://link.aps.org/doi/10.1103/PhysRevD.7.3150.

[71] W. Struczinski et al. "Study of photoproduction on hydrogen in a streamer chamber with tagged photons for 1.6 GeV $< E_\gamma <$ 6.3 GeV Topological and reaction cross sections". In: *Nuclear Physics B* 108.1 (1976), pp. 45–74. ISSN: 0550-3213. DOI: https://doi.org/10.1016/0550-3213(76)90123-1. URL: https://www.sciencedirect.com/science/article/pii/0550321376901231.

[72] R. M. Egloff et al. "Measurements of Elastic ρ- and ϕ-Meson Photoproduction Cross Sections on Protons from 30 to 180 GeV". In: *Phys. Rev. Lett.* 43 (10 Sept. 1979), pp. 657–660. DOI: 10.1103/PhysRevLett.43.657. URL: https://link.aps.org/doi/10.1103/PhysRevLett.43.657.

[73] D. Aston et al. "Photoproduction of ρ^0 and ω on hydrogen at photon energies of 20 to 70 GeV". In: *Nuclear Physics B* 209.1 (1982), pp. 56–76. ISSN: 0550-3213. DOI: https://doi.org/10.1016/0550-3213(82)90102-X. URL: https://www.sciencedirect.com/science/article/pii/055032138290102X.

[74] V. Andreev et al. "Measurement of Exclusive $\pi^+\pi^-$ and ρ^0 Meson Photoproduction at HERA". In: (May 2021). arXiv: 2005.14471 [hep-ex].

[75] S. Aid et al. "Elastic photoproduction of ρ^0 mesons at HERA". In: *Nuclear Physics B* 463.1 (1996), pp. 3–29. ISSN: 0550-3213. DOI: https://doi.org/10.1016/0550-3213(96)00045-4. URL: https://www.sciencedirect.com/science/article/pii/0550321396000454.

[76] M. Derrick et al. "Measurement of elastic ρ^0 photoproduction at HERA". In: *Z. Phys. C* 69 (1995), pp. 39–54. DOI: 10.1007/s002880050004. arXiv: hep-ex/9507011.

[77] J. Breitweg et al. "Elastic and proton dissociative ρ^0 photoproduction at HERA". In: *Eur. Phys. J.* C2 (1998), pp. 247–267. DOI: 10.1007/s100520050136. arXiv: hep-ex/9712020 [hep-ex].

[78] Albert M Sirunyan et al. "Measurement of exclusive $\rho(770)^0$ photoproduction in ultraperipheral pPb collisions at $\sqrt{s_{\mathrm{NN}}} = 5.02$ TeV". In: *Eur. Phys. J.* C79 (2019), p. 702. DOI: 10.1140/epjc/s10052-019-7202-9. arXiv: 1902.01339 [hep-ex].

[79] G. Agakishiev et al. "ρ^0 Photoproduction in AuAu Collisions at $\sqrt{s_{NN}} =$ 62.4 GeV with STAR". In: *Phys. Rev.* C85 (2012), p. 014910. DOI: 10.1103/PhysRevC.85.014910. arXiv: 1107.4630 [nucl-ex].

[80] C. Adler et al. "Coherent ρ^0 production in ultraperipheral heavy ion collisions". In: *Phys. Rev. Lett.* 89 (2002), p. 272302. DOI: 10.1103/PhysRevLett.89.272302. arXiv: nucl-ex/0206004 [nucl-ex].

[81] B. I. Abelev et al. "ρ^0 photoproduction in ultraperipheral relativistic heavy ion collisions at $\sqrt{s_{NN}} = 200$ GeV". In: *Phys. Rev.* C77 (2008), p. 034910. DOI: 10.1103/PhysRevC.77.034910. arXiv: 0712.3320 [nucl-ex].

[82] René Brun et al. "GEANT Detector Description and Simulation Tool". In: (1994). DOI: 10.17181/CERN.MUHF.DMJ1.

[83] Yakov I. Azimov. "Mixing and decays of rho and omega mesons". In: *Eur. Phys. J.* A16 (2003), pp. 209–219. DOI: 10.1140/epja/i2002-10084-x. arXiv: hep-ph/0209153 [hep-ph].

[84] Spencer R. Klein. "Ultra-Peripheral Collisions with gold ions in STAR". In: *PoS* DIS2016 (2016), p. 188. DOI: 10.22323/1.265.0188. arXiv: 1606.02754 [nucl-ex].

[85] B. I. Abelev et al. "Observation of Two-source Interference in the Photoproduction Reaction Au Au —> Au Au rho0". In: *Phys. Rev. Lett.* 102 (2009), p. 112301. DOI: 10.1103/PhysRevLett.102.112301. arXiv: 0812.1063 [nucl-ex].

[86] V. A. Khoze, A. D. Martin, and M. G. Ryskin. "Exclusive vector meson production in heavy ion collisions". In: (2019). arXiv: 1902.08136 [hep-ph].

[87] V. Rebyakova, M. Strikman, and M. Zhalov. "Coherent ρ and J/ψ photoproduction in ultraperipheral processes with electromagnetic dissociation of heavy ions at RHIC and LHC". In: *Phys. Lett.* B710 (2012), pp. 647–653. DOI: 10.1016/j.physletb.2012.03.041. arXiv: 1109.0737 [hep-ph].

[88] Spencer R. Klein and Heikki Mäntysaari. "Imaging the nucleus with high-energy photons". In: *Nature Rev. Phys.* 1.11 (2019), pp. 662–674. DOI: 10.1038/s42254-019-0107-6. arXiv: 1910.10858 [hep-ex].

[89] Nestor Armesto. "Nuclear shadowing". In: *J. Phys. G* 32 (2006), R367–R394. DOI: 10.1088/0954-3899/32/11/R01. arXiv: hep-ph/0604108.

[90] Shreyasi Acharya et al. "Coherent photoproduction of ρ^0 vector mesons in ultra-peripheral Pb-Pb collisions at $\sqrt{s_{NN}} = 5.02$ TeV". In: *JHEP* 06 (2020), p. 035. DOI: 10.1007/JHEP06(2020)035. arXiv: 2002.10897 [nucl-ex].

[91] I. A. Pshenichnov. "Electromagnetic excitation and fragmentation of ultrarelativistic nuclei". In: *Phys. Part. Nucl.* 42 (2011), pp. 215–250. DOI: 10.1134/S1063779611020067.

[92] Uliana Dmitrieva and Igor Pshenichnov. "On the performance of Zero Degree Calorimeters in detecting multinucleon events". In: *Nucl. Instrum. Meth.* A906 (2018), pp. 114–119. DOI: 10.1016/j.nima.2018.07.072. arXiv: 1805.01792 [physics.ins-det].

[93] I.A. Pshenichnov et al. "Particle emission following Coulomb excitation in ultrarelativistic heavy ion collisions". In: *Phys. Rev. C* 60 (1999), p. 044901. DOI: 10.1103/PhysRevC.60.044901. arXiv: nucl-th/9901061.

[94] J.G. Contreras. *Corrections related to EMD applied to the cross section for coherent rho production in Pb–Pb UPC*. Tech. rep. ALICE internal note. Jan. 2020. URL: https://alice-notes.web.cern.ch/node/1021.

[95] Evgeny Kryshen. *Luminosity determination for ultra-peripheral triggers in Pb-Pb at sqrt(sNN) = 5.02 TeV*. Tech. rep. ALICE internal note. Jan. 2017. URL: https://alice-notes.web.cern.ch/node/595.

[96] Constantin Loizides, Jason Kamin, and David d'Enterria. "Improved Monte Carlo Glauber predictions at present and future nuclear colliders". In: *Phys. Rev. C* 97 (2018). [Erratum: Phys.Rev.C 99, 019901 (2019)], p. 054910. DOI: 10.1103/PhysRevC.97.054910. arXiv: 1710.07098 [nucl-ex].

[97] Evgeny Kryshen. "Overview of ALICE results on ultra-peripheral collisions". In: *EPJ Web Conf.* 204 (2019), p. 01011. DOI: 10.1051/epjconf/201920401011.

[98] V. Guzey, M. Strikman, and M. Zhalov. "Disentangling coherent and incoherent quasielastic J/ψ photoproduction on nuclei by neutron tagging in ultraperipheral ion collisions at the LHC". In: *Eur. Phys. J.* C74 (2014), p. 2942. DOI: 10.1140/epjc/s10052-014-2942-z. arXiv: 1312.6486 [hep-ph].

[99] Z. Citron et al. "Future physics opportunities for high-density QCD at the LHC with heavy-ion and proton beams". In: *HL/HE-LHC Workshop: Workshop on the Physics of HL-LHC, and Perspectives at HE-LHC Geneva, Switzerland, June 18-20, 2018*. 2018. arXiv: 1812.06772 [hep-ph].

[100] H. Abramowicz et al. "Exclusive electroproduction of two pions at HERA". In: *Eur. Phys. J.* C72 (2012), p. 1869. DOI: 10.1140/epjc/s10052-012-1869-5. arXiv: 1111.4905 [hep-ex].

[101] V. Andreev et al. *Measurement of Exclusive ρ^0 Meson Photoproduction at HERA*. H1prelim 18-012. 2018.

[102] M. Tanabashi et al. "Review of Particle Physics". In: *Phys. Rev. D* 98.3 (2018), p. 030001. DOI: 10.1103/PhysRevD.98.030001.

[103] S. Acharya et al. "First measurement of coherent ρ^0 photoproduction in ultra-peripheral Xe–Xe collisions at $\sqrt{s_{NN}} = 5.44$ TeV". In: *Physics Letters B* (2021), p. 136481. ISSN: 0370-2693. DOI: https://doi.org/10.1016/j.physletb.2021.136481. URL: https://www.sciencedirect.com/science/article/pii/S0370269321004214.

[104] M. Krelina, V.P. Goncalves, and J. Cepila. "Coherent and incoherent vector meson electroproduction in the future electron-ion colliders: the hot-spot predictions". In: *Nucl. Phys. A* 989 (2019), pp. 187–200. DOI: 10.1016/j.nuclphysa.2019.06.009. arXiv: 1905.06759 [hep-ph].

List of Figures

List of Tables

Appendices

Appendix A

STAR results

Table A.1: The total cross section extrapolated to the full rapidity range for coherent ρ^0 production at $\sqrt{s_{NN}} =$ 62.4 GeV [79] accompanied by nuclear breakup and without breakup, compared with previous measurements at 130 GeV [80] and 200 GeV [81, 64]. The measured cross section, for XnXn events with $|y_{\rho^0}| < 1$, is based on the dataset collected with trigger B. Cross sections for other levels of nuclear excitation, and for the full rapidity range, are calculated with extrapolation factors detailed in the text. Statistical and systematic errors are shown.

Parameter	STAR at $\sqrt{s_{NN}} = 62.4$ GeV coherent ($\|y_{\rho^0}\| < 1$)	STAR at $\sqrt{s_{NN}} = 62.4$ GeV coherent (full rapidity)	STAR at $\sqrt{s_{NN}} = 130$ GeV coherent (full rapidity)	STAR at $\sqrt{s_{NN}} = 200$ GeV coherent (full rapidity)
$\sigma^{\rho^0}_{XnXn}$ (mb)	6.2 ± 0.9 ± 0.8	10.5 ± 1.5 ± 1.6	28.3 ± 2.0 ± 6.3	31.9 ± 1.5 ± 4.5
$\sigma^{\rho^0}_{0nXn}$ (mb)	16.7 ± 2.7 ± 2.	31.8 ± 5.2 ± 3.9	95 ± 60 ± 25	105 ± 5 ± 15
$\sigma^{\rho^0}_{0n0n}$ (mb)	28.5 ± 5.2 ± 4.8	78 ± 14 ± 13	370 ± 170 ± 80	391 ± 18 ± 55
$\sigma^{\rho^0}_{total}$ (mb)	51.5 ± 5.9 ± 5.3	120 ± 15 ± 22	460 ± 220 ± 110	530 ± 19 ± 57

Appendix B

Pb–Pb

B.1 UPC triggers in Pb–Pb

The dedicated UPC trigger elements in LHC15o periods:

- 0VBA = signal in V0A in BB window;
- 0VBC = signal in V0C in BB window;
- 0UBA = signal in ADA in BB window;
- 0UBC = signal in ADC in BB window;
- 0MSL = single muon low threshold;
- 0MUL = unlike sign di-muon low threshold;
- 0STP = SPD topological trigger;
- 0SH1 = 0SM2 = 2 or more pixel or in outer SPD;
- 0OMU = Between 2 and 6 TOF pad triggered;
- 0OM2 = At least 2 TOF pads triggered.

Muon spectrometer triggers:

- CMUP10 = *0VBA *0UBA *0UBC 0MSL;
- CTEST63 = *0VBA *0UBA *0UBC 0MSL;
- CTEST64 = *0VBA *0UBA *0UBC 0MUL.

Central barrel triggers:

- CCUP2 = *0VBA *0VBC 0OM2 0SM2;
- CCUP4 = *0VBA *0VBC 0OMU 0SM2;
- CCUP9 = *0VBA *0VBC *0UBA *0UBC 0STP;
- CCUP8 = *0VBA *0VBC *0UBA *0UBC 0STP 0OMU;
- CCUP10 = *0VBA *0VBC *0UBA *0UBC 0SH1;
- CCUP11 = *0UBA *0UBC 0STP 0OMU;
- CCUP12 = *0UBA *0UBC 0STP;
- CTEST58= *0VBA *0VBC *0UBA *0UBC 0SH1;
- CTEST59= *0VBA *0VBC *0UBA *0UBC 0STP;
- CTEST60= *0VBA *0VBC *0UBA *0UBC 0OM2;
- CTEST61= *0VBA *0VBC *0UBA *0UBC 0OMU.

B.2 Selection criteria

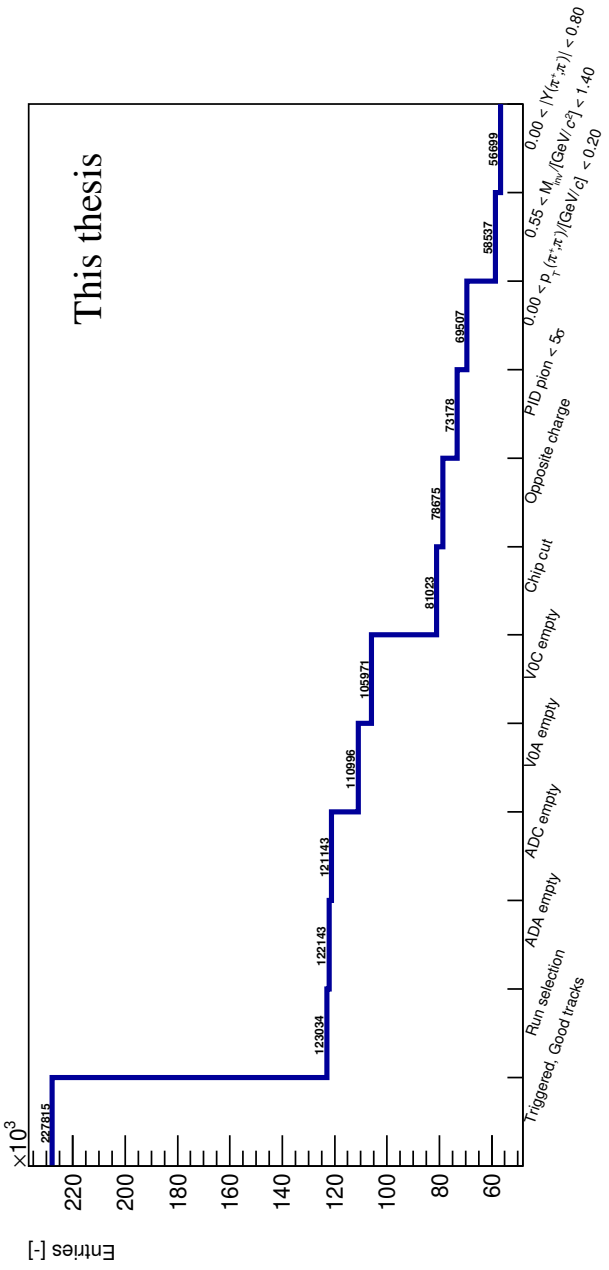

Fig. B.1: The number of events after each selection criterion.

B.3 Code of the SPD trigger-matching

```
Bool_t IsOSTPfired(Int_t *vPhiInner, Int_t *vPhiOuter)
{
  Int_t fired(0);
    for (Int_t i(0); i<10; ++i) {
      for (Int_t j(0); j<2; ++j) {
        const Int_t k(2*i+j);
        fired += ((   vPhiOuter[k]    || vPhiOuter[k+1]       ||
                      vPhiOuter[k+2]      )
                  && (vPhiOuter[k+20] || vPhiOuter[(k+21)%40] ||
                      vPhiOuter[(k+22)%40])
                  && (vPhiInner[i]    || vPhiInner[i+1]       )
                  && (vPhiInner[i+10] || vPhiInner[(i+11)%20]));
          }
    }
  if (fired != 0) return kTRUE;
  else return kFALSE;
}

Int_t SPDInner[20]; for (Int_t i=0; i<20; ++i) SPDInner[i]=0;
Int_t SPDOuter[40]; for (Int_t i=0; i<40; ++i) SPDOuter[i]=0;

SPDInner[ITSModuleInner_T[0]/4]++;
SPDInner[ITSModuleInner_T[1]/4]++;
SPDOuter[(ITSModuleOuter_T[0]-80)/4]++;
SPDOuter[(ITSModuleOuter_T[1]-80)/4]++;

if (!IsOSTPfired(SPDInner,SPDOuter)) return kFALSE;
```

B.4 Pile-up probabilities in detectors

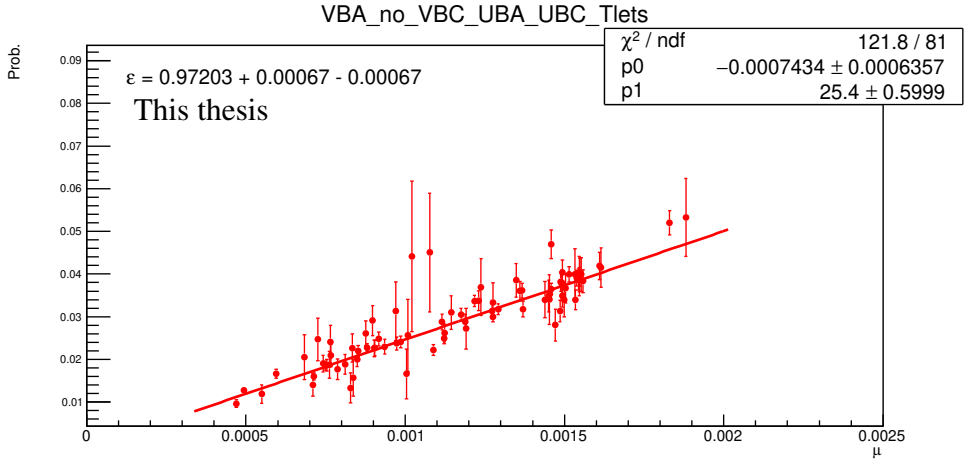

Fig. B.2: Pile-up correction factor for the V0A trigger element (VBA).

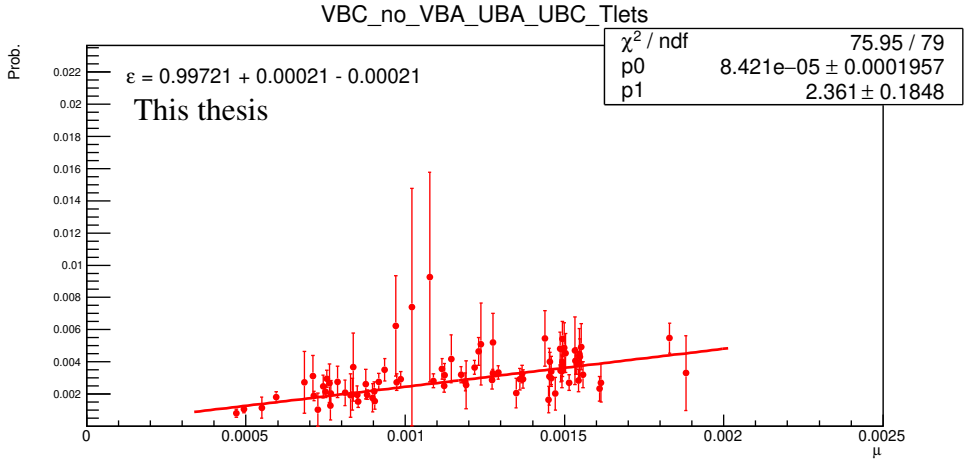

Fig. B.3: Pile-up correction factor for the V0C trigger element (VBC).

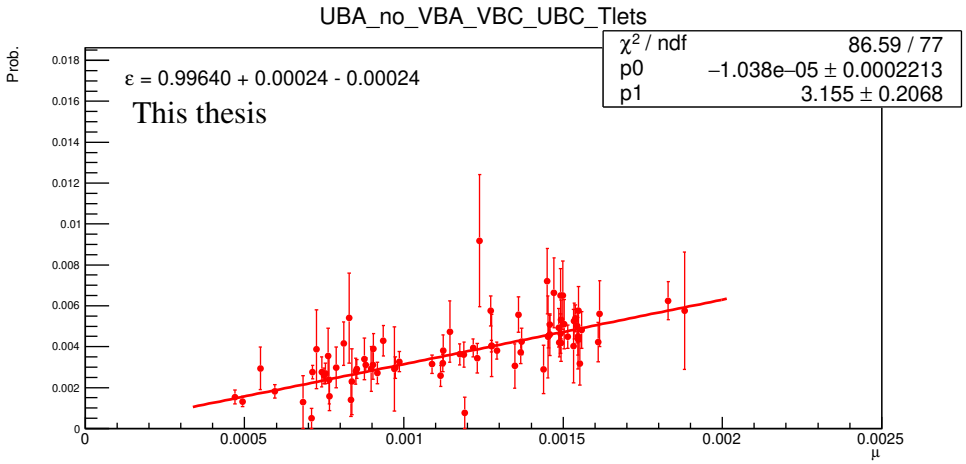

Fig. B.4: Pile-up correction factor for the ADA trigger element (UBA).

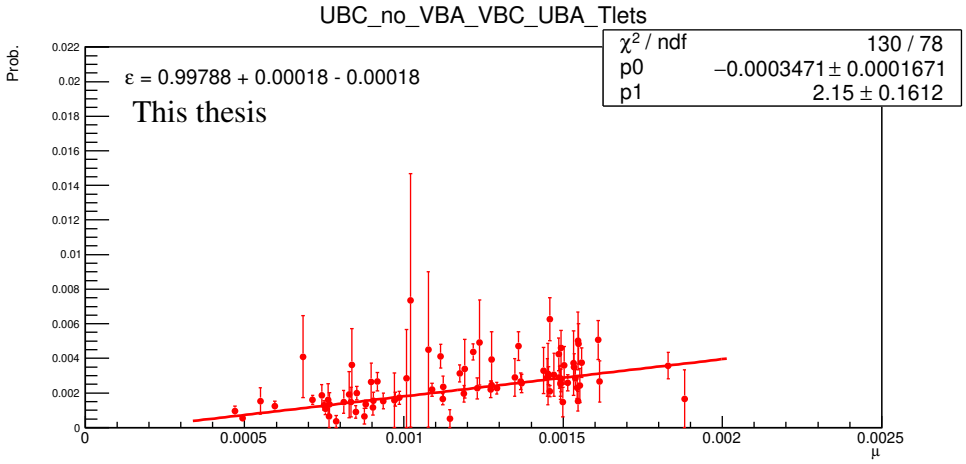

Fig. B.5: Pile-up correction factor for the ADC trigger element (UBC).

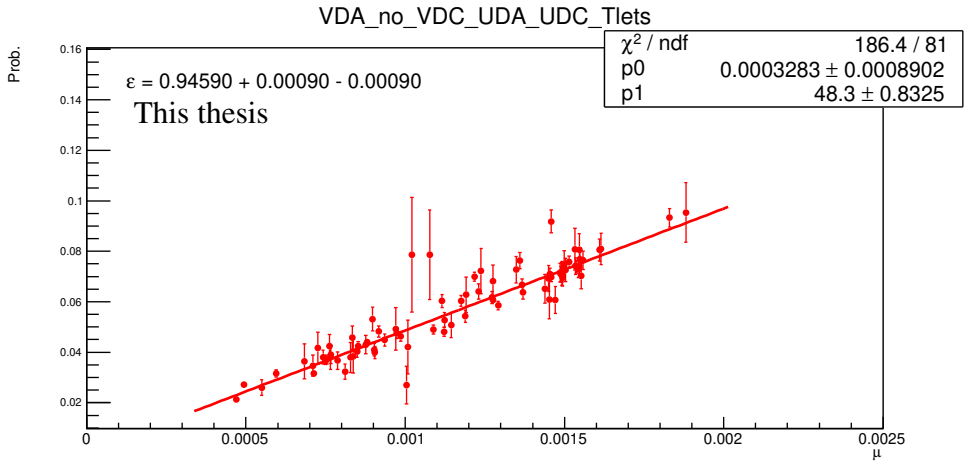

Fig. B.6: Pile-up correction factor for the V0A offline decision (VDA).

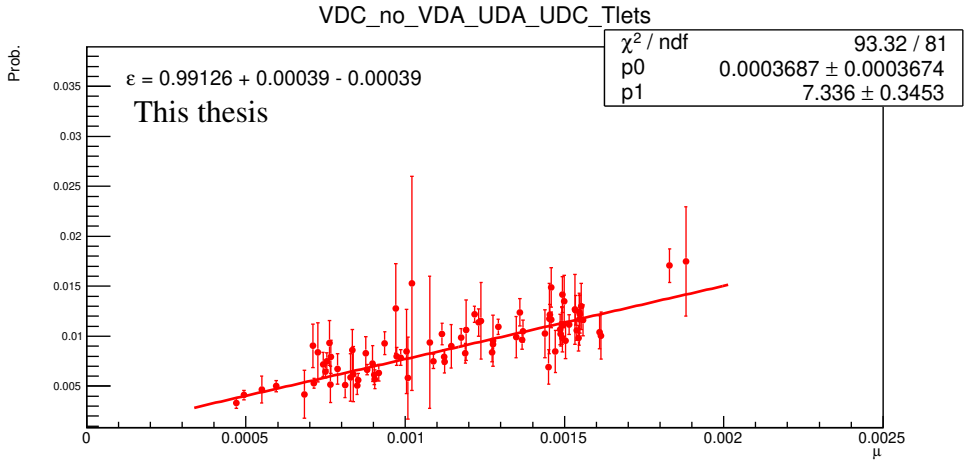

Fig. B.7: Pile-up correction factor for the V0C offline decision (VDC).

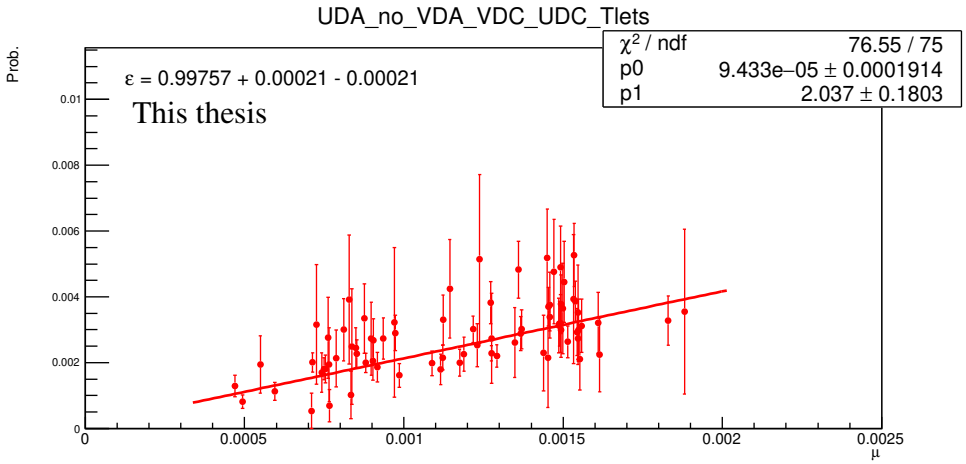

Fig. B.8: Pile-up correction factor for the ADA offline decision (UDA).

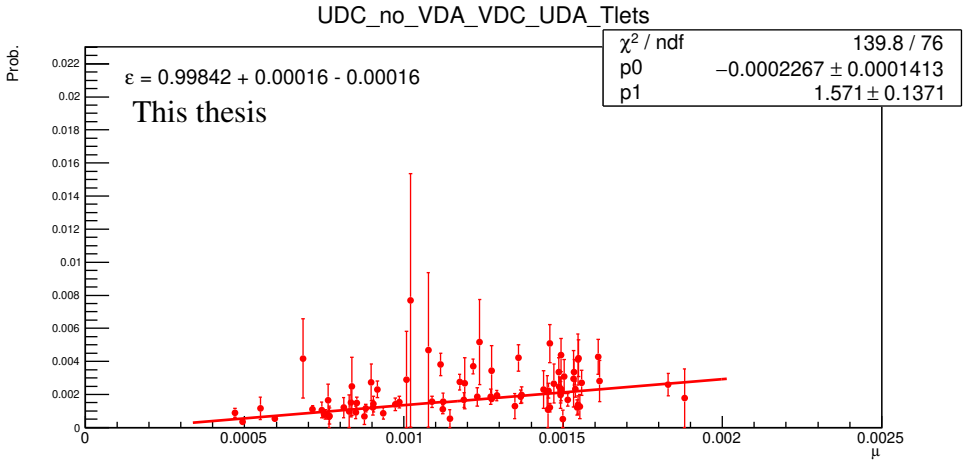

Fig. B.9: Pile-up correction factor for the ADC offline decision (UDC).

B.5 Extracted number of candidates

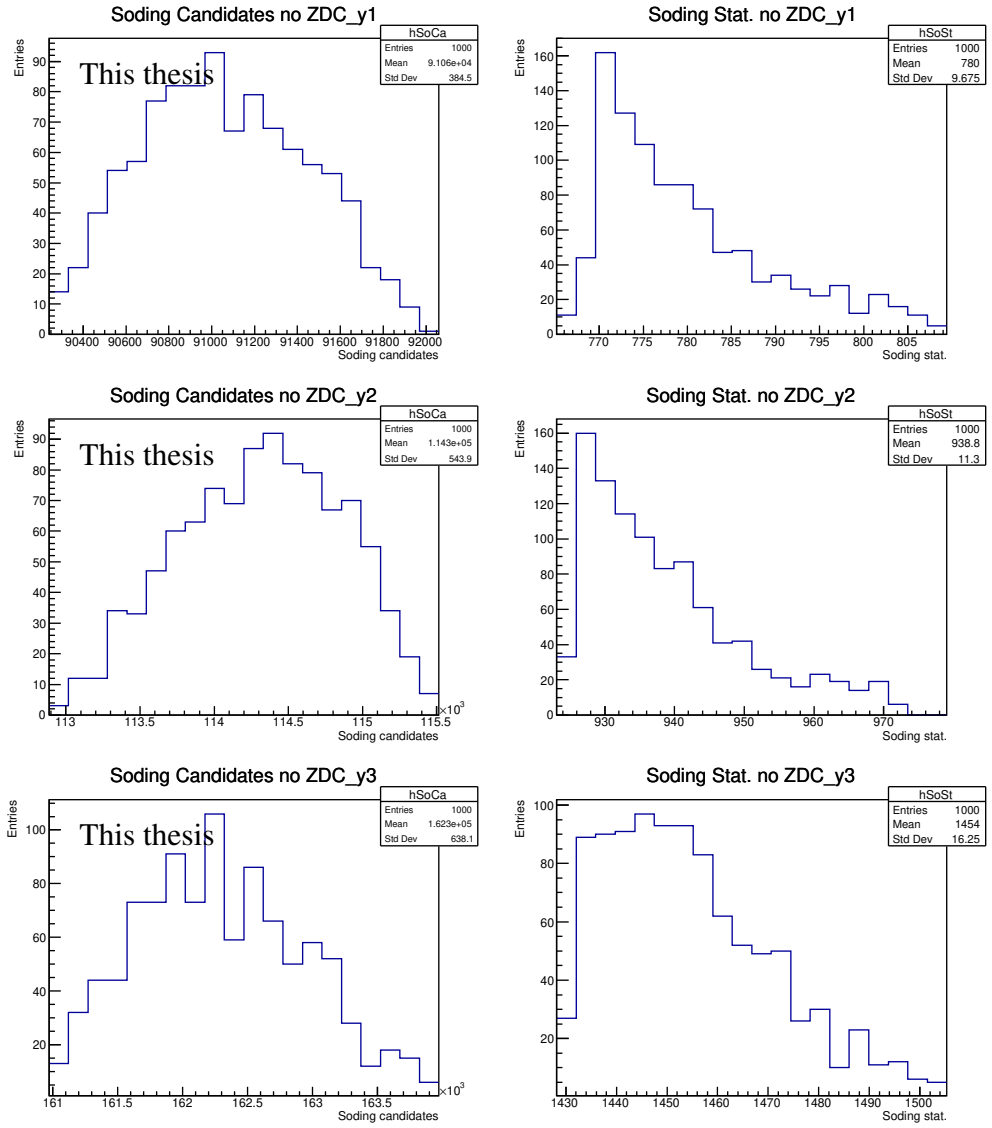

Fig. B.10: Number of candidates and its statistical uncertainty of the Söding in three rapidity bins and total sample.

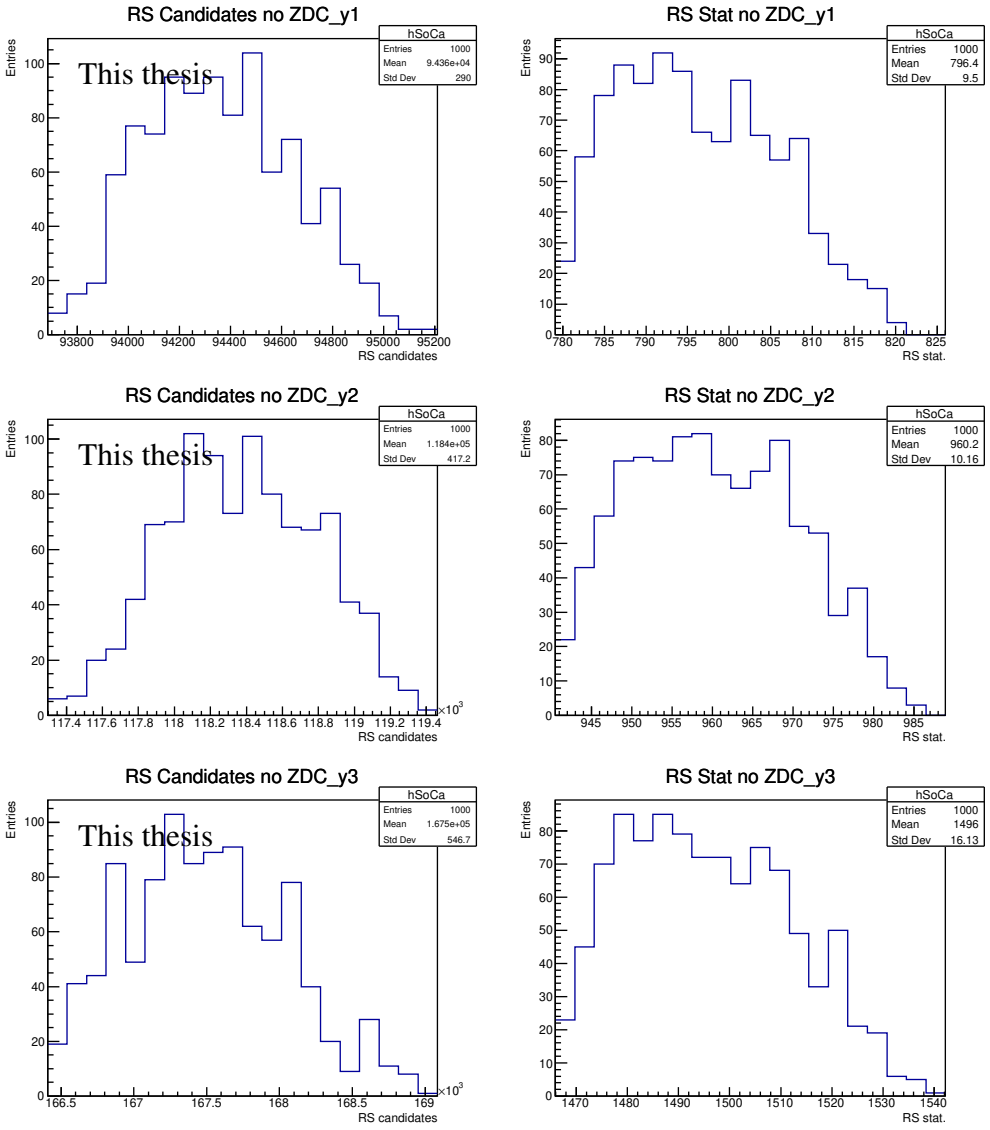

Fig. B.11: Number of candidates and its statistical uncertainty of the Ross-Stodolsky in three rapidity bins and total sample.

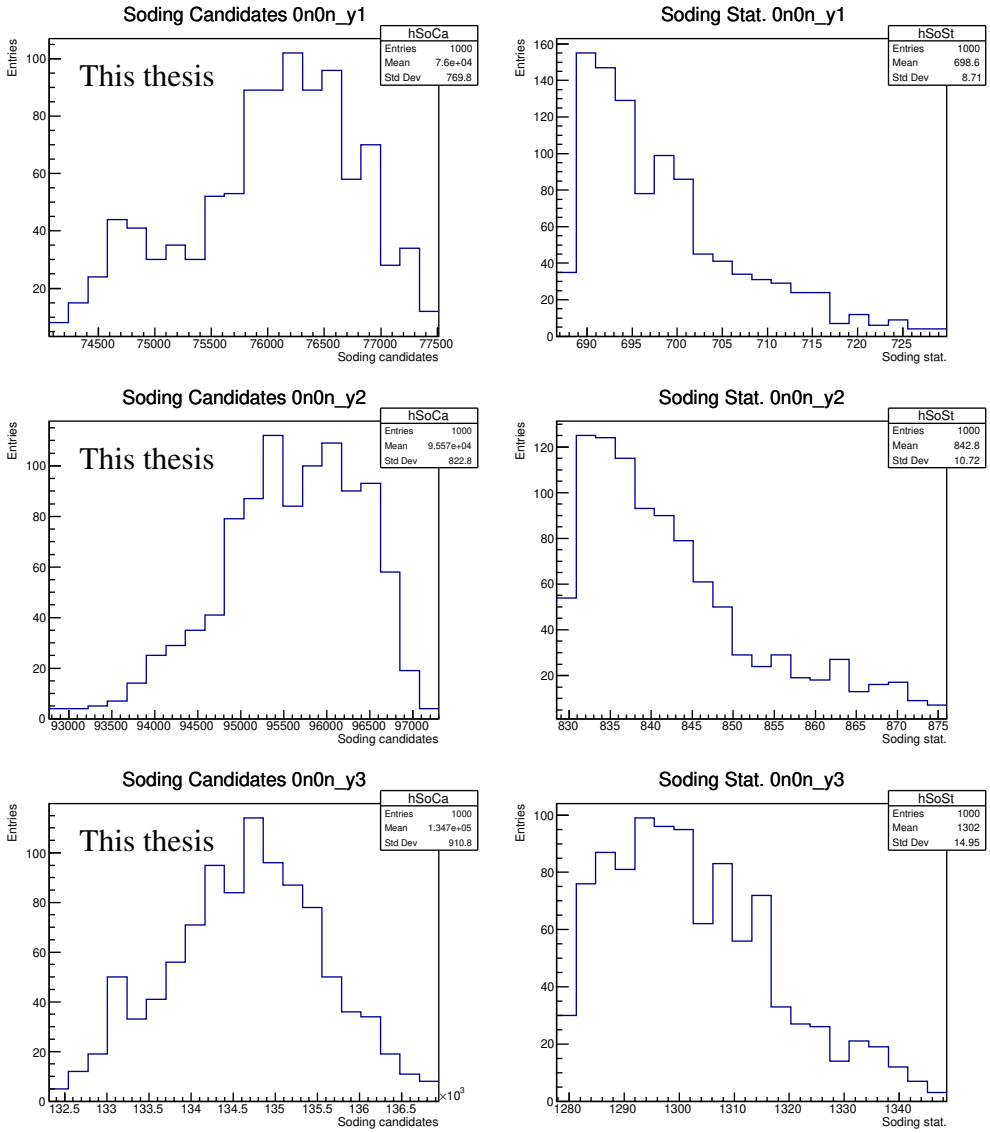

Fig. B.12: Number of candidates and its statistical uncertainty of the Söding in three rapidity bins and 0n0n sample.

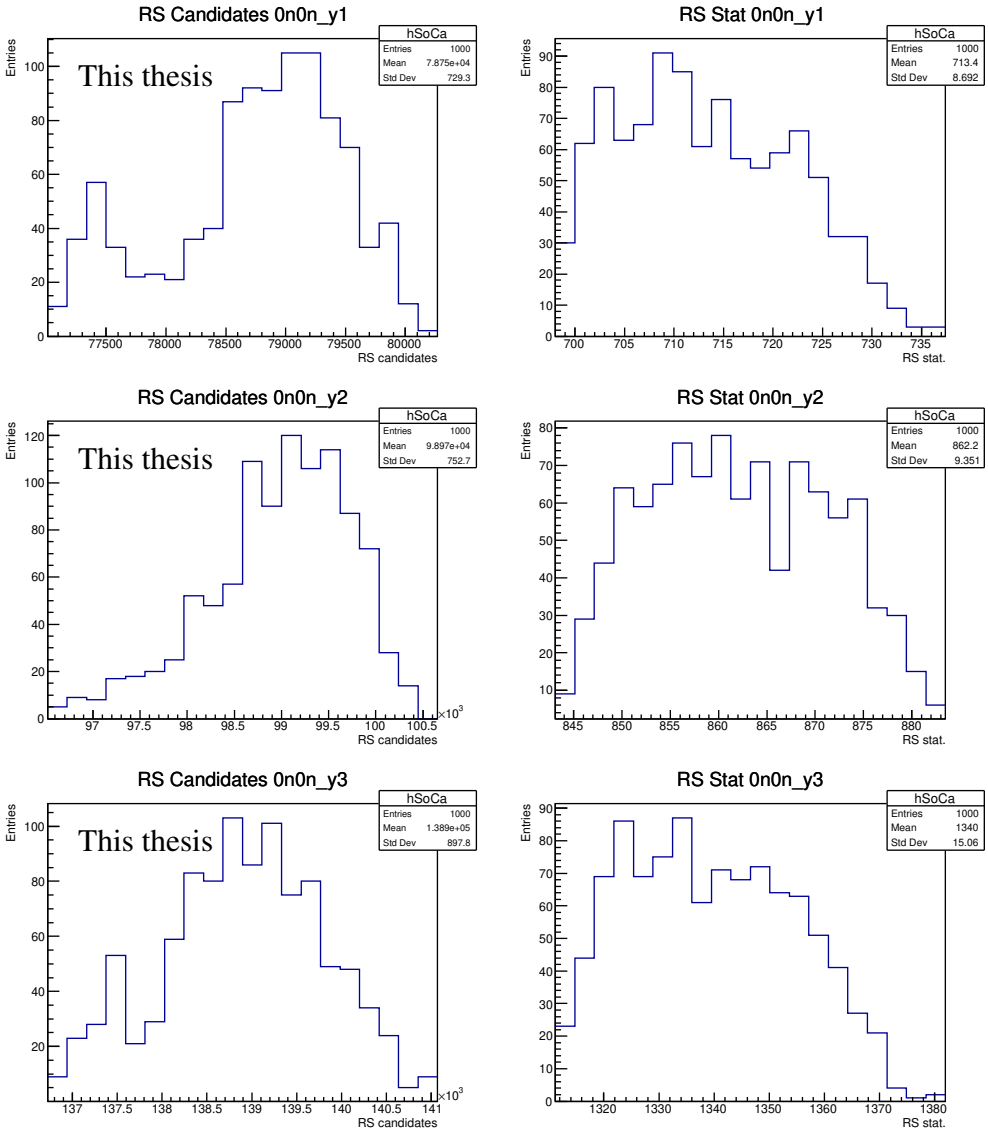

Fig. B.13: Number of candidates and its statistical uncertainty of the Ross-Stodolsky in three rapidity bins and 0n0n sample.

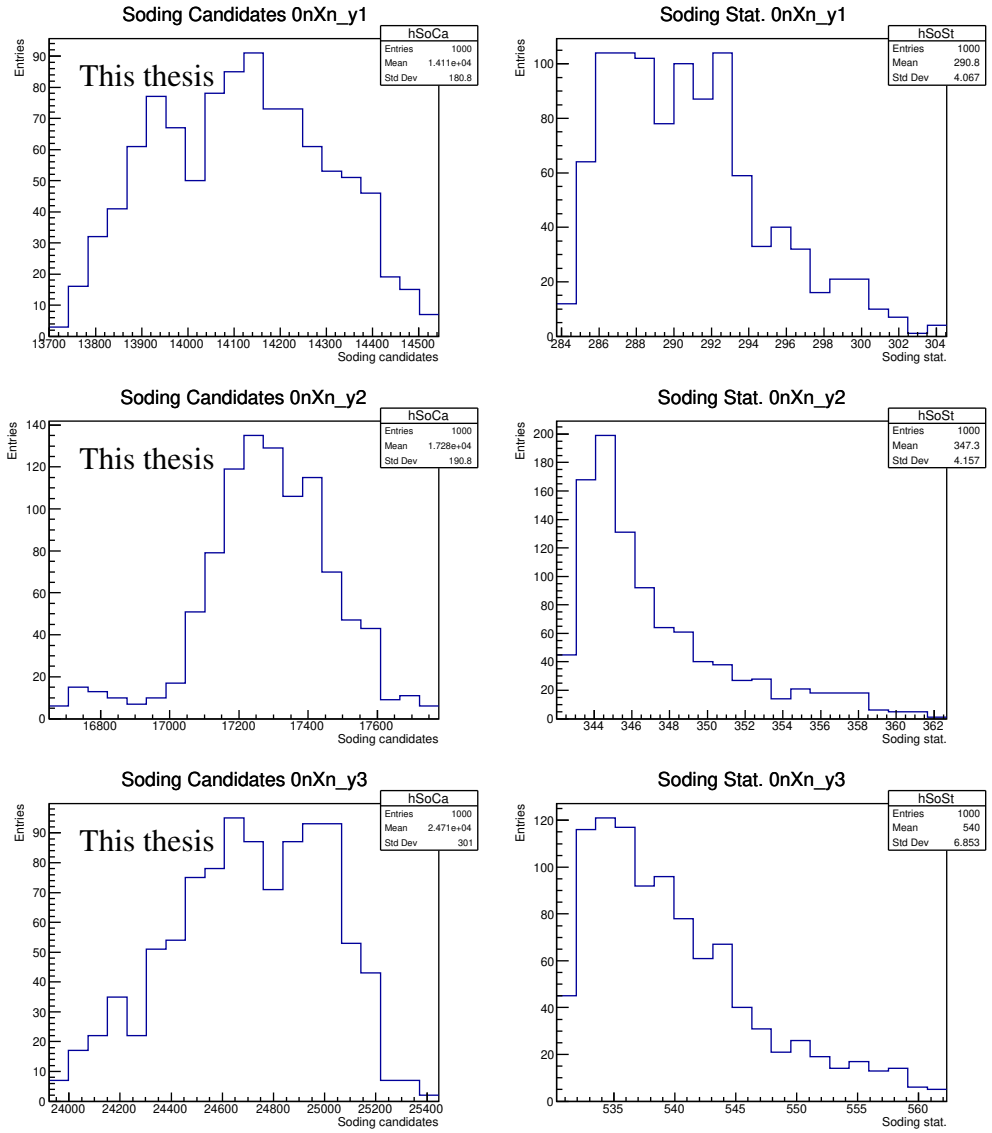

Fig. B.14: Number of candidates and its statistical uncertainty of the Söding in three rapidity bins and 0nXn sample.

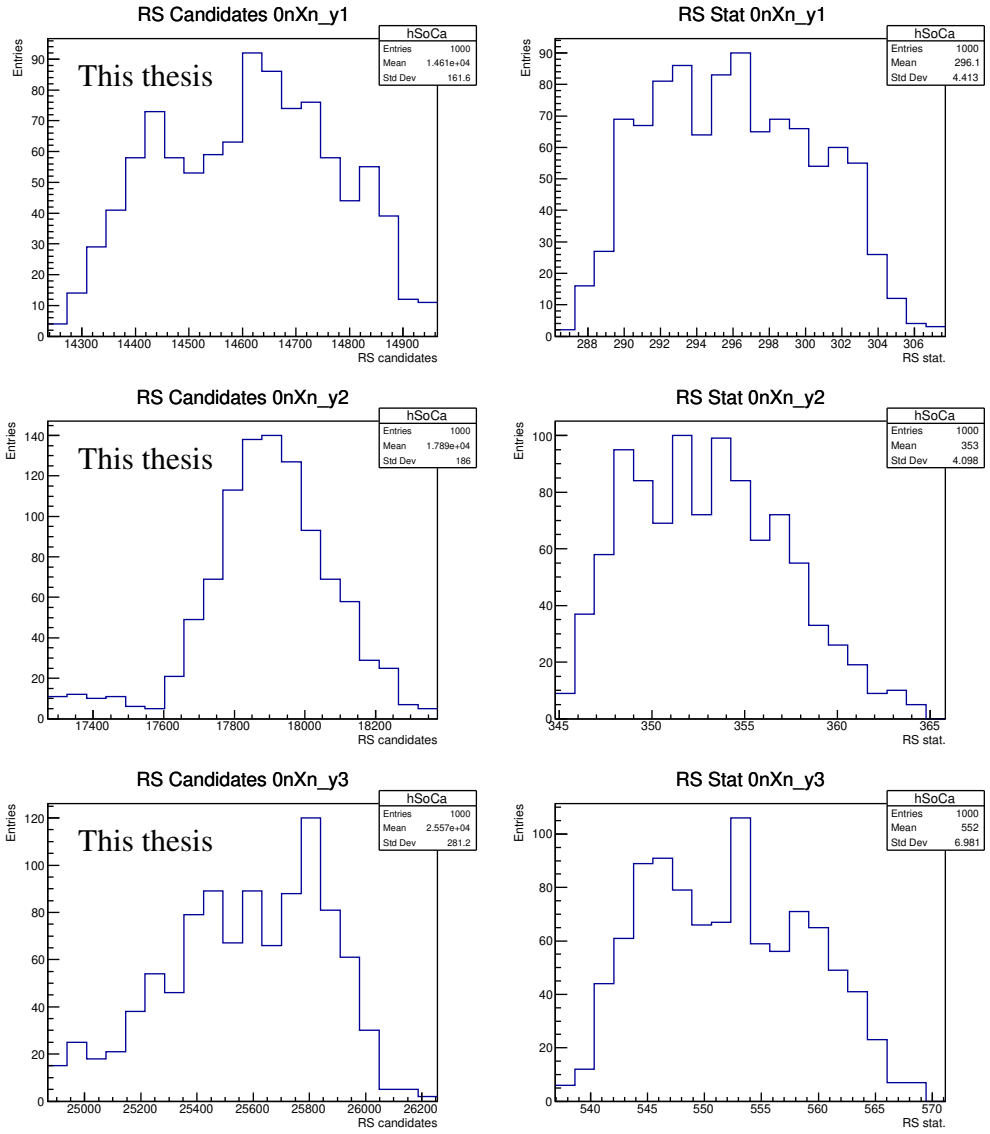

Fig. B.15: Number of candidates and its statistical uncertainty of the Ross-Stodolsky in three rapidity bins and 0nXn sample.

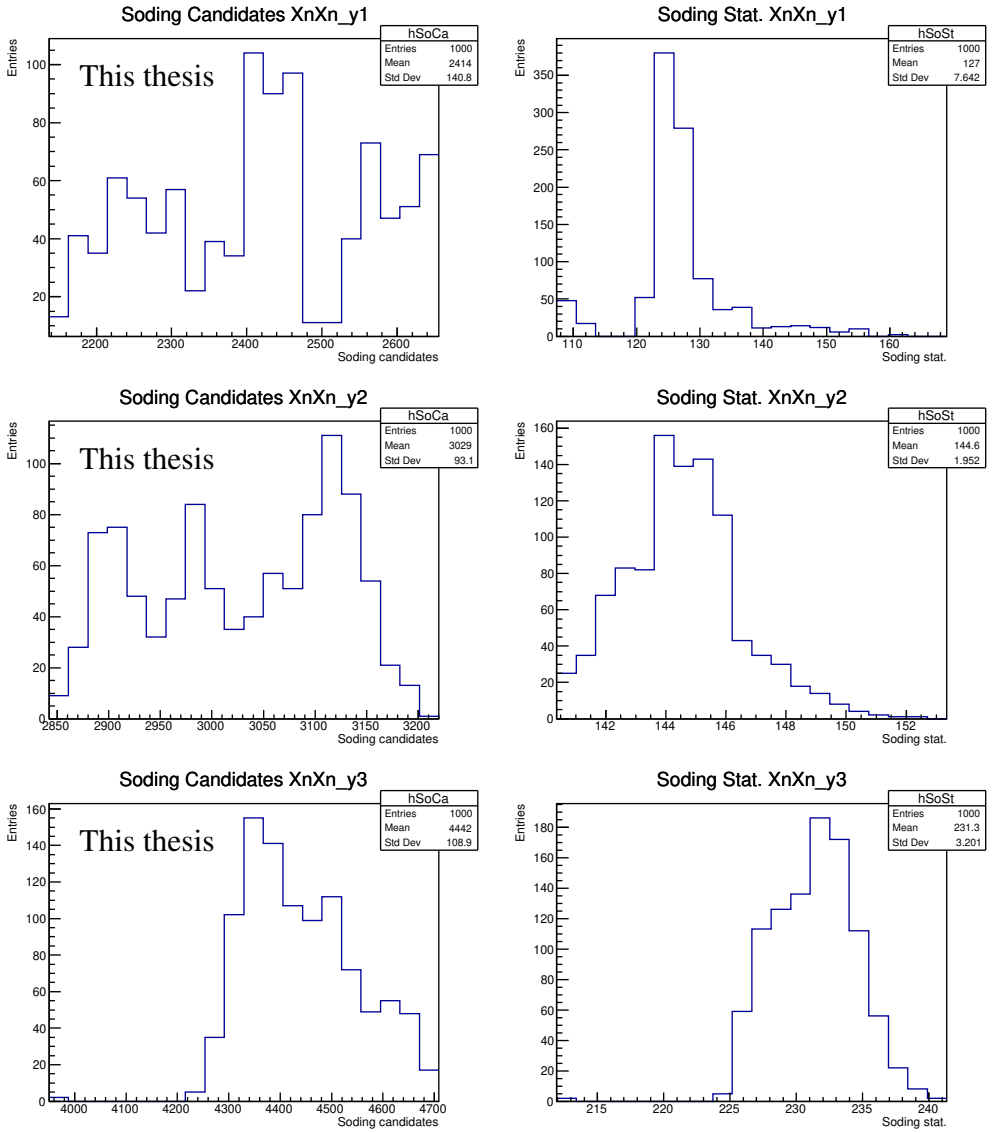

Fig. B.16: Number of candidates and its statistical uncertainty of the Söding in three rapidity bins and XnXn sample.

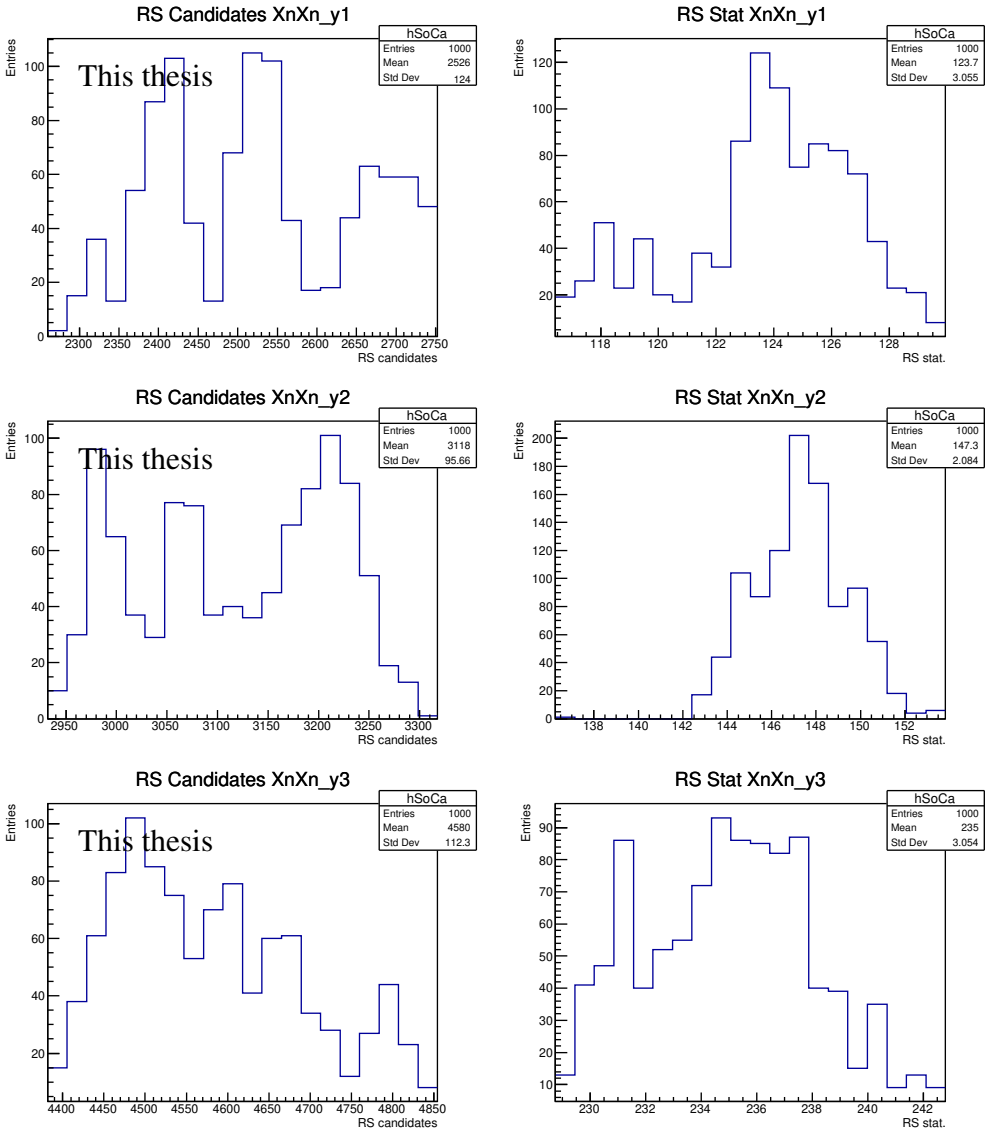

Fig. B.17: Number of candidates and its statistical uncertainty of the Ross-Stodolsky in three rapidity bins and XnXn sample.

B.6 Quark Matter 2017 poster

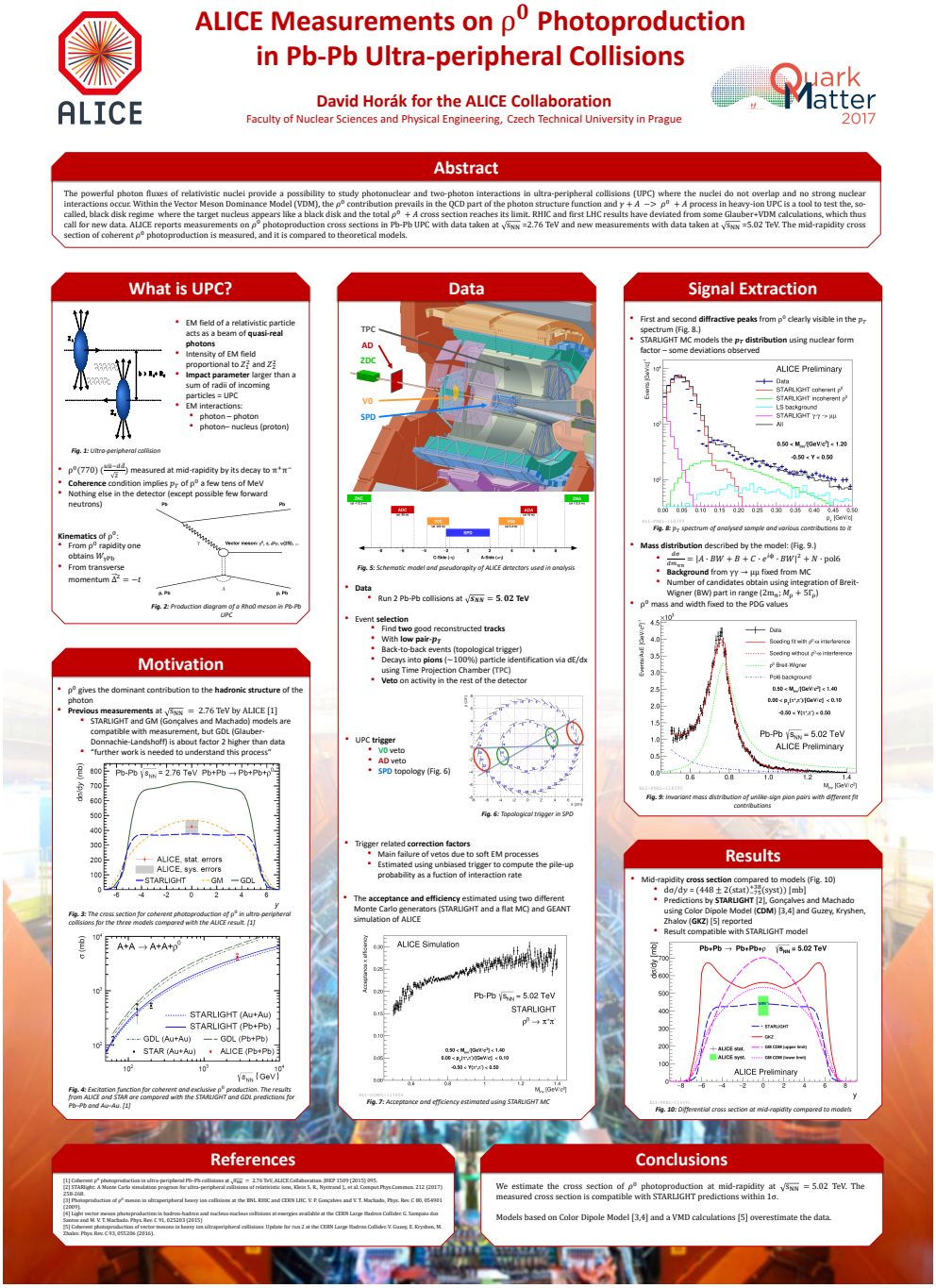

Fig. B.18: Poster of preliminary results presented at Quark Matter 2017.

B.7 LHCP 2020 poster

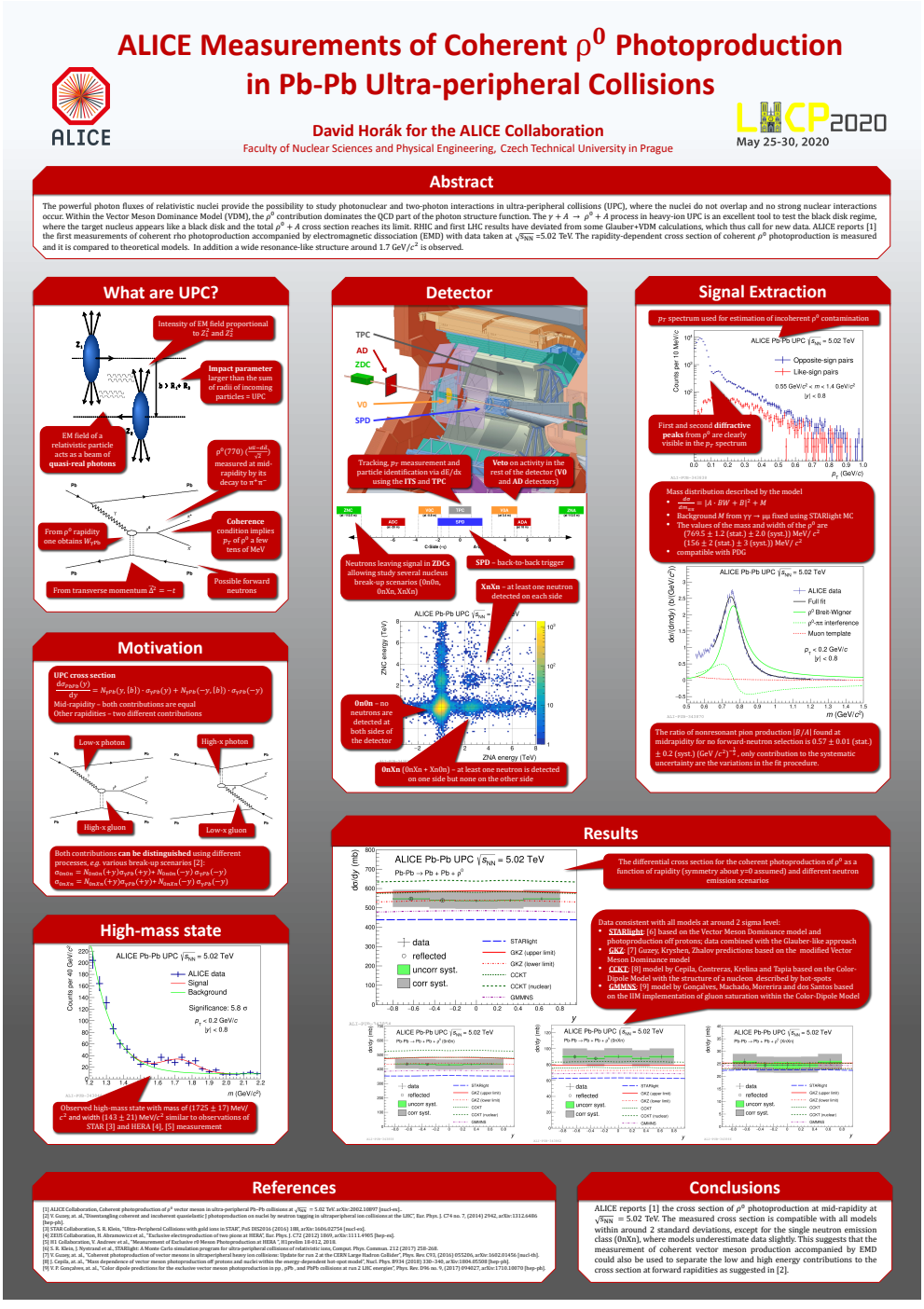

Fig. B.19: Poster of final results presented at LHCP 2020.

Appendix C

Xe–Xe

C.1 Selection criteria

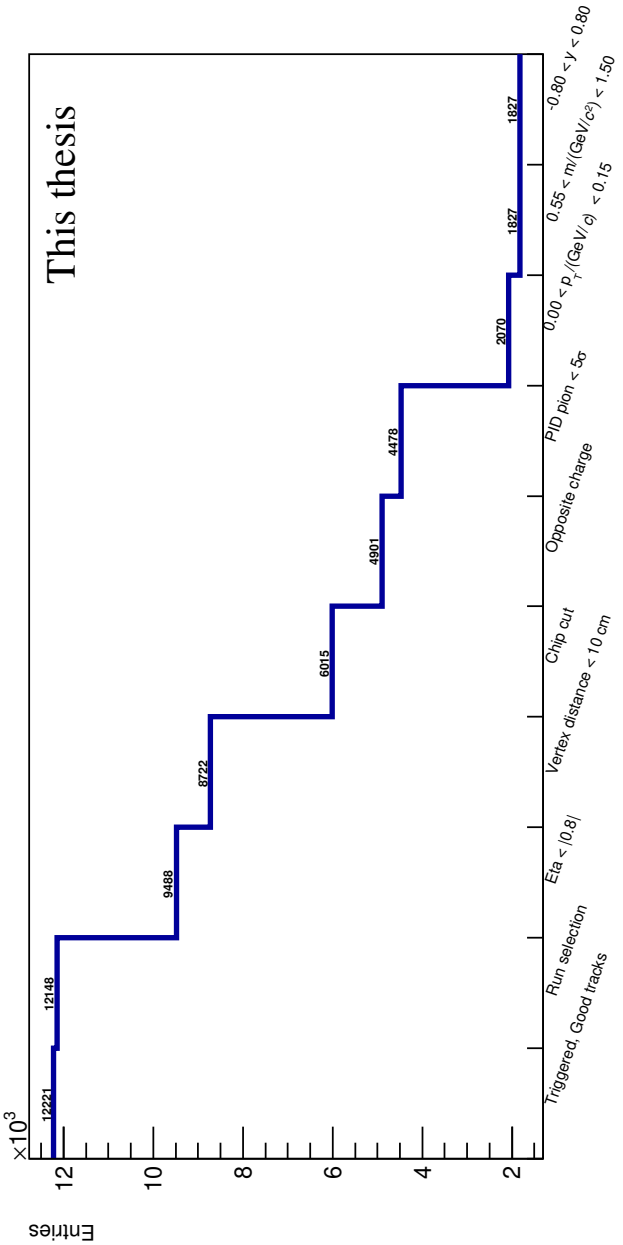

Fig. C.1: Number of events that passed through the selection criteria.

C.2 Results

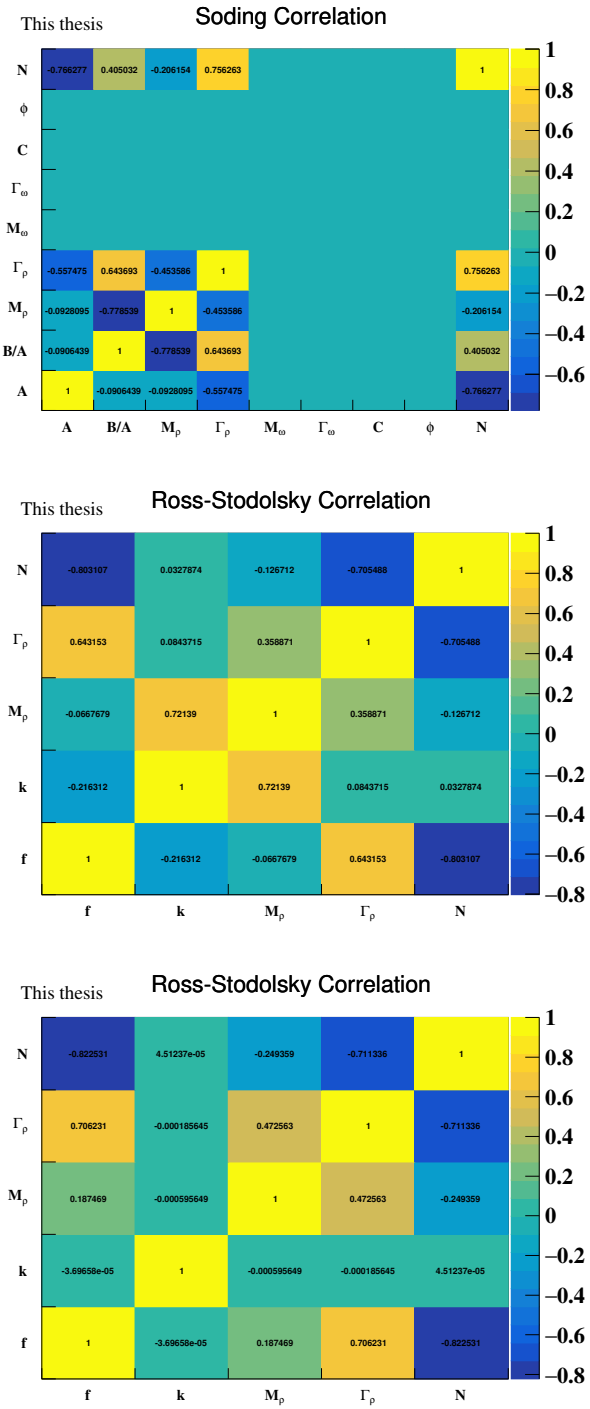

Fig. C.2: Up: Correlation matrix of the Söding fit. Middle: Ross-Stodolsky correlation matrix. Bottom: Ross-Stodolsky 2 definition.

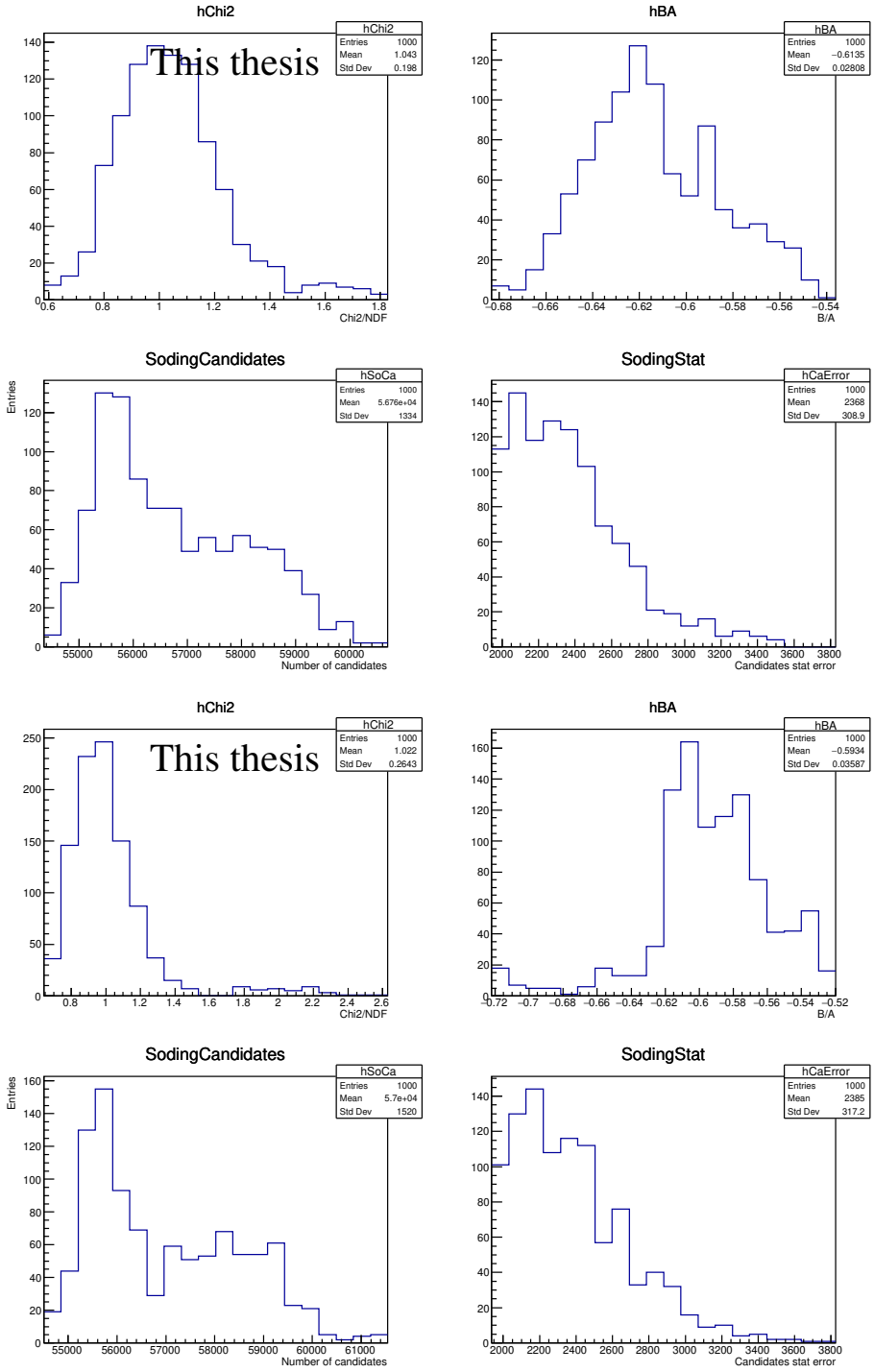

Fig. C.3: Distribution of results for performed fit on the full sample. Mean was used as a measured value and Std Dev as a systematic error. Upper: B-W with continuum, Middle: Pure B-W.

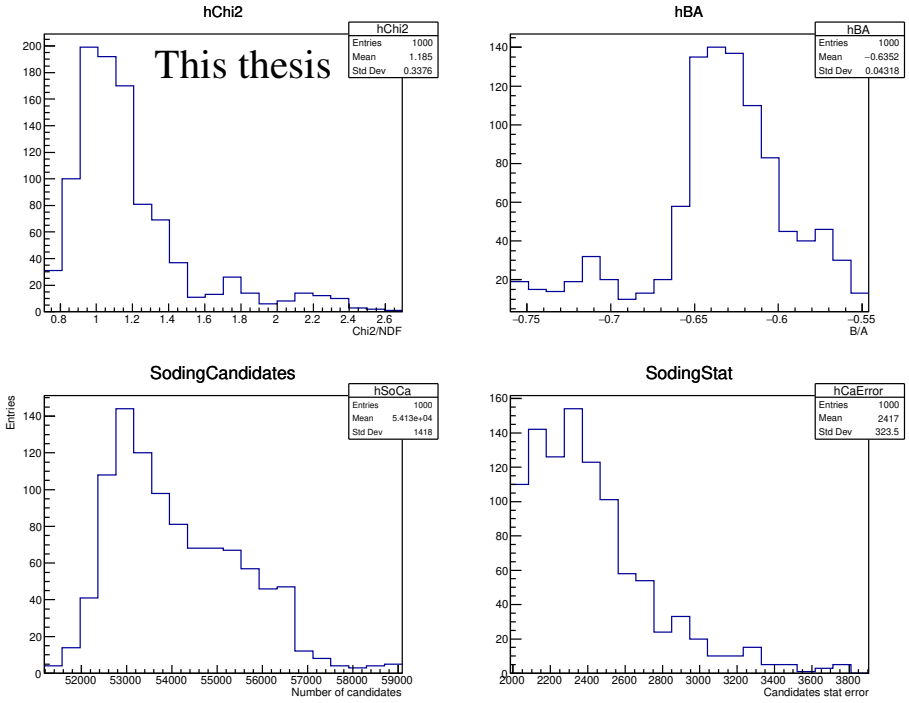

Fig. C.4: Distribution of results for performed fit on the full sample. Mean was used as a measured value and Std Dev as a systematic error. Results use the flat-mass acceptance.